PAULO ROBERTO CORREA DE ALMEIDA JUNIOR

EXPERIMENTAL AERODYNAMICS OF A WING MODEL WITH DISTRIBUTED PROPULSION IN PUSHER CONFIGURATION

UNIVERSIDADE FEDERAL DE UBERLÂNDIA

FACULDADE DE ENGENHARIA MECÂNICA

2023

PAULO ROBERTO CORREA DE ALMEIDA JUNIOR

Orientador

Prof. Dr. Odenir de Almeida

EXPERIMENTAL AERODYNAMICS OF A WING MODEL WITH DISTRIBUTED PROPULSION IN PUSHER CONFIGURATION

Projeto de Conclusão de Curso apresentado ao Curso de Graduação em Engenharia Aeronáutica da Universidade Federal de Uberlândia, como parte dos requisitos para a obtenção do título de **BACHAREL em ENGENHARIA AERONÁUTICA.**

UBERLÂNDIA - MG

2023

EXPERIMENTAL AERODYNAMICS OF A WING MODEL WITH DISTRIBUTED PROPULSION IN PUSHER CONFIGURATION

Projeto de conclusão de curso **APROVADO** pelo Colegiado do Curso de Graduação em Engenharia Aeronáutica da Faculdade de Engenharia Mecânica da Universidade Federal de Uberlândia.

BANCA EXAMINADORA

_____

Prof. Dr. Odenir de Almeida
Universidade Federal de Uberlândia

_____

Prof. Dr. João Rodrigo Andrade
Universidade Federal de Uberlândia

_____

Prof. Dr. Tobias Souza Morais
Universidade Federal de Uberlândia

UBERLÂNDIA - MG

2023

To everyone who believed in me.

ACKNOWLEDGEMENTS

I would like to thank a few of my colleagues for their instrumental help in some of the technical details of this work: Vítor Campos, for sharing his knowledge about aircraft performance and Gabriel Henrique, for teaching me so much regarding coding and instrumentation. Additionally, I want to express my gratitude to Leonardo Junqueira, for reviewing this entire work, and I cannot thank Alexandra Elbakyan enough, for contributing so much with sharing knowledge.

Finally, I would like to thank my professor Odenir de Almeida for his guidance and expertise. The absence of either would render this thesis unfeasible.

"My kind transcends your very understanding. We are each a nation. Independent, free of all weakness. You cannot even grasp the nature of our existence."

Sovereign

Almeida, P. R. C. Jr. **Experimental aerodynamics of a wing model with distributed propulsion in pusher configuration.** 2023. 106p. Graduation Project, Federal University of Uberlândia, Uberlândia, Brazil.

ABSTRACT

The goal of this project is to analyze the flow around a wing with distributed propulsion in pusher configuration in various positions, so that to find the aerodynamically-optimal configuration by assessing the pressure, C_P, lift, C_L, and drag, C_D, coefficients. The model was designed in SolidWorks software, manufactured using a 3D printer and tested in an open section subsonic wind tunnel from the External Aerodynamic Research Center (CPAERO) located in the Federal University of Uberlandia (UFU). Three main model configurations were tested: with one, two as well as no propeller, in order to assess the effect of attaching a second propeller on the aerodynamic coefficients of the wing. For this matter, the second propeller was affixed onto two different spanwise locations so that its optimal position could be assessed, while the first propeller was kept near the wing root. Additional tests using only a rake probe were made in order to get the velocity profile of the undisturbed flow. For this project, a half wing model, two propellers and two drone engines were used. The experiments suggest that the lift is increased when two propellers are affixed to the wing; this gain is strongest when the second propeller is placed closest to the wing tip, ameliorating the wing tip vortices. The effects of the propeller in the pusher configuration also include the delay in flow separation on the section near the propeller – which could be noticed during some of the experiments by an increase (in module) in the distribution values of the pressure coefficient towards the trailing edge of the wing. Finally, the drag coefficient of the wing seems to be reduced by the influence of the propellers, which is expected due to the decrease in the induced drag as well as the delay in the flow separation.

KEYWORDS: *distributed propulsion, clean wing, wind tunnel, rake probe, aerodynamic coefficients, pusher configuration.*

Almeida, P. R. C. Jr. **Experimental aerodynamics of a wing with distributed propulsion in pusher configuration.** 2023. 106p. Graduation Project, Federal University of Uberlândia, Uberlândia, Brazil.

RESUMO

O objetivo deste projeto é analisar o escoamento ao redor de uma asa com propulsão distribuída na configuração *pusher* em múltiplas posições, de forma a encontrar a configuração aerodinamicamente otimizada, através da aferição dos coeficientes de pressão, C_P, sustentação, C_L, e de arrasto, C_D. O modelo foi desenvolvido no software SolidWorks, manufaturado utilizando uma impressora 3D e testado em um túnel de vento subsônico de seção aberta do Centro de Pesquisa Aerodinâmica (CPAERO) na Universidade Federal de Uberlândia (UFU). Três principais configurações foram testadas: com uma, duas e nenhuma hélice, permitindo analisar a influência de uma segunda hélice nos coeficientes aerodinâmicos da asa. Para fazer essa avaliação, a segunda hélice foi alocada em duas posições diferentes ao longo da envergadura da asa para se encontrar a posição cujos coeficientes aerodinâmicos fossem otimizados ao máximo, enquanto que a primeira hélice foi fixada próximo da raiz da asa. Testes adicionais utilizando apenas o sensor rake foram realizados para traçar o perfil de velocidades do escoamento não perturbado. Para este projeto, foi utilizado um modelo de semi-asa, duas hélices e dois motores de drone. Os resultados experimentais apontam que a força de sustentação é aumentada ao se acrescentar duas hélices; esse ganho é máximo quando a segunda hélice é afixada o mais próximo possível da ponta da asa, combatendo os vórtices de ponta de asa. Os efeitos de uma hélice pusher também incluem um adiamento no descolamento do fluido – o que pode ser notado durante alguns dos experimentos na forma de um aumento (em módulo) nos valores da distribuição do coeficiente de pressão em direção ao bordo de fuga da asa. Finalmente, o coeficiente de arrasto da asa parece ter sido reduzido devido à influência das hélices, o que era esperado devido à redução no arrasto induzido bem como pelo adiamento no descolamento do fluido.

PALAVRAS CHAVE: *propulsão distribuída, asa limpa, túnel de vento, sensor rake, coeficientes aerodinâmicos, configuração pusher.*

List of Figures

Figure 1.1 - Aviation CO_2 emission prediction for the next decades. (Available in: <https://www.icao.int/NACC/Documents/Meetings/2014/ENVSEMINAR/8.2.IATA%20MBM.pdf >. Access in November 13th, 2022) ..... …..16
Figure 1.2 - Manzel's aircraft. (Available in: <https://patents.google.com/patent/US1487872A/en>. Access in January 10th, 2022)..... 18
Figure 1.3 - Griffith's aircraft. (Available in: <https://patents.google.com/patent/US2982495A/en>. Access in January 10th, 2022)..... 19
Figure 2.1 - NASA's e-ATLIT aircraft (Moore et al., 2013)..... 20
Figure 2.2 - NASA's LEAPTech aircraft (Borer et al., 2014)..... 21
Figure 2.3 - NASA's SCEPTOR aircraft. (Available in: <https://ntrs.nasa.gov/api/citations/20160007822/downloads/20160007822.pdf>. Access in January 10, 2020)..... 22
Figure 2.4 - Conventional (left) and modified (right) turboprop aircraft (Modified from source: de Vries et al., 2019)..... 23
Figure 2.5 - ONERA's DRAGON aircraft (Schmollgruber et al., 2019) 24
Figure 2.6 - DEPWIM wing (Modified from source: Silva Filho, 2020)..... 25
Figure 2.7 - Over-the-Wing model with pressure taps, with dimensions in millimeters (Marcus et al., 2018) 26
Figure 2.8 - Over-the-Wing model with secondary wing (Khajehzadeh, 2018) 26
Figure 2.9 - Total drag coefficient as a function of the propeller´s location (a) and total lift coefficient as a function of the propeller location (b) (Modified from source: Khajehzadeh, 2018) 27
Figure 2.10 - Aerodynamic forces breakdown on a generic section of a propeller (Anderson, 2016) 29
Figure 2.11 - Aerodynamic forces breakdown on a generic section of a propeller (Anderson, 2016) 30
Figure 2.12 - Propeller efficiency versus advance ratio (Anderson, 2016) 30

Figure 2.13 - (a) High and (b) low V_∞ effect on the angle of attack of a given blade section (Anderson, 2016) 31
Figure 2.14 - Streamwise behavior of the axial velocity and (Veldhuis, 2005, as cited in Silveira Filho, 2020) 32
Figure 3.1 – Wing model placement 33
Figure 3.2 - Wind tunnel TV-60-Zephyr 34
Figure 3.3 - Wind tunnel test section with rake probe 35
Figure 3.4 - Six-component external wind tunnel balance 36
Figure 3.5 - Minipa MT-455A digital thermometer 37
Figure 3.6 - Rake probe with pressure taps 38
Figure 3.7 - AA-TVCR2 Pressure tap reader 39
Figure 3.8 - Model dimensions (in millimeters) 40
Figure 3.9 - Manufactured model 41
Figure 3.10 - Exploded view of the entire model 42
Figure 3.11 - Airfoil s8036 42
Figure 3.12 - Wing without enclosures 44
Figure 3.13 - Upper surface enclosure with holes (top) and corresponding wing opening (bottom) 45
Figure 3.14 - Main wing longeron 46
Figure 3.15 - Example of wing stringer 46
Figure 3.16 - Segments of a secondary wing longeron 47
Figure 3.17 - Wing fairing 48
Figure 3.18 - Nacelle 49
Figure 3.19 - Motor retainer 49
Figure 3.20 - 8x4 Propeller 50
Figure 3.21 - Drone motor Emax XA2212/980 KV 51
Figure 3.22 - Power supply unit BLU500R-BCASE 51
Figure 3.23 - Microcontroller board Arduino UNO 52
Figure 3.24 - MakerBot Replicator Z18 3D printer 53
Figure 3.25 - Locations for placement of nacelle + propeller on the wing, with pressure taps in location U1 as an example 55

Figure 3.26 - Wing configurations analyzed in the wind tunnel..... 59
Figure 3.27 - Panel distribution of the wing (top) and streamlines around the wing (bottom) 60
Figure 4.1 - Velocity profile of the flow in the test section..... 63
Figure 4.2 - Pressure distribution on the clean wing (AoA = 2°) 64
Figure 4.3 - Pressure distribution on the clean wing (AoA = 4°) 66
Figure 4.4 - Lift polar comparison for the clean wing..... 67
Figure 4.5 - Drag polar comparison for the clean wing..... 68
Figure 4.6 - Pressure distribution for wing + one propeller on location 1 and pressure differential measurements on location U1..... 70
Figure 4.7 - Pressure distribution for wing + two propellers on location 1 + 3 and pressure differential measurements on location U1 + U3 (AoA = 4°)..... 72
Figure 4.8 - Pressure distribution for wing + two propellers on location 1 + 4 and pressure differential measurements on location U1 + U4 (AoA = 4°)..... 74
Figure 4.9 - Lift polars for wing + two propellers on locations 1 + 3 and 1 + 4 76
Figure 4.10 - Drag polars for wing + two propellers on locations 1 + 3 and 1 + 4 78

List of Tables

Table 3.1 - Precision parameters of the six-component external wind tunnel balance..... 36
Table 3.2 - Airfoil coordinates (s8036). (Available in: < http://airfoiltools.com/airfoil/details?airfoil=s8036-il >. Access in January 12 th, 2020)..... 43

Contents

1 Introduction 15

2 Bibliographic review and physical aspects 20

2.1 Propeller aerodynamics 28

3 Methodology 33

3.1 Experiment setup 33

3.1.1 Wind tunnel 34

3.1.2 Wind tunnel balance 35

3.1.3 Digital thermometer 37

3.1.4 Rake probe 37

3.1.5 Pressure tap reader 38

3.2 The model 39

3.2.1 Model design 39

3.2.1.1 Wing 42

3.2.1.2 Nacelle 48

3.2.1.3 Propeller 50

3.2.1.4 Drone motor 50

3.2.1.5 Power Supply Unit 51

3.2.1.6 Arduino UNO 52

3.2.2 Model manufacture 52

3.3 Locations of measurement 53

3.3.1 Rake probe 54

3.3.2 Wing 54

3.4 Test conditions 55

3.4.1 Boundary layer thickness 56
3.4.2 Wind tunnel readings setup 56
3.4.3 Pressure tap reader readings setup 57
3.5 Experimental procedure 57
3.6 Numerical procedure 59
4 Results 62
4.1 Rake probe 62
4.2 Clean wing 63
4.3 Wing and one propeller 69
4.4 Wing and two propellers 71
5 Conclusions 80
References 82
Appendix 85
Appendix A – C_P Distribution code 86
Appendix B – C_L Polar code 92
Appendix C – C_D Polar code 96
Appendix D – Control of the drone motors 100

1 Introduction

OBS.: This project was executed mostly during the end of 2021, amid the peak of the COVID-19 pandemic in Brazil. As a consequence, multiple restrictions arose: social distancing as well as limited opening hours within the university campus, which impaired access to both required laboratory equipment and relevant personnel; limited means of commuting to and from the university campus; impossibility of redoing experiments in the laboratory, so as to minimize the exposure risk to the pathogen as much as possible to all people involved.

For some time, environmental awareness has been growing and becoming a consensus among humans, to such a degree that reducing toxic emissions and general harm to nature are goals almost as important as financial gain. If no action is taken, the environmental footprint of the aviation industry is expected to soar, since the number of flights worldwide keeps rising, as depicted by Figure 1.1. Even though the aviation market is currently only responsible for around 2% of global man-made CO_2 emissions, it is imperative that this tendency be ameliorated, possibly by multiple actions, such as technology breakthroughs, biofuels and operations measures (International Civil Aviation Organization, 2014).

Figure 1.1- Aviation CO2 emission prediction for the next decades

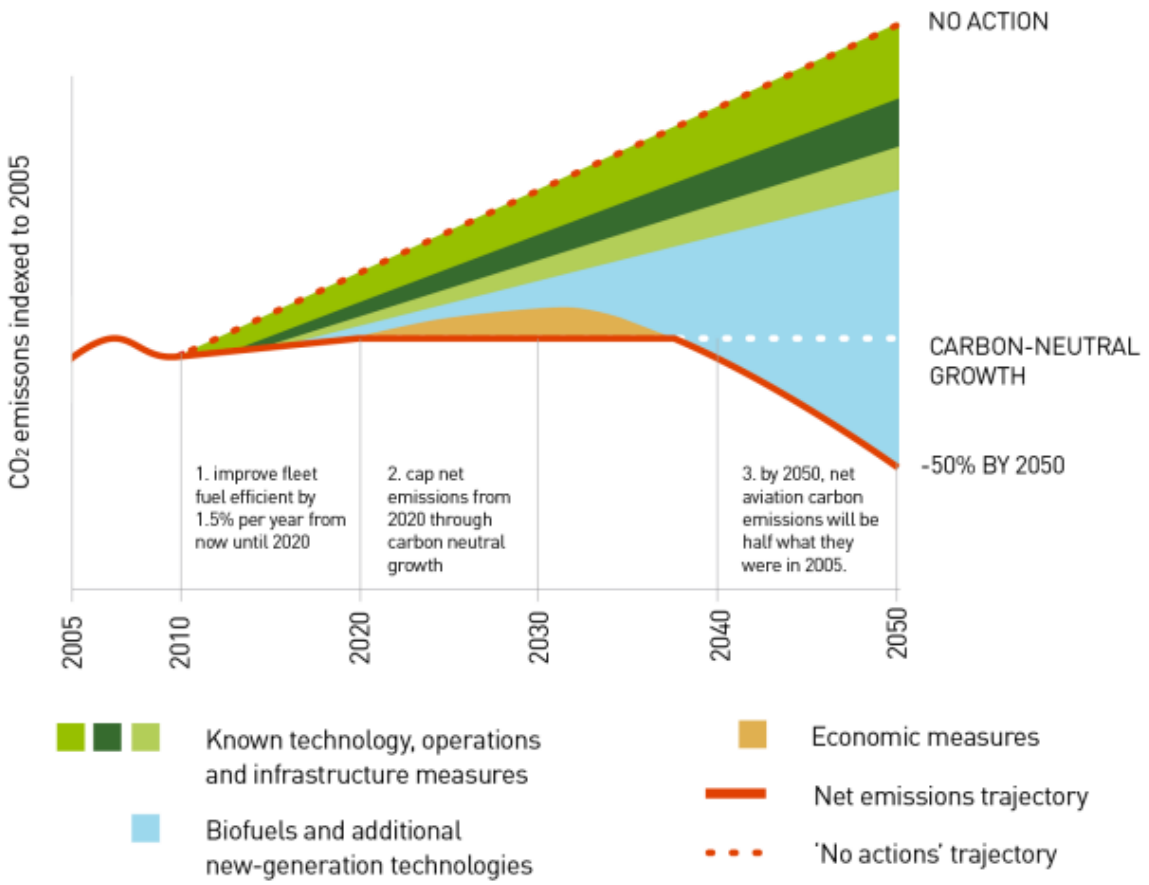

Note. Retrieved from <https://www.icao.int/NACC/Documents/Meetings/2014/ENVSEMINAR/8.2.IATA%20MBM.pdf >. Access in November 13th, 2022.

Considering this context, distributed propulsion represents a technological advancement that could potentially reduce the negative impact – and cost – of operating an aircraft by reducing the aircraft's weight and drag coefficient for the cruise phase of flight (Stoll, 2015), while increasing the lift coefficient for the same flight phase (Silva Filho, 2020). Other benefits include fuel burn reduction (Khajehzadeh, 2018; Pan, 2020) and noise reduction (Marcus et al., 2018; Pan, 2020). This configuration also allows for a reduction in the required span and weight of the wing, since the required propulsive power is lessened and the takeoff and landing speeds are increased (Keller, 2021). Furthermore, the distributed electric propulsion (DEP), would technically allow for a flight without the use of fossil fuels whatsoever, representing a major advantage of this configuration.

Conceptually, the distributed propulsion is the use of multiple thrust-generating devices (which usually employ propellers) placed along the wingspan, often amounting to a significantly bigger number of devices than the one when the conventional system is adopted. As each device in this model has smaller dimensions than in the conventional system, the aircraft wetted area is reduced, lowering the aircraft drag (Sgueglia, 2019). Various other parameters are involved in each specific configuration of distributed propulsion, such as the chordwise location, the size, rotation speed and direction of each one of the propellers (in the cases in which propellers are adopted), the type of motor as well as the vertical distance of said propellers to the wing. This expansive array of possibilities resulted in many concepts regarding this propulsion system, each with its own set of advantages and disadvantages.

Some of the current limitations of the DEP concept are the heavy weight of the required battery system, the low energy density of said batteries (Wh/kg) as well as the challenges in recycling them. Considering the distributed propulsion concept as a whole, another obstacle is the reduction in the stall angle, α_{stall} (Silva Filho, 2020).

Furthermore, two main distributed propulsion configurations were considered: tractor and pusher. Even though the former has a superior aerodynamic performance in most cases – considering that its slope of the $C_L \times \alpha$ curve, C_{L_α}, aerodynamic efficiency, $^{C_L}/_{C_D}$, and maximum lift coefficient, C_{Lmax}, are all higher than those of the pusher configurations (Chinwicharnam & Thipyopas, 2016), it was decided that this work would only test the pusher configuration, due to time and financial constraints and especially by the scarcity of works about this configuration. All other conceptual designs, for instance the disk-wing, under-wing nacelle (UWN) and over-the-wing (OTW) were discarded as well.

Historically, distributed propulsion has been conjectured for a long time, with relevant designs dating as far back as the second decade of the 20th century, with Manzel's aircraft (Manzel, 1924), shown in Figure 1.2. He conducted experimental studies which proved that this system could further energize the flow around the wing, and he had an inkling that this system could allow for a laminar flow, optimizing takeoff and landing distances (Sgueglia, 2019). Years later, another quite important design aimed for shorter takeoff and landing (STOL), this time by the

implementation of thrust vectoring, which would increase the lift force generated by the aircraft (Griffith, 1954). This model is illustrated in Figure 1.3.

Figure 1.2 - Manzel's aircraft

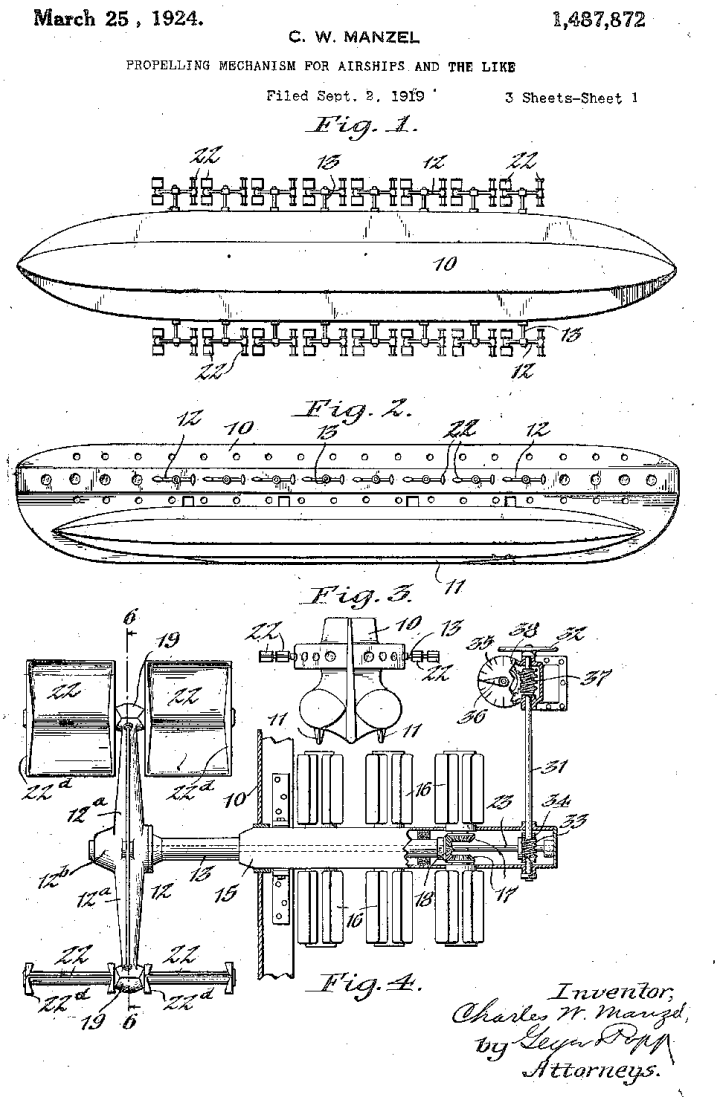

Note. Retrieved from <https://patents.google.com/patent/US1487872A/en>. Access in January 10th, 2022.

Figure 1.3 - Griffith's aircraft

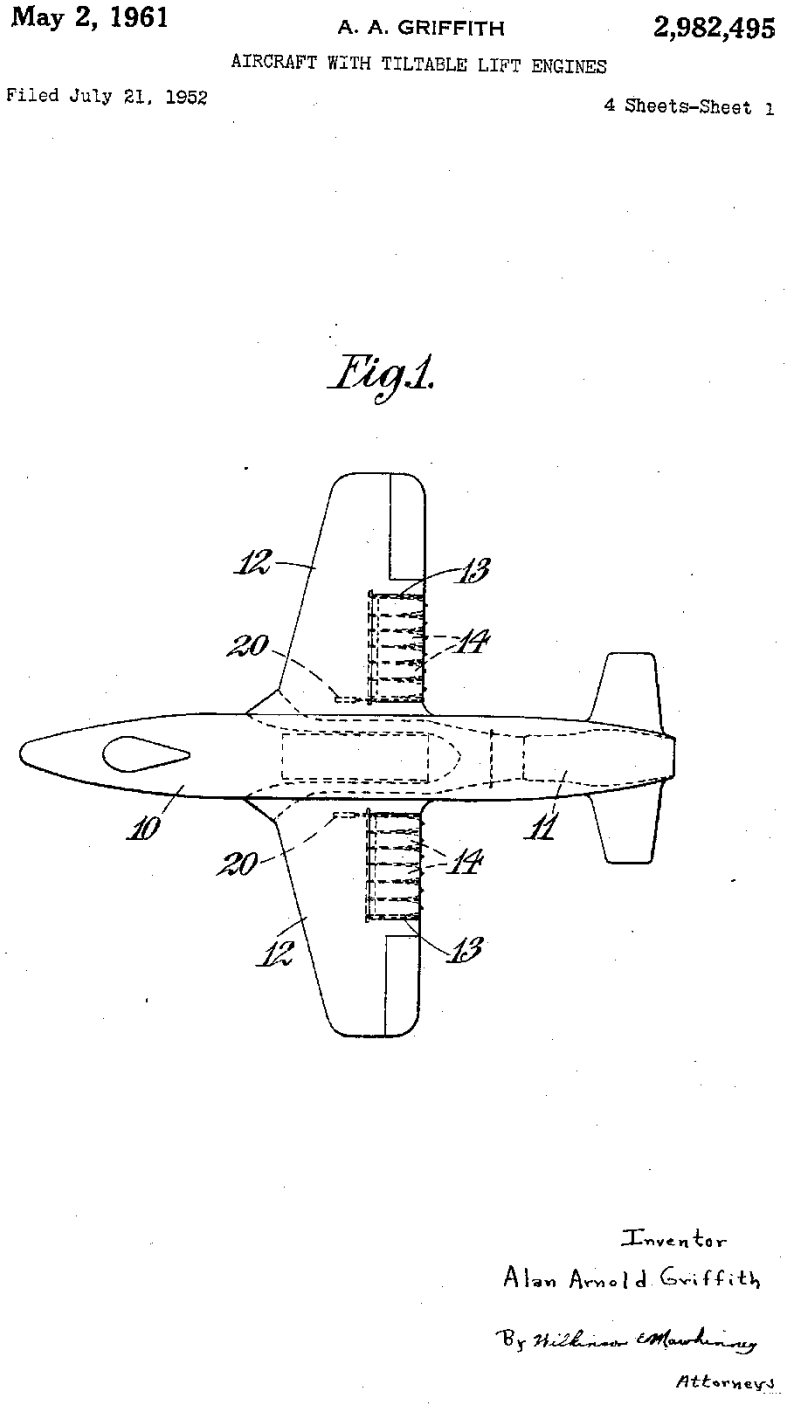

May 2, 1961 A. A. GRIFFITH 2,982,495

AIRCRAFT WITH TILTABLE LIFT ENGINES

Filed July 21, 1952 4 Sheets-Sheet 1

Fig.1.

Inventor
Alan Arnold Griffith
By Wilkinson & Mawhinney
Attorneys

Note. Retrieved from <https://patents.google.com/patent/US2982495A/en>. Access in January 10th, 2022.

2 Bibliographic review and physical aspects

On more recent years, new distributed propulsion concepts were introduced by the National Aeronautics and Space Administration (NASA), such as the Advanced Technology Light Twin aircraft (e-ATLIT) depicted in Figure 2.1, whose leading edge propellers allowed for a fowler flap that extended through the whole wingspan. This configuration yielded a maximum lift coefficient, C_{Lmax}, of 5.0, for low-speed flight conditions (Moore et al., 2013). Its overlapping propellers, furthermore, help maximize the slipstream effect on the surface of the wing (Silva Filho, 2020).

Figure 2.1 - NASA's e-ATLIT aircraft

Note. Moore et al., 2013.

Another concept aircraft proposed by NASA, illustrated in Figure 2.2, was the Leading Edge Asynchronous Propellers Technology aircraft (LEAPTech), which represents a revised version of the former aircraft, consisting in leading edge propellers in addition to trailing edge tail propellers. Due to its electric motors, the rpm of each propeller can be somewhat different – avoiding acoustic beating phenomena and therefore greatly reducing aircraft operation noise (Moore & Fredericks, 2014).

Figure 2.2 - NASA's LEAPTech aircraft

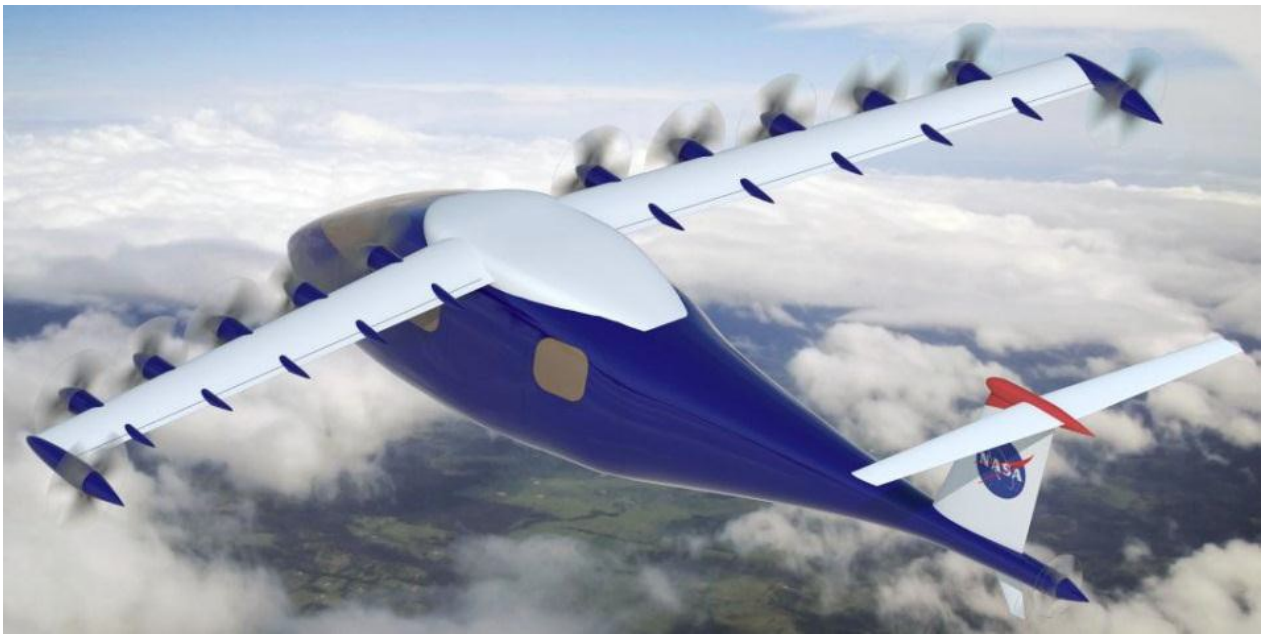

Note. Borer et al., 2014.

The third iteration of this NASA conceptual design, shown in Figure 2.3, is the Scalable Convergent Electric Propulsion Technology Operations Research aircraft (SCEPTOR), which shifted the tail propellers from the trailing edge to the leading edge, increasing the dynamic pressure over the wing for low-speed flight conditions. The sum of all the leading edge propellers allows for a smaller wingspan, since the lift force is boosted. During slow-speed flight conditions, all propellers would be employed, in order to maximize the lift force. Alternatively, for high-speed flight conditions, such as the cruise phase, only the tail propellers would be used, while the others would be stowed (Patterson et al., 2016). Finally, the tail propellers would spin in a way that would counteract the induced drag (Silva Filho, 2020).

Figure 2.3 - NASA's SCEPTOR aircraft

Note. Retrieved from <https://ntrs.nasa.gov/api/citations/20160007822/downloads/20160007822.pdf>. Access in January 10th, 2022.

A modified version of NASA's SCEPTOR aircraft (SCEPTOR Mod I) with a different number of propellers and tail propeller size was tested experimental and analytically, which corroborated that the multiple propellers increase the dynamic pressure over the wing. Furthermore, the difference between the experimental and analytical results differed by around 10%, mainly due to simplifications in the computational simulations and experimental uncertainty. Also, this configuration would allow for a C_{Lmax} of over 4.3 – representing a relevant way of reducing cruise drag (Stoll, 2015).

Another conceptual design is for a commuter aircraft with 19 passenger seats and 16 electric-powered propellers, which provide an increase in the lift coefficient due to the slipstream effect on the wing surface, optimizing the take-off and landing performance and reducing the required wing area. Additionally, it was noticed that the increase in the number of propellers – while reducing their diameters and maintaining the wingspan – results in a more pronounced blown wing effect, while the maximum theoretical propeller efficiency is decreased. In a way to further analyze this dichotomy, it was implemented a parametric study concerning the number of propellers, which concluded that a higher number of them would increase the propulsive efficiency due to a decline in fuel consumption. Finally, the addition of electric batteries in the powertrain architecture did not affect the fuel consumption significantly (Orefice et al., 2020).

A considerably bigger aircraft concept was proposed on a study in Delft University of Technology, depicted in Figure 2.4, which features a modified regional turboprop with distributed propulsion and a propulsive empennage. This analysis showed a decrease in payload-range efficiency by 2.5% when compared to a conventional aircraft – contrary to most theoretical studies currently available on distributed propulsion –, which suggests that its expected benefits may be offset by inaccuracies in the sizing process of the aircraft and in the design of the distributed propulsion system. Nonetheless, a few benefits of the distributed propulsion are indicated, such as an increase in payload-range efficiency of up to 12% at constant cruise altitude and a higher maximum effective lift during landing due to thrust vectoring (de Vries et al., 2019).

Figure 2.4 – Conventional (left) and modified (right) turboprop aircraft

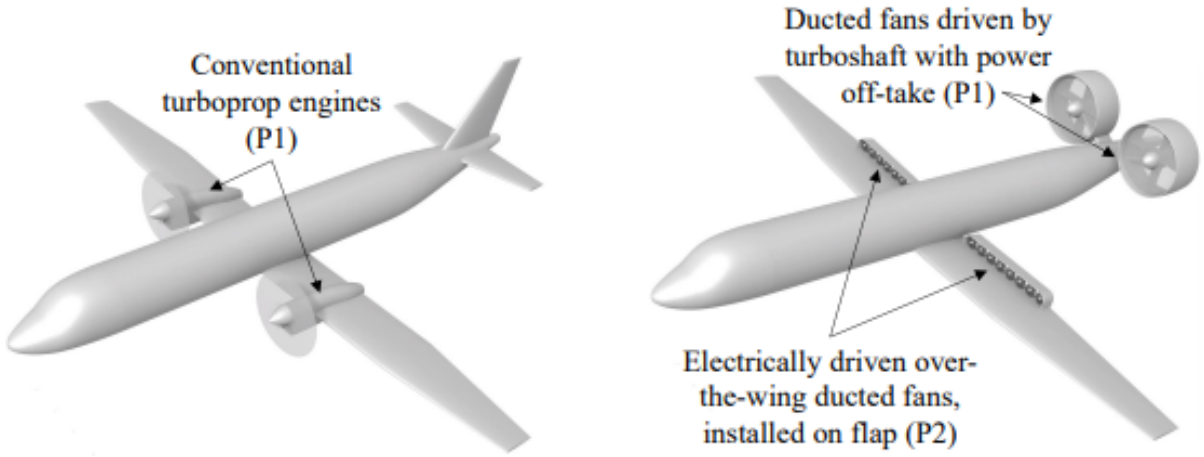

Note. Modified from source: de Vries et al., 2019.

Another concept, much bigger, was designed in the Office National d'Etudes et de Recherches Aérospatiales (ONERA), called Distributed fans Research Aircraft with electric Generators by ONERA (DRAGON). This aircraft, shown in Figure 2.5, was envisioned to carry 150 passengers and would have multiple electric-powered fans, with the basic principle of scaling down the fans in order to achieve major gains in terms of fuel consumption, which shuns the geometric drawbacks of increasing the fan size in typical configurations so that to achieve the same goal. Being mindful of the transonic regime of the aircraft, this concept placed the fans in a pusher configuration, on the lower surface of the wing, which may the delay wave drag rise on the upper surface of the wing and prevent buffet onset. Finally, provided that significant advancements on

the DEP technology are made, this aircraft is expected to require 5% less fuel (Schmollgruber et al., 2019).

Figure 2.5 – ONERA's DRAGON aircraft

Note. Schmollgruber et al., 2019.

Academic works were also analyzed, such as the Distributed Electric Propulsion Wing Interference Model (DEPWIM), shown in Figure 2.6, which consists of an untampered and untwisted semispan wing with four leading edge propellers. One difference between this model and the e-ATLIT is that the former has a gap between the radii of each propeller, so that there are regions not directly affected by the slipstream. The analytical results of the DEPWIM, when compared to the clean wing, showed that C_{Lmax} was increased, as well as the C_{L_α} (Silva Filho, 2020). Three academic works were examined, in addition to the DEPWIM model: the first one consists of an OTW propeller and a wing (untampered and untwisted) with a fowler flap in addition to pressure taps in a zigzag fashion on both the suction and pressure sides of the wing. The propeller can be attached to the flap, generating a magnitude of thrust vectoring for low-speed flight conditions. In addition, ground clearance is simplified and flyover noise is ameliorated due

to the shielding effects of the wing, when compared to the more conventional tractor configuration (Marcus et al., 2018). This model can be seen in Figure 2.7.

Figure 2.6 – DEPWIM wing

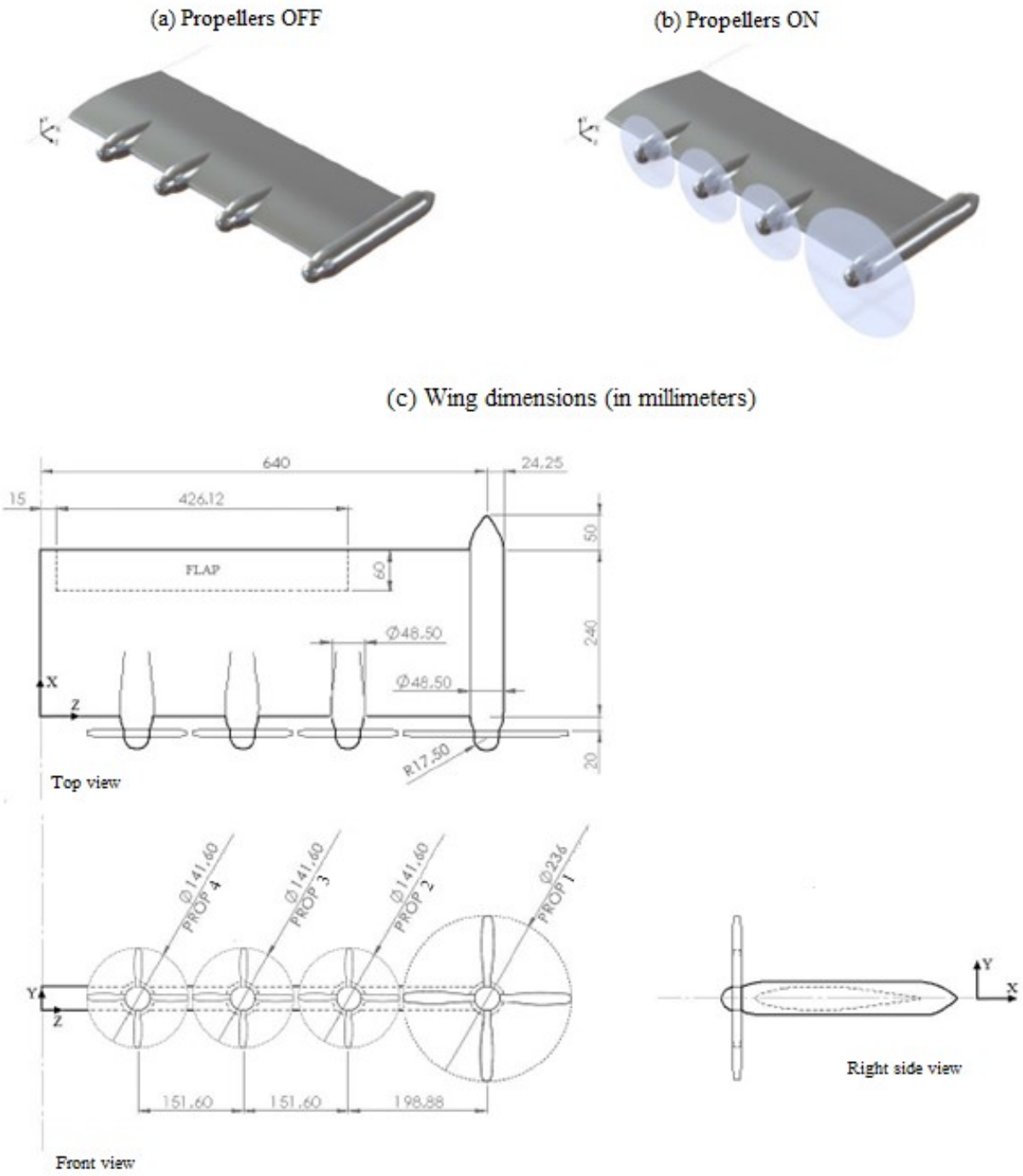

Note. Modified from source: Silva Filho, 2020.

Figure 2.7 – Over-the-Wing model with pressure taps, with dimensions in millimeters

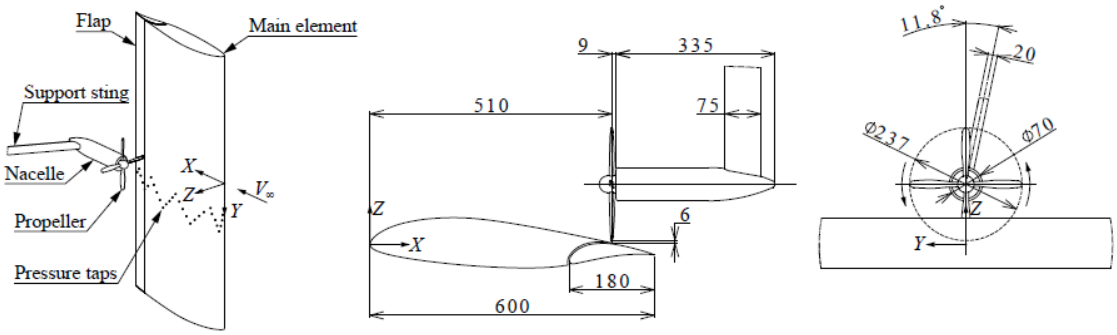

Note. Marcus et al., 2018.

The second academic work is an iteration of the last one, with the addition of a duplicate and in-scale wing, located above the propeller, as shown in Figure 2.8. It was discovered that the total drag coefficient would increase as the propeller was moved towards the trailing edge of the main wing, while this effect was significantly less pronounced for the total lift coefficient, which can be noticed in Figure 2.9. Furthermore, the secondary wing can increase the total lift coefficient by accelerating the flow over it while boosting the propeller efficiency by decelerating the flow between the wings. All these remarks contributed to the conclusion that the addition of a secondary wing to an OTW configuration could significantly enhance the aerodynamic characteristics of the system as a whole (Khajehzadeh, 2018).

Figure 2.8 – Over-the-Wing model with secondary wing

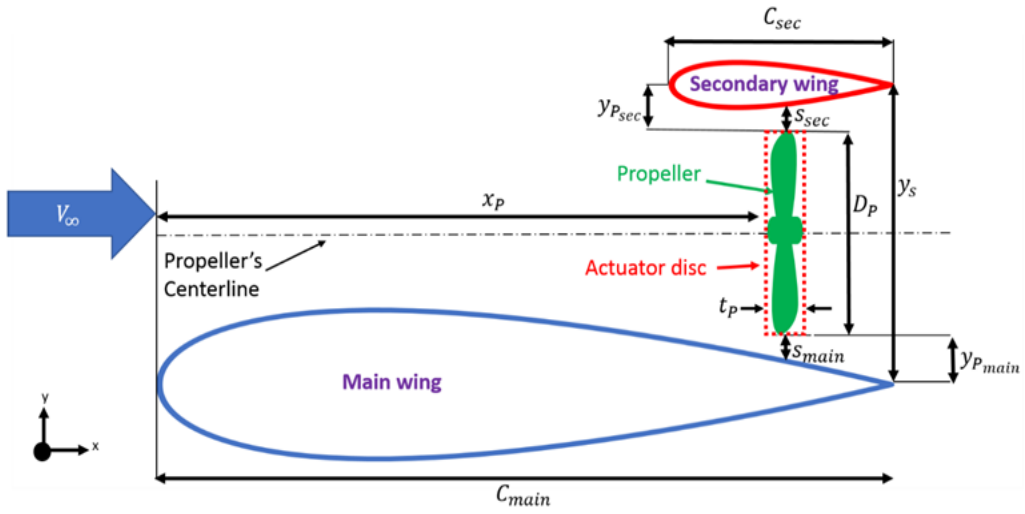

Note. Khajehzadeh, 2018.

Figure 2.9 – Total drag coefficient as a function of the propeller's location (a) and total lift coefficient as a function of the propeller location (b)

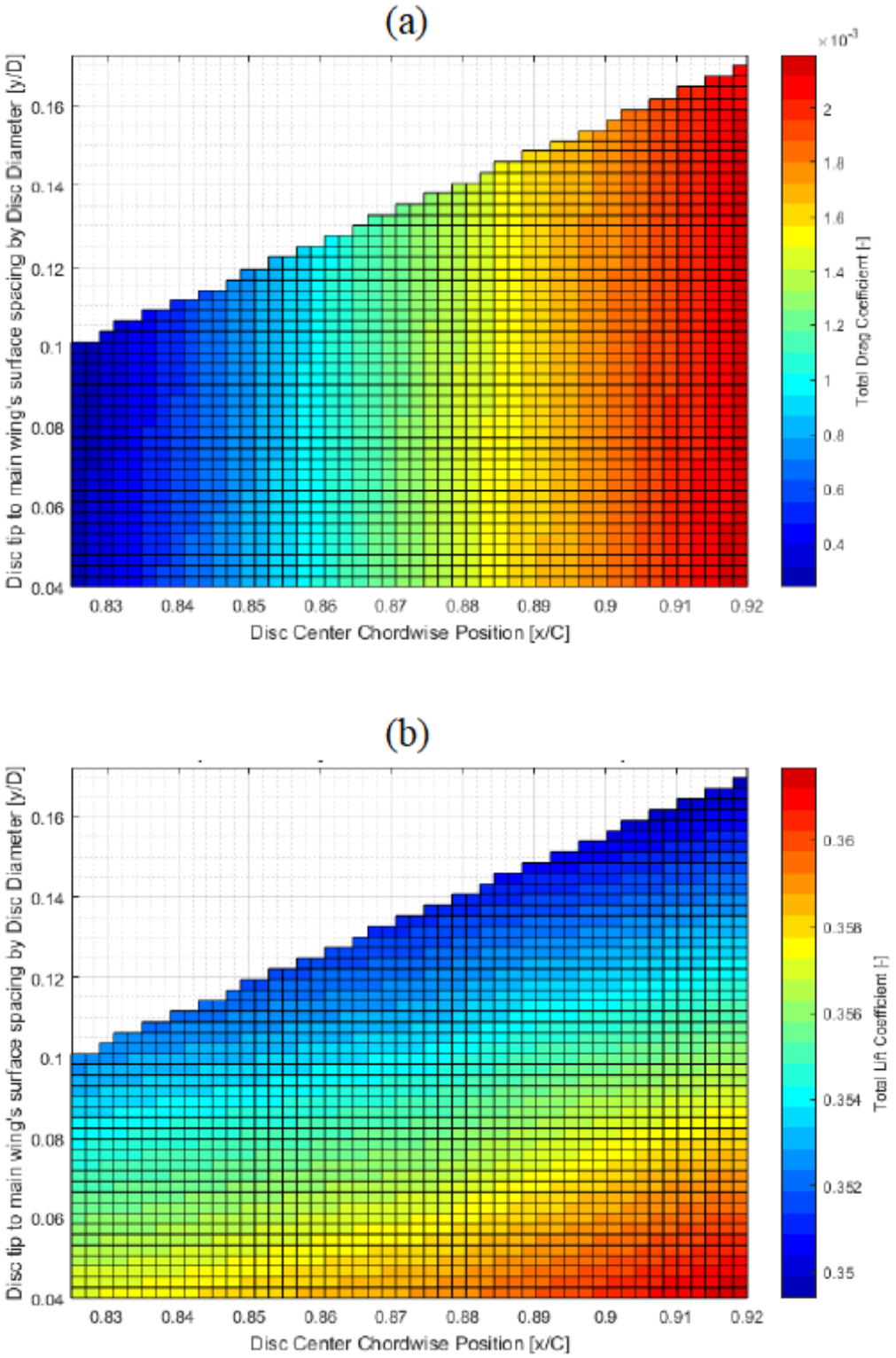

Note. Modified from source: Khajehzadeh, 2018.

The third academic work focuses on comparing OTW and UWN configurations for a distributed propulsion system. It was found that the UWN has the lowest drag coefficient while reducing the likelihood of shock wave formation, which reduces or even avoids wave drag. The OTW design is worse due to requiring a higher α in order to generate the same amount of lift as the UWN design – strengthening both suction force and shock waves on the upper surface of the wing. Finally, due to the propeller location, the upper surface flow of the UWN configuration does not decelerate as much, which leads the static pressure of the aft upper surface to not increase as much, bolstering the suction force. Therefore, the α required to generate the same lift force is reduced (Pan, 2020)

2.1 Propeller aerodynamics

This subsection presents the aerodynamic effects of a propeller on the flow, briefly explaining the relating physical phenomena. A propeller is comprised of multiple airfoil sections, each with a specific pitch angle, β, which is the angle between the airfoil chord and the rotation plane of the propeller. Due to the propeller rotation, the section speed due to the rotation of the blade (calculated by the product of the angular speed, ω, and the distance from a given section to the root, r) increases towards the tip of each blade (Anderson, 2016), and so the pitch angle must vary in order to maintain the same amount of thrust, T, generated by each section, as illustrated in Figure 2.10.

Figure 2.10 – Aerodynamic forces breakdown on a generic section of a propeller

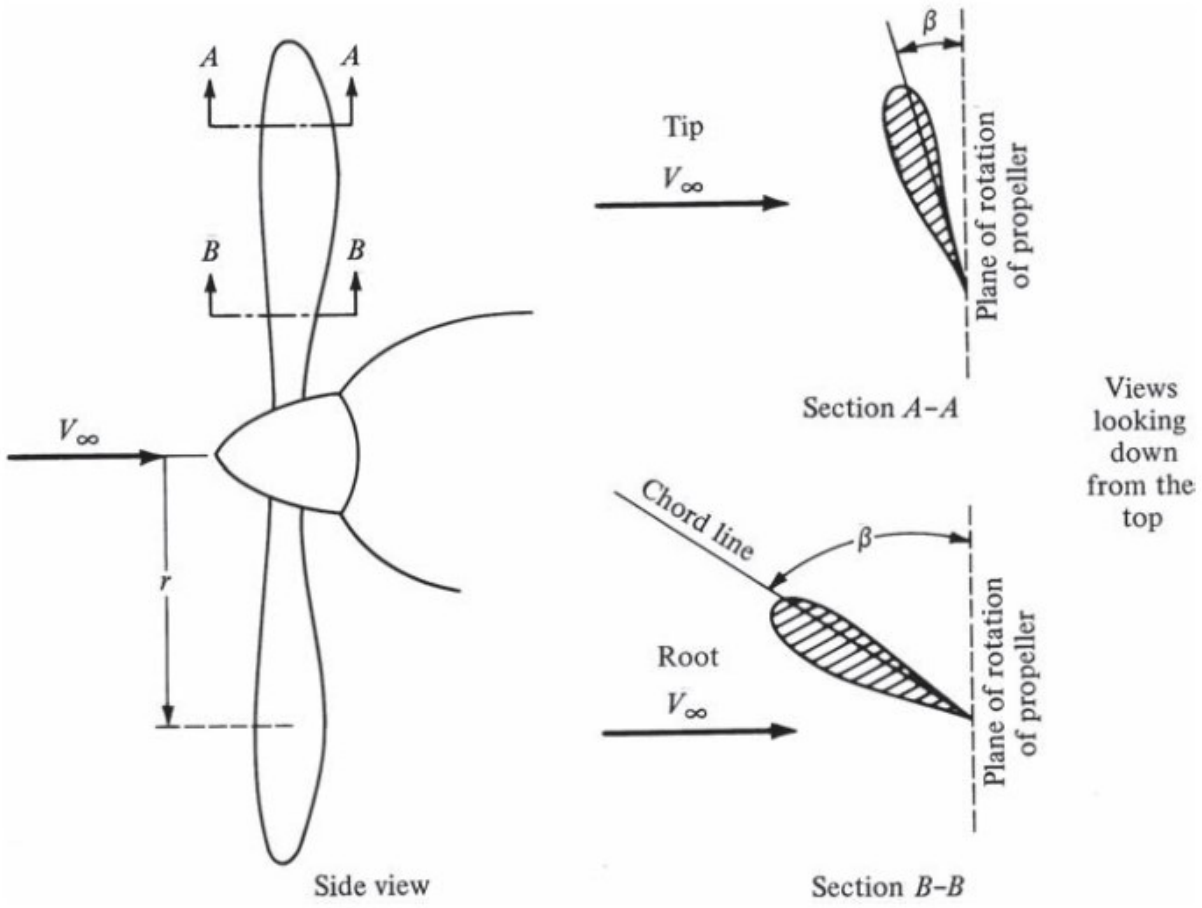

Note. Anderson, 2016.

The section thrust force can be calculated from the lift force, L, and the drag force, D, by Equation 2.1.

$$T = Lcos\phi - Dsin\phi \tag{2.1}$$

Another velocity component that affects the propeller is the one corresponding to the airplane's relative wind, V_∞, which reduces the angle of attack of each section by an ϕ angle, equivalent to $\beta - \alpha$, as shown in Figure 2.11.

Figure 2.11 – Aerodynamic forces breakdown on a generic section of a propeller

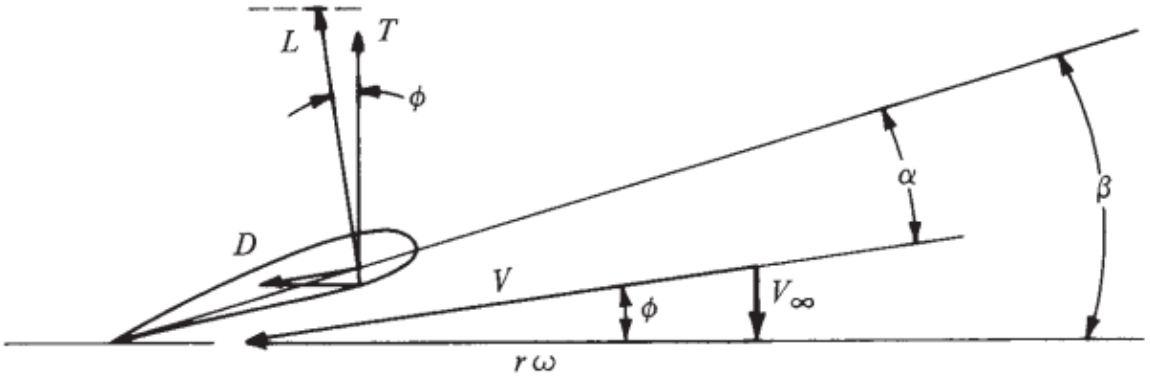

Note. Anderson, 2016.

The propeller efficiency, η, can be optimized for a given pitch angle by varying the advance ratio, J, which is defined as the relation between the freestream and the rotational velocities (Anderson 2016), as shown by Figure 2.12. This dimensionless parameter can be calculated using the rotational speed, n, and the propeller diameter, D_p, by Equation 2.2.

$$J = \frac{V_\infty}{nD_p} \tag{2.2}$$

Figure 2.12 – Propeller efficiency versus advance ratio

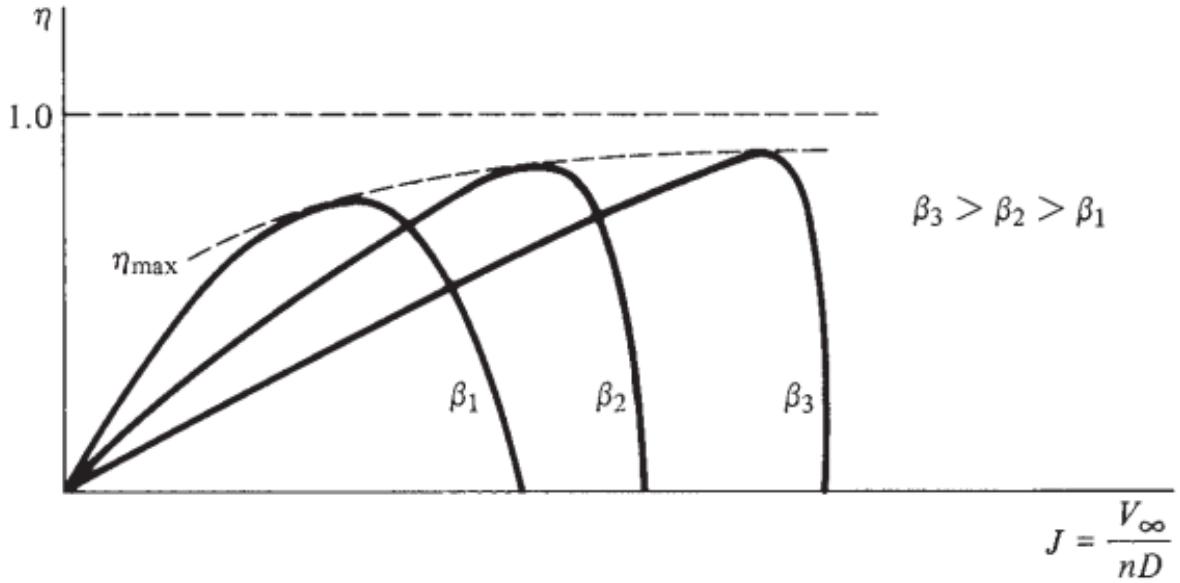

Note. Anderson, 2016.

Considering Equation 2.2, it is clear that J increases as V_∞ does, and Figure 2.12 shows that a sufficiently high advance ratio value severely compromises the propeller efficiency. This phenomenon can be explained by an increase in ϕ, which can even result in a negative angle of attack, as illustrated in Figure 2.13, deterring the use of propellers for transonic and supersonic flight (Anderson, 2016).

Figure 2.13 – (a) High and (b) low V_∞ effect on the angle of attack of a given blade section

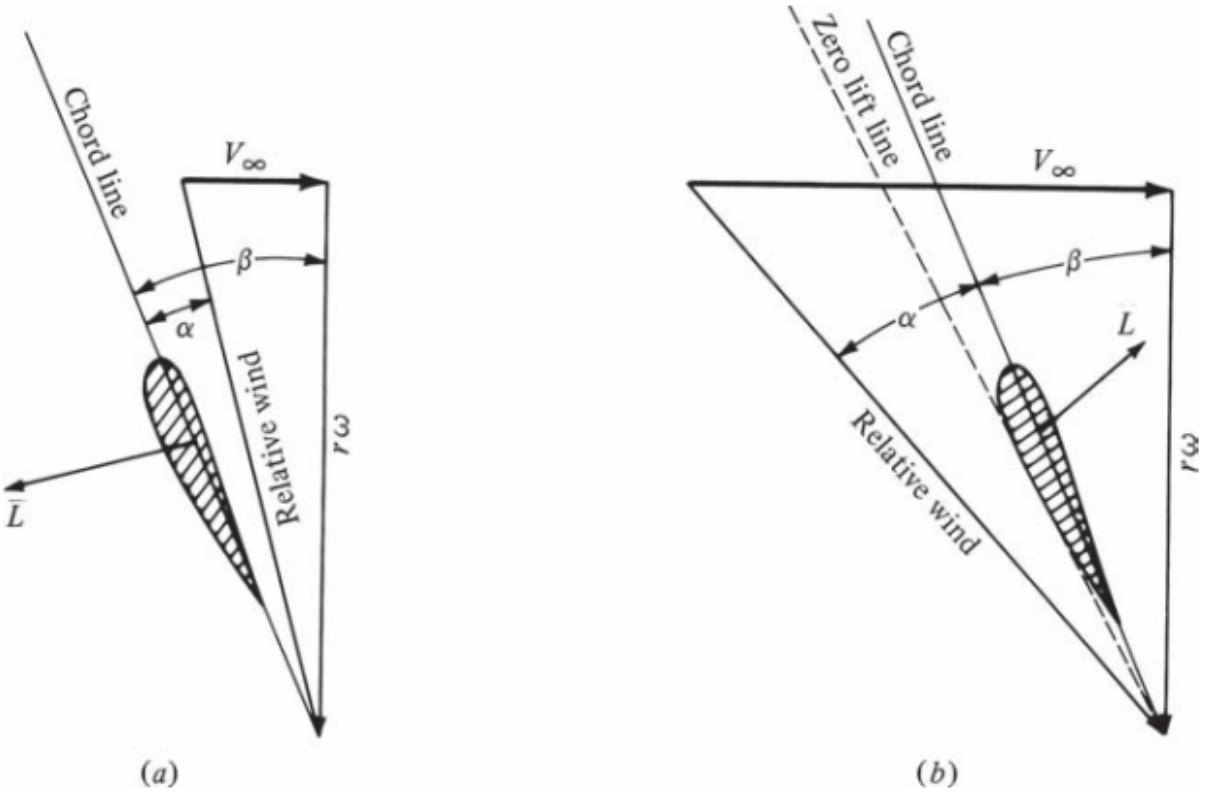

Note. Anderson, 2016.

Finally, it is also important to analyze the slipstream generated by the rotation of the propeller, which is the region where the flow is subjected to a swirl motion, as shown in Figure 2.14. This region decreases in size downstream due to the acceleration effect of the propeller, in order to keep mass flow continuity, in accordance with the actuator disk theory. The propeller is represented, in this theory, by an infinitely thin disk that transmits momentum onto the flow, which is considered incompressible and inviscid (Marcus, 2018). As a result, the axial flow velocity, v_a, steadily increases inside the slipstream, while the tangential velocity, static pressure, P_s, and total

pressure, P_t, are instantly boosted in the disk region (Veldhuis, 2005, as cited in Silveira Filho, 2020).

Figure 2.14 – Streamwise behavior of the axial velocity and pressure

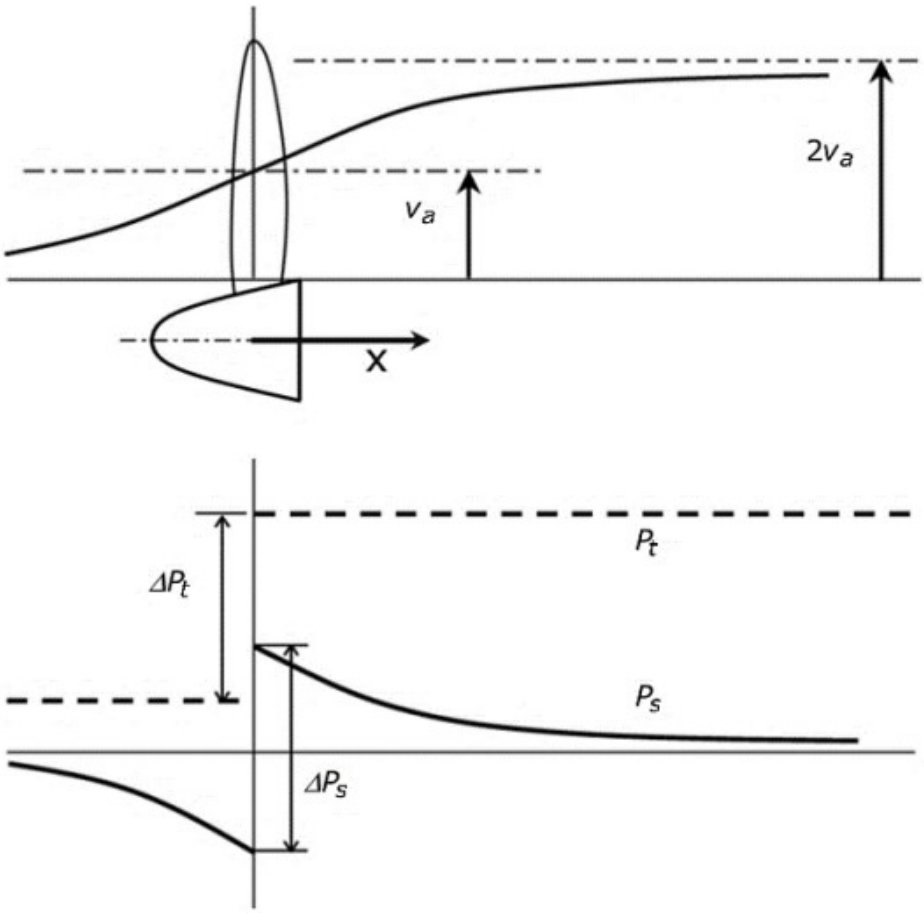

Note. Veldhuis, 2005, as cited in Silveira Filho, 2020.

3 Methodology

This section aims to describe the experiment setup, the 3D-printed model and the experimental procedure, all of which were envisioned for this work. It also presents the numerical setup employed in order to compare the experimental results.

3.1 Experiment setup

This subsection presents the wind tunnel, the wind tunnel balance, the rake probe and the pressure tap reader used to analyze the flow around the wing model as well as the undisturbed flow. Due to geometric constraints as well as instrumentation's sake, the wing model was affixed in front of the wind tunnel's usual test enclosure rather than inside it, as illustrated in Figure 3.1.

Figure 3.1 - Wing model placement

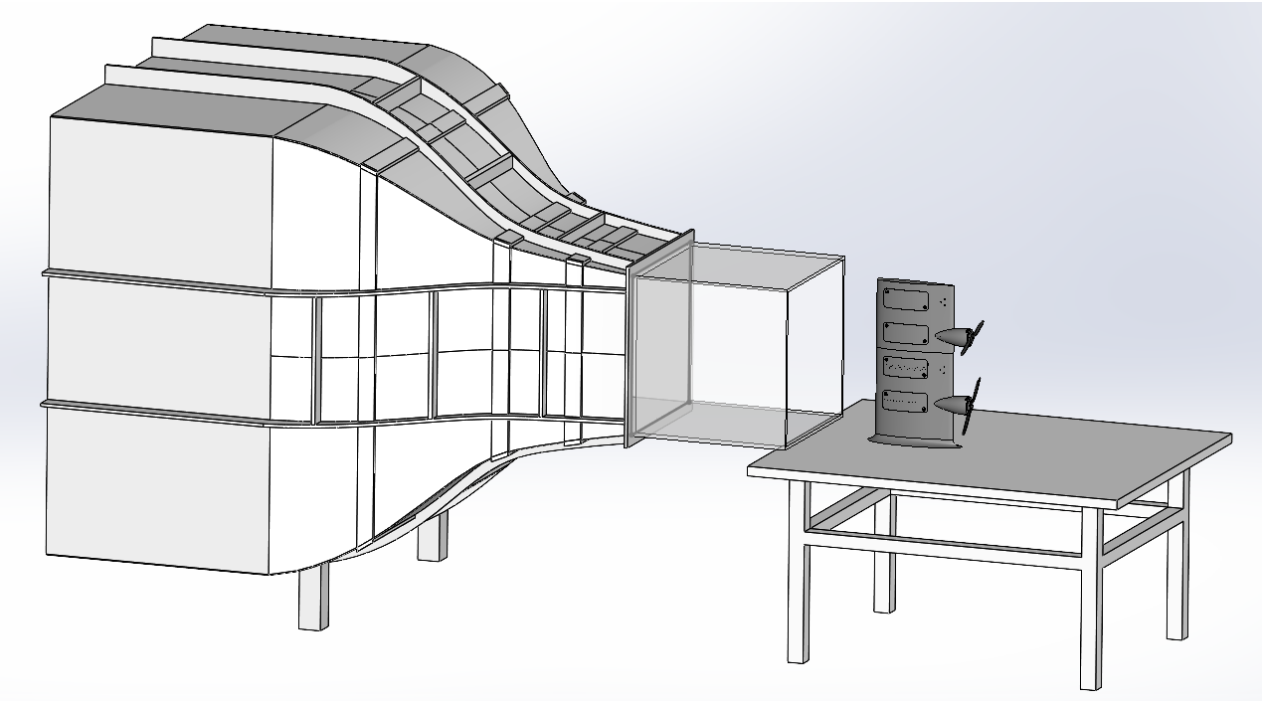

3.1.1 Wind tunnel

It was employed an open section subsonic wind tunnel which has a test section of 60 x 60 x 100 cm, called TV-60-Zephyr. This wind tunnel, depicted in Figure 3.2, is a property of the External Aerodynamic Research Center (CPAERO) based in the 1D building at Federal University of Uberlândia, Glória Campus.

Figure 3.2 - Wind tunnel TV-60-Zephyr

The wind tunnel provides a flow velocity within the range of 0 to 28 m/s, as its electrical inverter varies from 0 to 60 Hz. The air flow is generated by a 12 blade rotor which is powered via a 25 Hp electrical engine, resulting in a turbulence intensity of 0.15 – 0.8% across the speed range. This wind tunnel can also be equipped with a digital thermometer, two models of wind tunnel balances, two pitot tubes as well as vertical and horizontal home-built rake probes for measuring the speed and pressure profiles, all available *in loco*. In this wind tunnel, only very low speed flows are analyzed (corresponding to low Reynolds numbers), with which low speed airfoils, simplified bodies and fundamental fluid dynamics research are employed (Almeida et al., 2017; Alves & Almeida, 2017; Nishioka & Almeida, 2018; Pinto, 2018).

For this project, the TV-60-Zephyr was instrumented with a digital manometer and a pitot tube in order to calibrate it. For analyzing the flow, the tunnel was instrumented with the vertical rake probe, illustrated in Figure 3.3, as well as the bigger wind tunnel balance – due to the scale of the model – and multiple pressure taps.

Figure 3.3 - Wind tunnel test section with rake probe

3.1.2 Wind tunnel balance

The bigger wind tunnel balance, illustrated in Figure 3.4, was custom-made for the CPAERO, being capable of measuring the aerodynamic forces lift drag and lateral as well as the pitch, yaw and rolling moments. The basic principle of this device is to convert pressure readings from the manometer to forces and moments through its 6 components, with its precision detailed in Table 3.1. For this study, only the lift and drag readings provided by the bigger balance were used. As was already mentioned, the laboratory is also equipped with a smaller wind tunnel

balance, comprised of 3 components, which was not employed for this study due to the size of the model.

Figure 3.4 – Six-component external wind tunnel balance

Due to the employment orientation of the wind tunnel balance during the analyses, the resulting lift force was accounted as lateral force, which requires the user to be mindful of the need to adopt the precision parameters of the latter force.

Table 3.1 – Precision parameters of the six-component external wind tunnel balance

	Axis	Minimum Sensibility (in module)	Maximum Load	Range	Accuracy	Precision
Forces	Lift	39 N (1.5% FS)	+/- 2500 N	5000 N	33 N (1.3% FS)	8 N (0.4% FS)
	Drag	17 N (5.6% FS)	+/- 300 N	600 N	15 N (6.0% FS)	4 N (1.3% FS)
	Lateral	15 N (3.0% FS)	+/- 500 N	1000 N	21 N (0.8% FS)	5 N (0.2% FS)
Moments	Pitch	17 N.m (5.6% FS)	+/- 300 N	600 N.m	3 N.m (1.0% FS)	1 N.m (0.3% FS)
	Roll	17 N.m (4.2% FS)	+/- 400 N	800 N.m	8 N.m (2.0% FS)	2 N.m (0.5% FS)
	Yaw	17 N.m (4.6% FS)	+/- 150 N	300 N.m	2 N.m (1.3% FS)	0.5 N.m (0.3% FS)

3.1.3 Digital thermometer

The Minipa MT-455A digital thermometer, placed next to the test section of the wind tunnel, has a thermocouple MTK-01 with resolution of 0.1 °C and accuracy of the read-out of ± 0.5%. This device is depicted in Figure 3.5.

Figure 3.5 – Minipa MT-455A digital thermometer

3.1.4 Rake probe

The rake probe allows for aligned pressure tap readings in order to trace the velocity profile of the undisturbed flow and is illustrated in Figure 3.6. It consists of equally spaced holes through which the pressure taps are inserted into.

Figure 3.6 – Rake probe with pressure taps

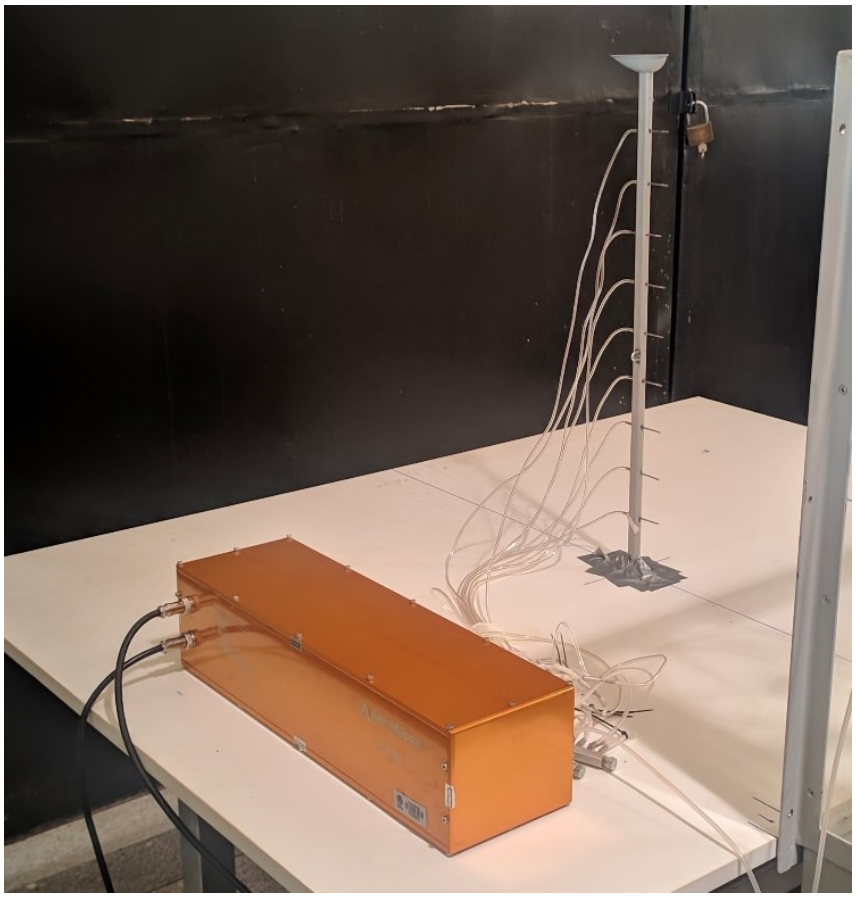

3.1.5 Pressure tap reader

The AA-TVCR2 pressure tap reader, shown in Figure 3.7, is a device intended to trace the pressure profile along any given surface, up to 64 readings simultaneously. For this study, the pressure distribution was measured on both the upper and lower surfaces of the wing model. This was inspired by a precursory work that assessed the pressure distribution on the upper surface of the wing in a similar manner (Marcus et al., 2018).

Figure 3.7 – AA-TVCR2 Pressure tap reader

3.2 The model

This subsection focuses on the 3D modelling and manufacturing of the wing model and the reasoning behind its design choices. Additionally, it presents the remaining non-printed components, which are mainly electronic gizmos.

3.2.1 Model design

The first decision made regarding the wing design was to use an airfoil whose coordinates were easily obtainable and that was commonly used among the bibliography regarding distributed propulsion analyses. However, after some extensive research, it became clear that most studies would either select the same few proprietary airfoils or would each choose a different openly accessible airfoil. Furthermore, in the attempt of being as relatable as possible to previous works, it was decided that the wing would have no taper, sweep, twist nor dihedral, and would be comprised of the same airfoil throughout its wingspan (Khajehzadeh, 2018; Marcus, 2018; Marcus et al., 2018; Silveira Filho 2020). The dimensions and the printed model are shown in Figure 3.8 and Figure 3.9, respectively. The exploded view in Figure 3.10 depicts the internal rods and each

manufactured subcomponent that will be discussed in greater detail in Subsubsubsection 3.2.1.1 and Subsubsubsection 3.2.1.2.

Figure 3.8 – Model dimensions (in millimeters)

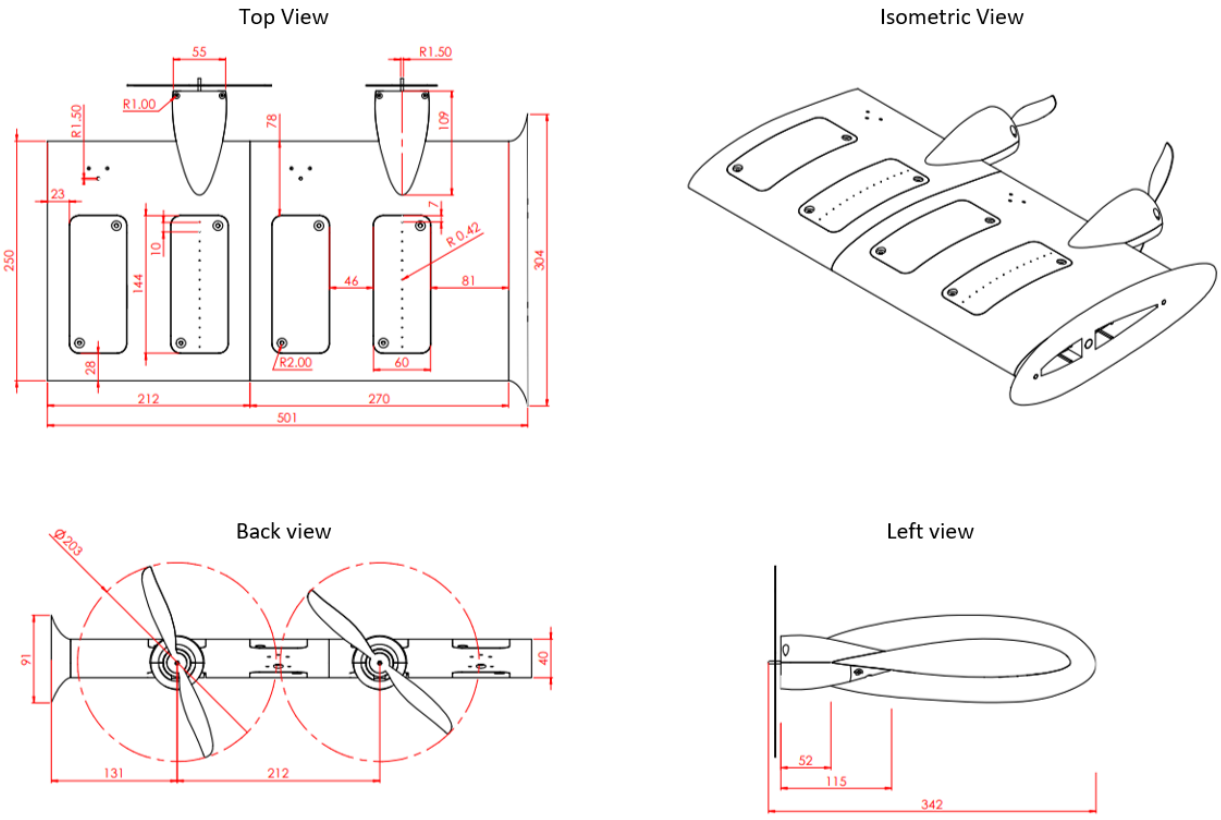

Figure 3.9 – Manufactured model

Figure 3.10 – Exploded view of the entire model

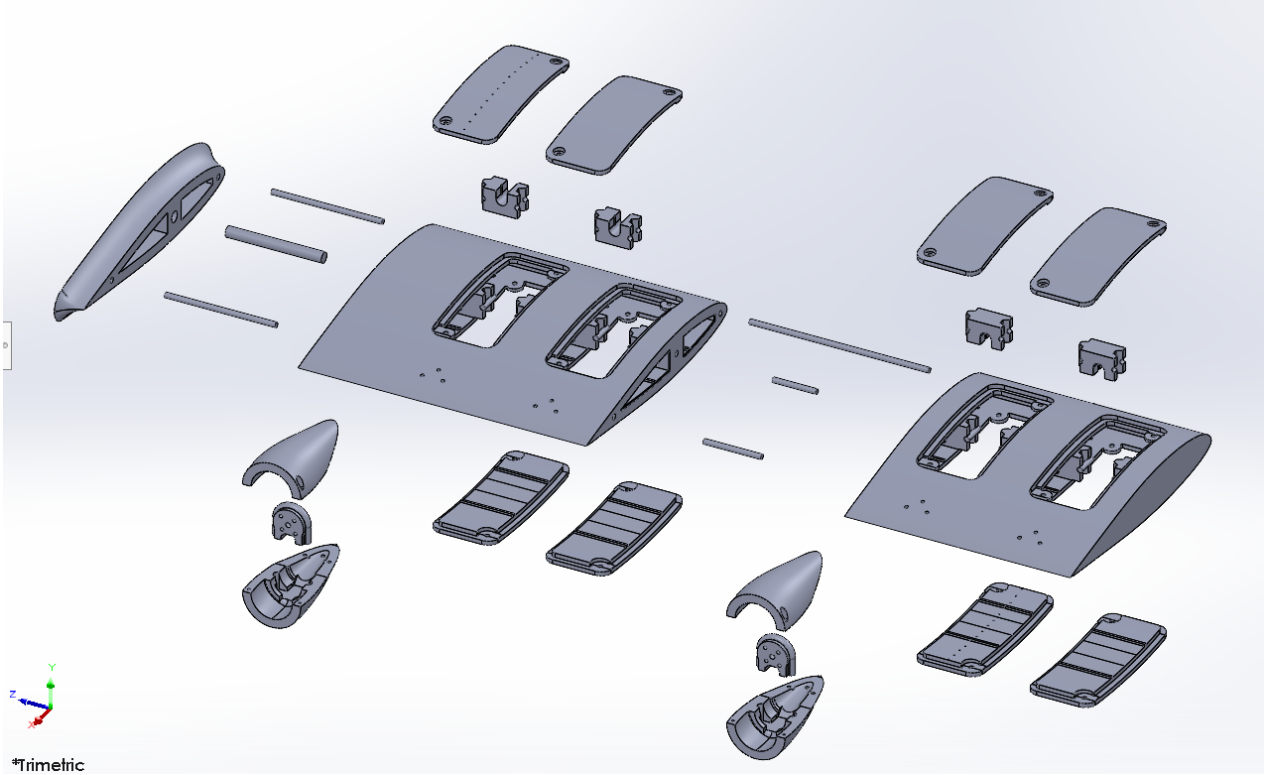

3.2.1.1 Wing

In order to obtain the pressure distribution on the wing, it was imperative that the wing would be hollow and have a big enough thickness-to-chord ratio so that it would be possible to fit inside all the small pressure tap tubes. All this reasoning led to the s8036 airfoil being chosen. The airfoil profile and coordinates are depicted in Figure 3.11 and Table 3.2, respectively.

Figure 3.11 – Airfoil s8036

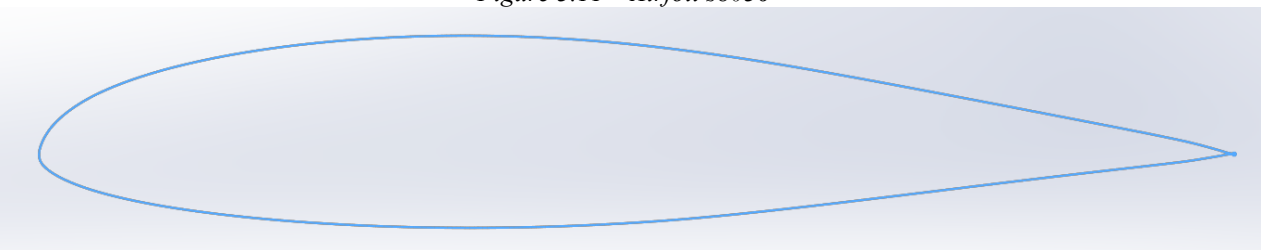

The wing has 4 lateral openings on each side to allow for the placement of the pressure taps as shown in Figure 3.12. This practice of gauging pressure on multiple spanwise locations was also adopted in another study (Veldhuis, 2005, as cited in Silveira Filho, 2020). Due to geometrical constraints, only two rows of pressure taps can fit at the same time in the wing – never at the same wing section. Figure 3.13 illustrates an enclosure with holes to receive the pressure taps, as well as its corresponding wing opening. It is worth mentioning that enclosures without holes were also manufactured.

Table 3.2 - Airfoil coordinates (s8036)

x	y	x	y	x	y	x	y
1	0	0.47611	0.09328	0.00193	0.00823	0.45435	-0.05959
0.99759	0.00046	0.43972	0.09598	0.00001	0.00054	0.49265	-0.05765
0.99095	0.00217	0.40381	0.09776	0.00098	-0.00588	0.53099	-0.05502
0.98105	0.00501	0.36848	0.09853	0.00548	-0.01153	0.56937	-0.05165
0.96827	0.00843	0.3338	0.09838	0.01338	-0.0172	0.60778	-0.04772
0.95247	0.01204	0.29999	0.09735	0.02433	-0.02273	0.64594	-0.04348
0.93354	0.01594	0.26722	0.09547	0.03811	-0.02804	0.68359	-0.03907
0.91163	0.02027	0.23564	0.0928	0.05468	-0.03304	0.72043	-0.03464
0.88697	0.02505	0.20545	0.08939	0.07395	-0.03773	0.75616	-0.03028
0.85984	0.03027	0.17681	0.08528	0.09576	-0.04208	0.79048	-0.02609
0.83047	0.0359	0.14988	0.08053	0.11999	-0.04605	0.82309	-0.02215
0.79916	0.04189	0.12484	0.0752	0.14648	-0.04964	0.8537	-0.01852
0.76618	0.04816	0.10184	0.06934	0.17504	-0.05283	0.88202	-0.01523
0.73183	0.05463	0.08104	0.06296	0.20549	-0.05558	0.90775	-0.0123
0.69641	0.06119	0.06251	0.0561	0.2376	-0.05786	0.93064	-0.0097
0.66022	0.06771	0.04638	0.04885	0.2712	-0.05962	0.95044	-0.00739
0.62357	0.07402	0.03271	0.04115	0.30609	-0.06084	0.96698	-0.00519
0.58668	0.07986	0.02141	0.03305	0.34204	-0.06146	0.98037	-0.00302
0.54969	0.08509	0.01256	0.02483	0.37887	-0.06147	0.9907	-0.0012
0.51279	0.08963	0.00612	0.01649	0.41638	-0.06087	0.99754	-0.0002
						1	0

Note. Retrieved from < http://airfoiltools.com/airfoil/details?airfoil=s8036-il >. Access in January 12th, 2023.

Figure 3.12 – Wing without enclosures

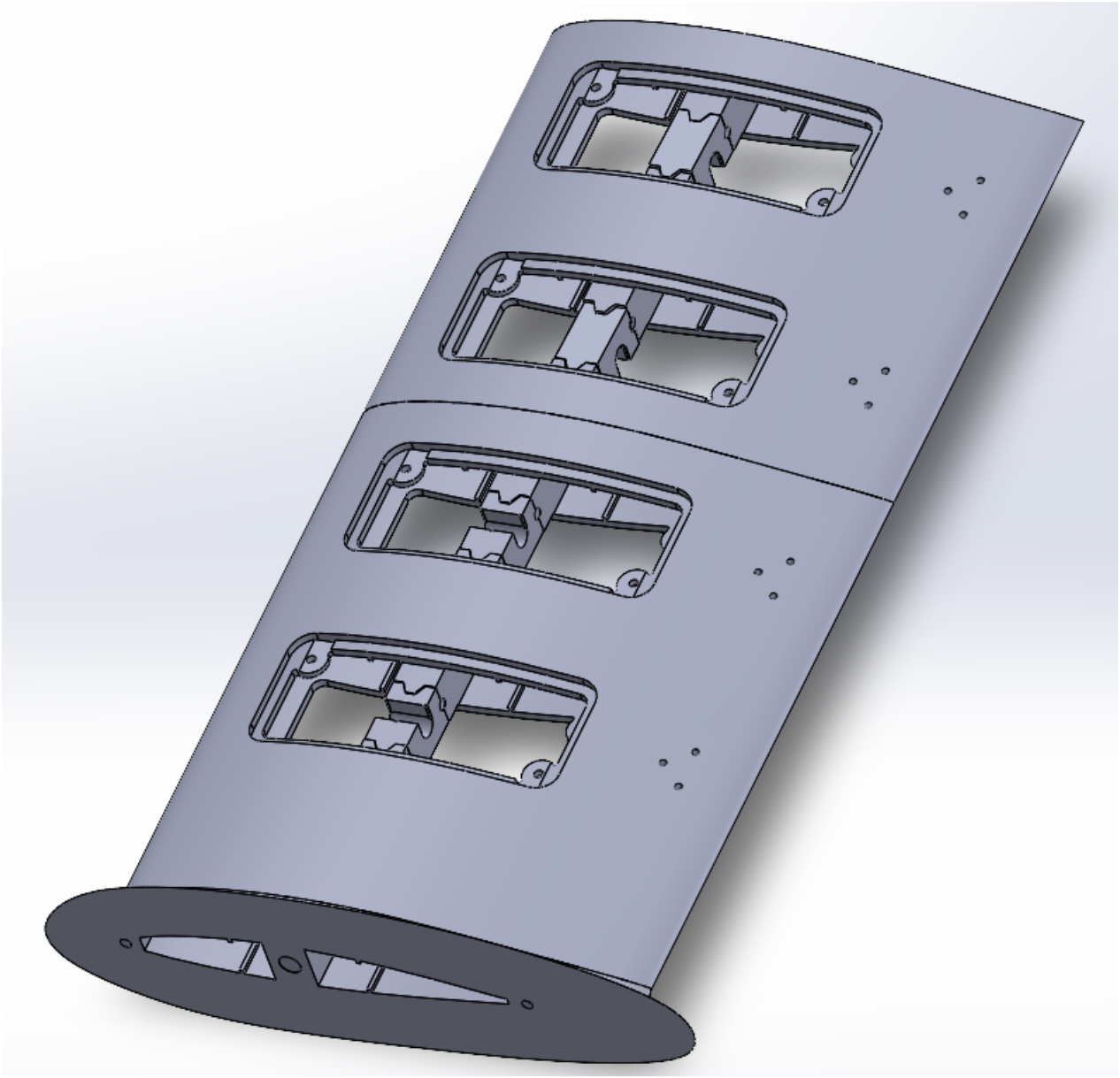

Figure 3.13 – Upper surface enclosure with holes (top) and corresponding wing opening (bottom)

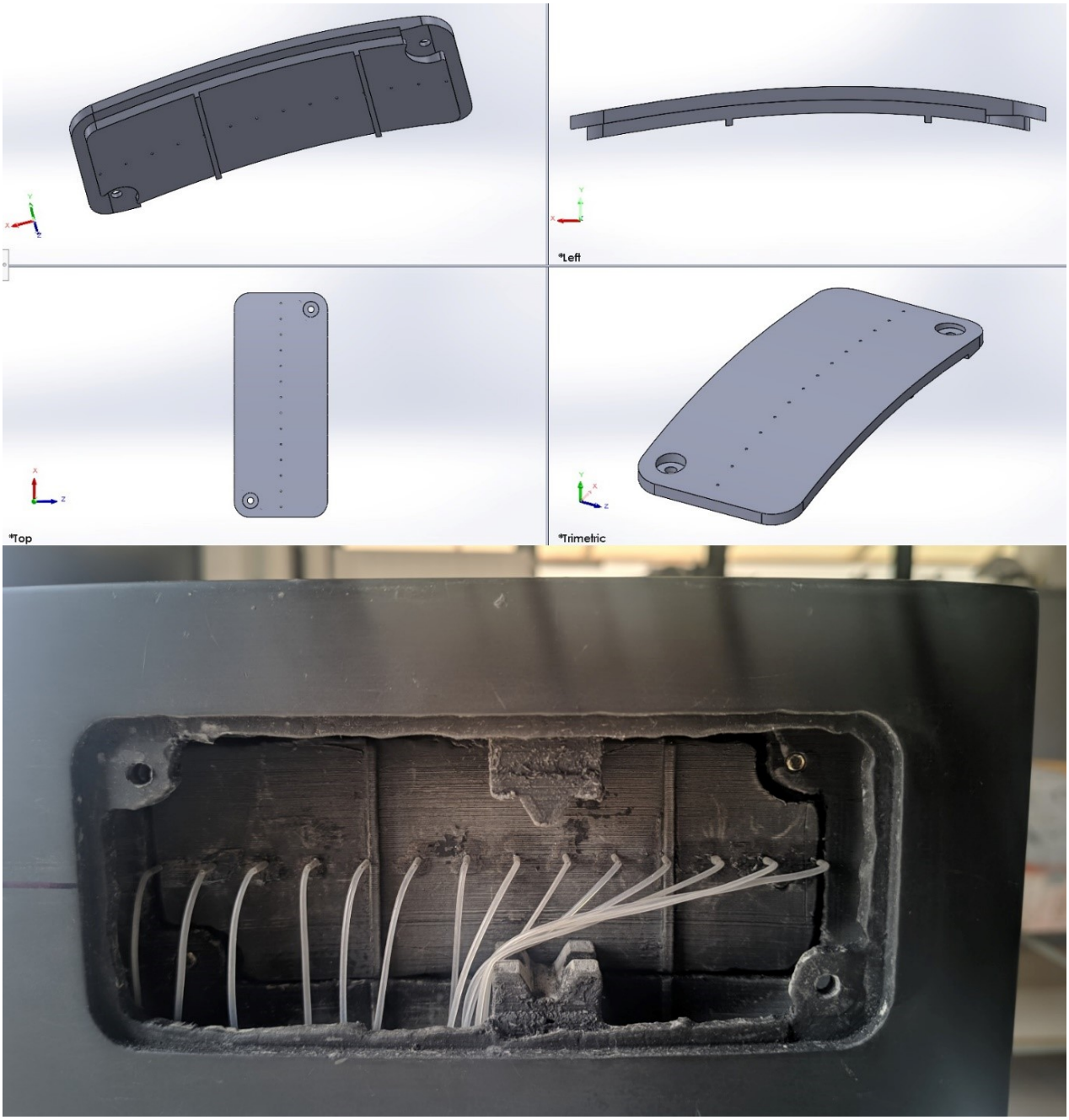

Considering the hollowness of the wing, rudimentary additional structural elements similar to stringers and longerons were implemented. It is worth mentioning, though, that the longerons (unlike the stringers) had to be manufactured in multiple pieces, lessening their structural soundness. This will be further explained in Subsubsection 3.2.2. The main longeron is highlighted

in Figure 3.14. The stringers have the same thickness as all of the four secondary longerons and one of each component is highlighted in Figure 3.15 and Figure 3.16, respectively.

Figure 3.14 – Main wing longeron

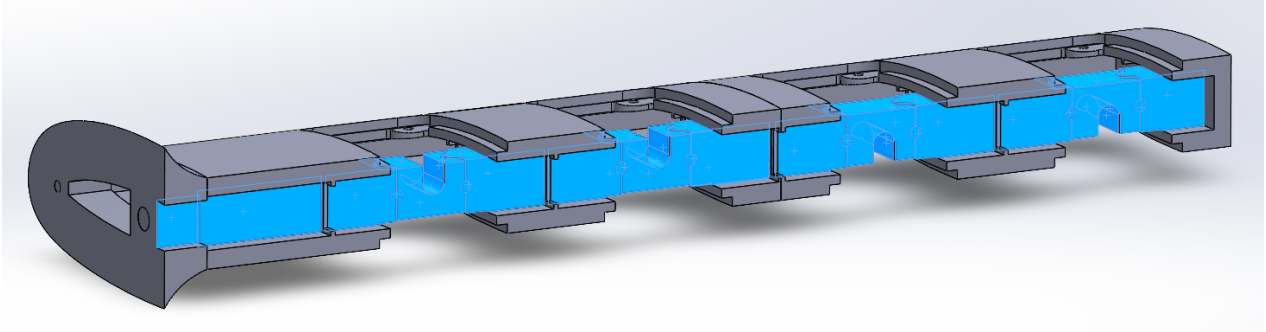

Figure 3.15 – Example of wing stringer

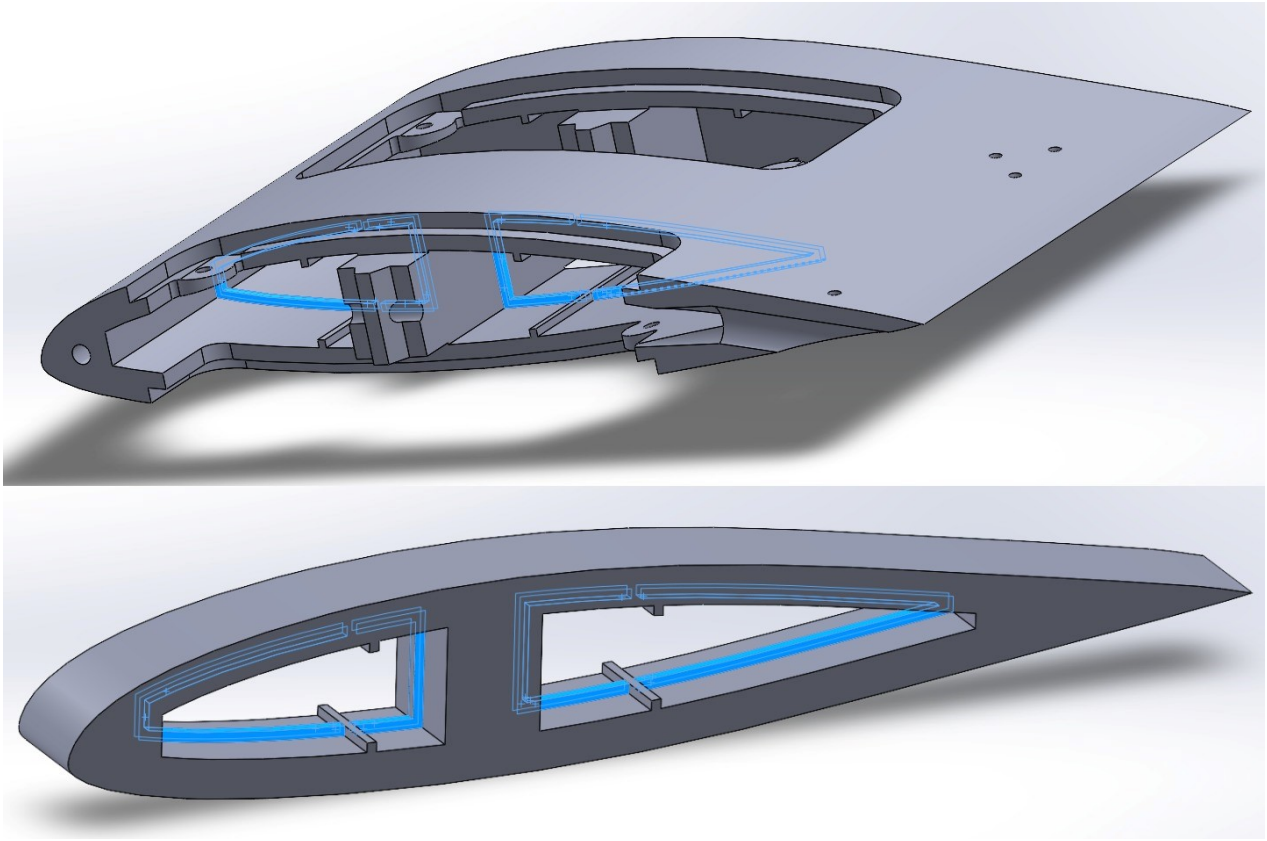

Due to instrumentation requirements, it was imperative for the interior of the wing to have as much empty space as possible, enabling the placement of multiple capillary tubes for the pressure taps – which could not be overly bended nor deformed – as well as the wiring of the drone motors. This especially constrained the maximum thickness of the secondary longerons and the stringers, since the interior cross section area of the wing was already fairly small because of the external dimensions of the model.

Figure 3.16 – Segments of a secondary wing longeron

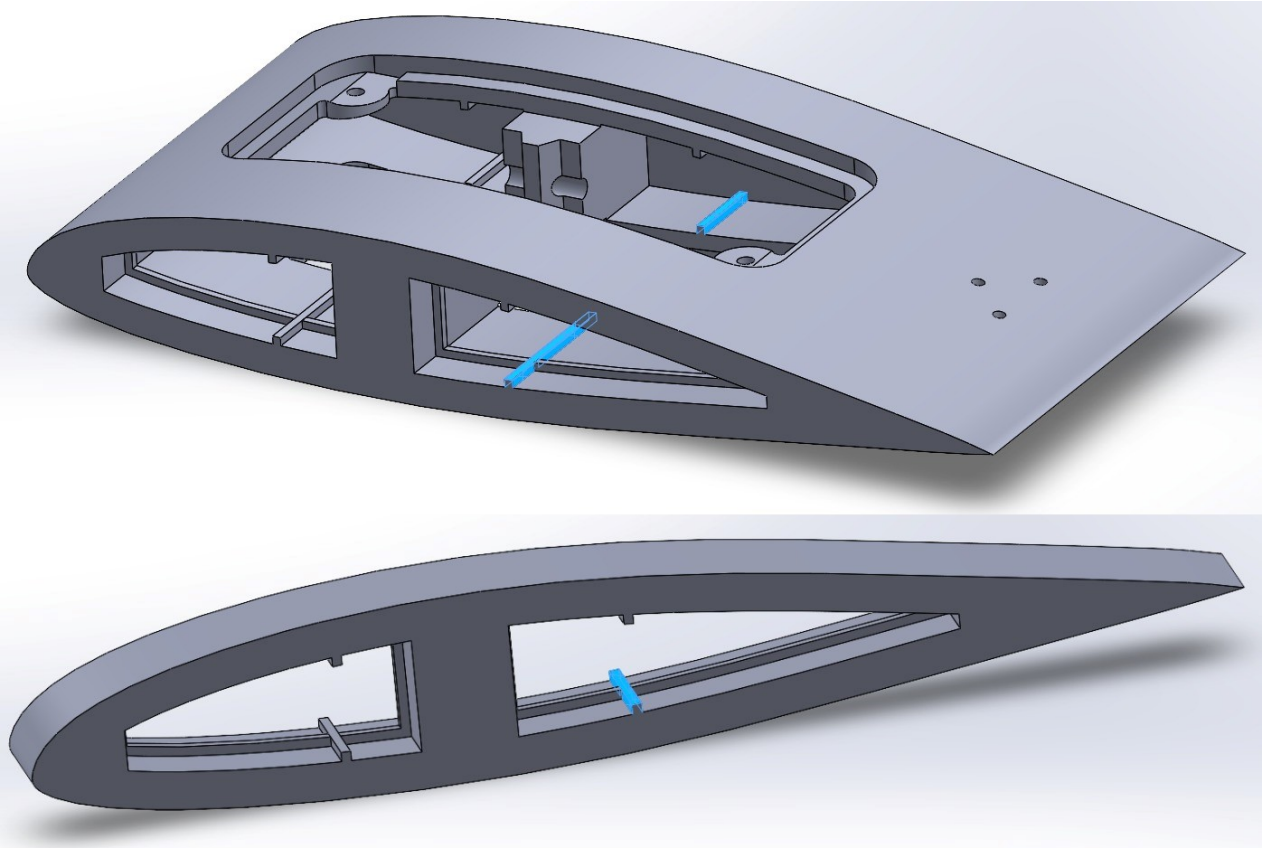

The final part of the wing was its fairing, depicted in Figure 3.17, designed to mitigate the effects of the table (upon which the wing was fixed) on the flow around the wing, distancing the wing itself from the table with a lofted surface that seamlessly transitions from the root section of the wing to a bigger section derived from the same airfoil. This component, therefore, contributes to the resemblance of the experimental flow behavior to the one experienced by a real wing during flight.

Figure 3.17 – Wing fairing

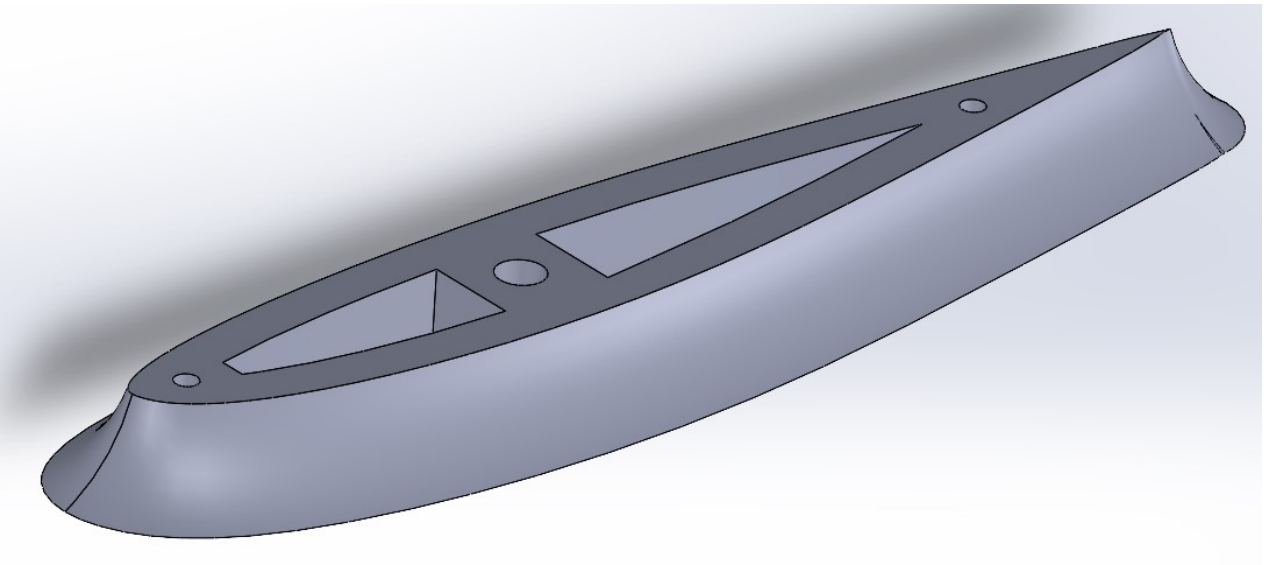

3.2.1.2 Nacelle

The nacelle was designed to house the drone motor and to minimize its form drag as much as possible. As it was essential that this component could be very well fixated to the trailing edge of the wing, considering the vibration of the motor-propeller system and the forces generated by the propeller, the nacelle design would have to be bulky enough to be secured using three screws. This was hindered by the low thickness of the trailing edge of the wing and by the motor cables that needed to cross the nacelle into the wing. The nacelle is portrayed in Figure 3.18.

Figure 3.18 – Nacelle

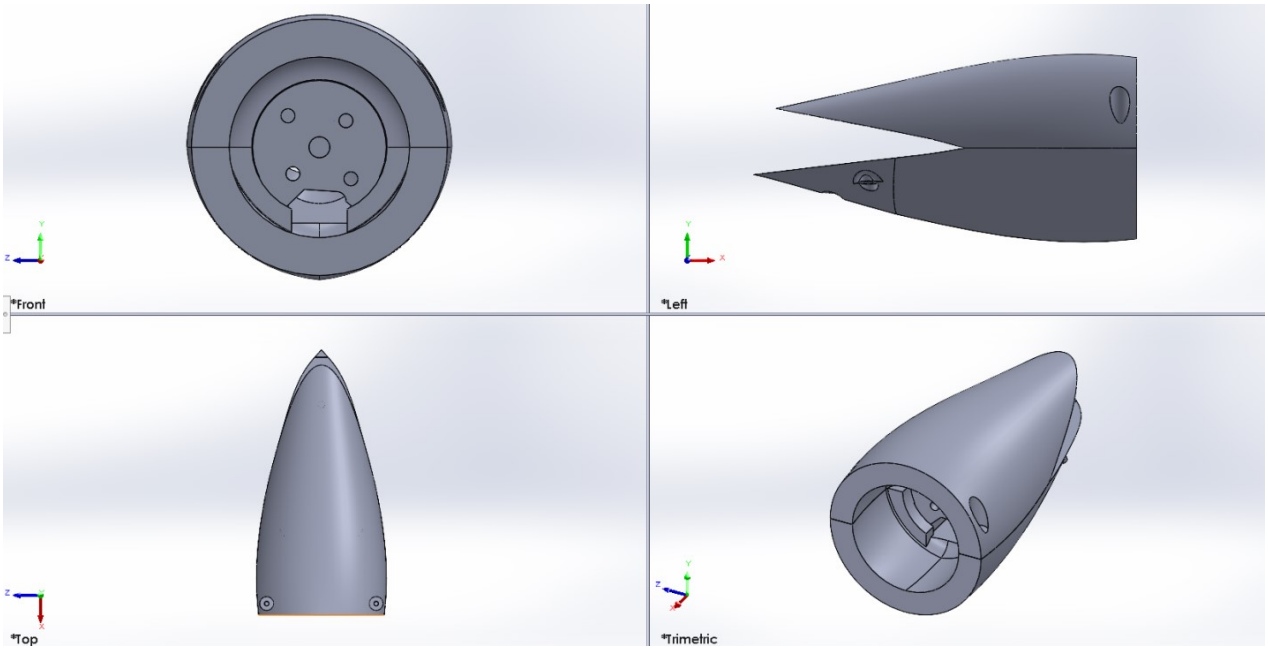

Another requirement was that the nacelle could be opened to insert and extract the motor, which consequently raised the number of screws by 2. The motor itself is only screwed into a third subcomponent, shown in Figure 3.19, which is embedded in the interior of the nacelle, as shown in the exploded view in Figure 3.10.

Figure 3.19 – Motor retainer

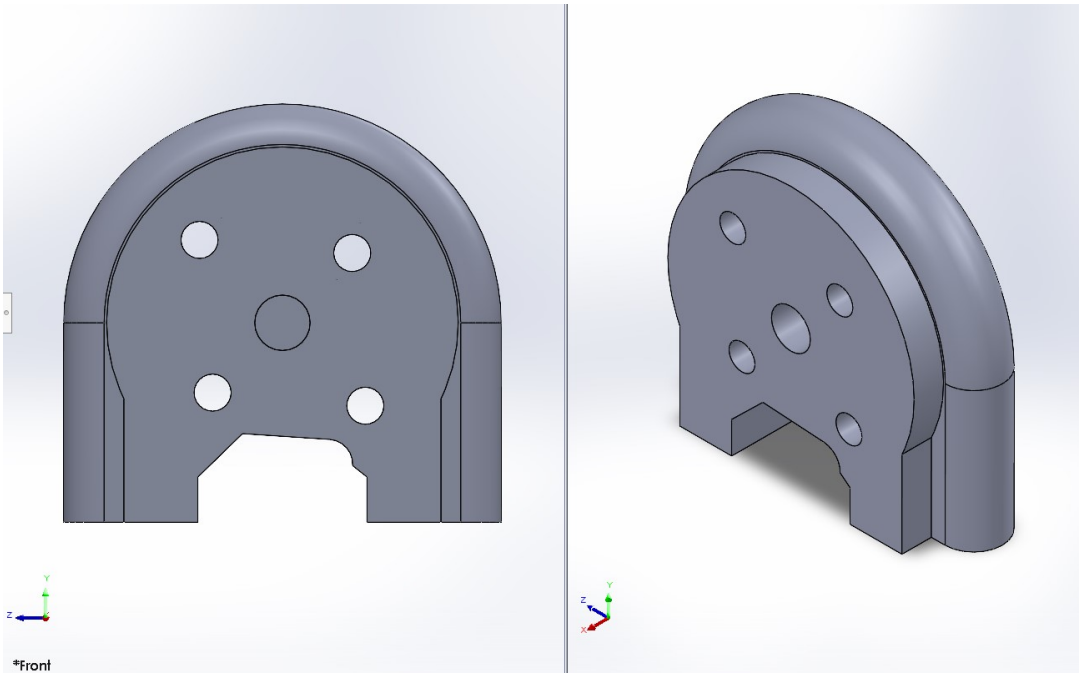

3.2.1.3 Propeller

The propeller chosen was made by APC Propellers and has two blades, 8 inches in diameter and 4 inches in pitch, which is close to 20 cm and 10 cm, respectively. The flow was analyzed with and without the pair of propellers, in order to account for their compound influence in it. Figure 3.20 depicts one of the (identical) propellers.

Figure 3.20 – 8x4 Propeller

3.2.1.4 Drone motor

Considering that the RPM intended for the propeller was significantly lesser than typical drone RPMs, the model Emax XA2212/980 KV was chosen, as it offers a great margin of surplus power, allowing for changes in the target RPM during the tests. Moreover, this model is affordable and is sufficiently compact to fit into the nacelle. Figure 3.21 depicts the drone motor adopted.

Figure 3.21 – Drone motor Emax XA2212/980 KV

3.2.1.5 Power Supply Unit

The drone motors were powered by a Power Supply Unit (PSU), typically employed for PC use, which would provide all the power needed even when testing both propellers at the same time. The Bluecase BLU500R-BCASE model was chosen due to its high wattage, low noise and reliability. Figure 3.22 illustrates the PSU chosen.

Figure 3.22 – Power supply unit BLU500R-BCASE

3.2.1.6 Arduino UNO

A microcontroller board was used in order to set the RPM of the propellers via laptop input, as precisely as possible. The Arduino UNO was chosen due to its libraries galore as well as its community of users, simplifying the implementation of the board. Figure 3.23 illustrates the microcontroller chosen.

Figure 3.23 – Microcontroller board Arduino UNO

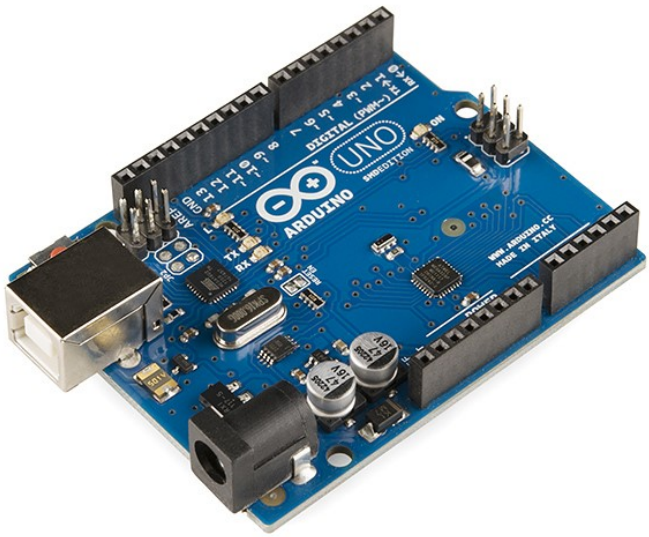

3.2.2 Model manufacture

Considering the intricacy of the model design – especially in its interior – which has multiple details with considerable small dimensions, the best viable manufacture option would be 3D printing. This method would also help alleviate the model's final weight, since the model did not need to be solid. The 3D printer employed was the MakerBot Replicator Z18, illustrated in Figure 3.24, with a PLA filament of 1.75 diameter in millimeters.

Figure 3.24 – MakerBot Replicator Z18 3D printer

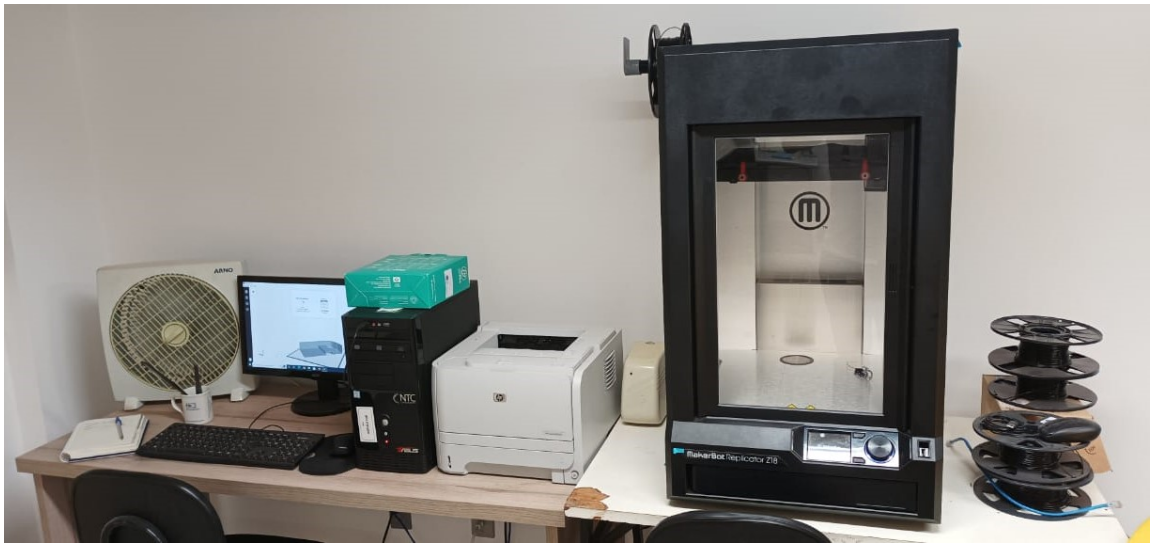

One notable drawback of this method of manufacture is its maximum dimension constraints that caused the wing model to be produced in multiple parts. This not only upped the number of internal rods required (which would be unitary, had the model been manufactured whole) but also raised the stakes of superficial smoothness, since superficial offsets between the parts could impact the flow around the wing. On top of that, it was expected that the external superficial smoothness of all parts would not be adequate right after the printing process. To solve that, the model was carefully sanded, glued together and then painted, permanently joining the wing sections, wing fairing and the internal rods together. The other parts, such as the nacelle halves, were not glued, but did receive the remaining post-printing procedures.

3.3 Locations of measurement

This subsection describes all the locations utilized to obtain pressure and other aerodynamic readings.

3.3.1 Rake probe

This probe was employed to analyze the undisturbed flow on three locations: at the outnozzle, at 21 cm from the outnozzle and at the rotating point of the wing (where one of the wing's rods would be positioned during the study, later on). This would guarantee that the flow in the test section of the wind tunnel is sufficiently undisturbed in order to analyze the flow around the wing.

3.3.2 Wing

The wing has four spanwise locations for the placement of nacelle + propeller and the placement of the pressure taps, ranging from the tip to the root of the wing, as illustrated in Figure 3.25. For the pressure taps' location, the placement options double, since each of the four nacelle + propeller attachment sites has one option in the upper surface and another in the lower surface of the wing. In those cases, it will be added to the location numbers the letters *U* and *L*, respectively.

Figure 3.25 – Locations for placement of nacelle + propeller on the wing, with pressure taps in location U4 as an example

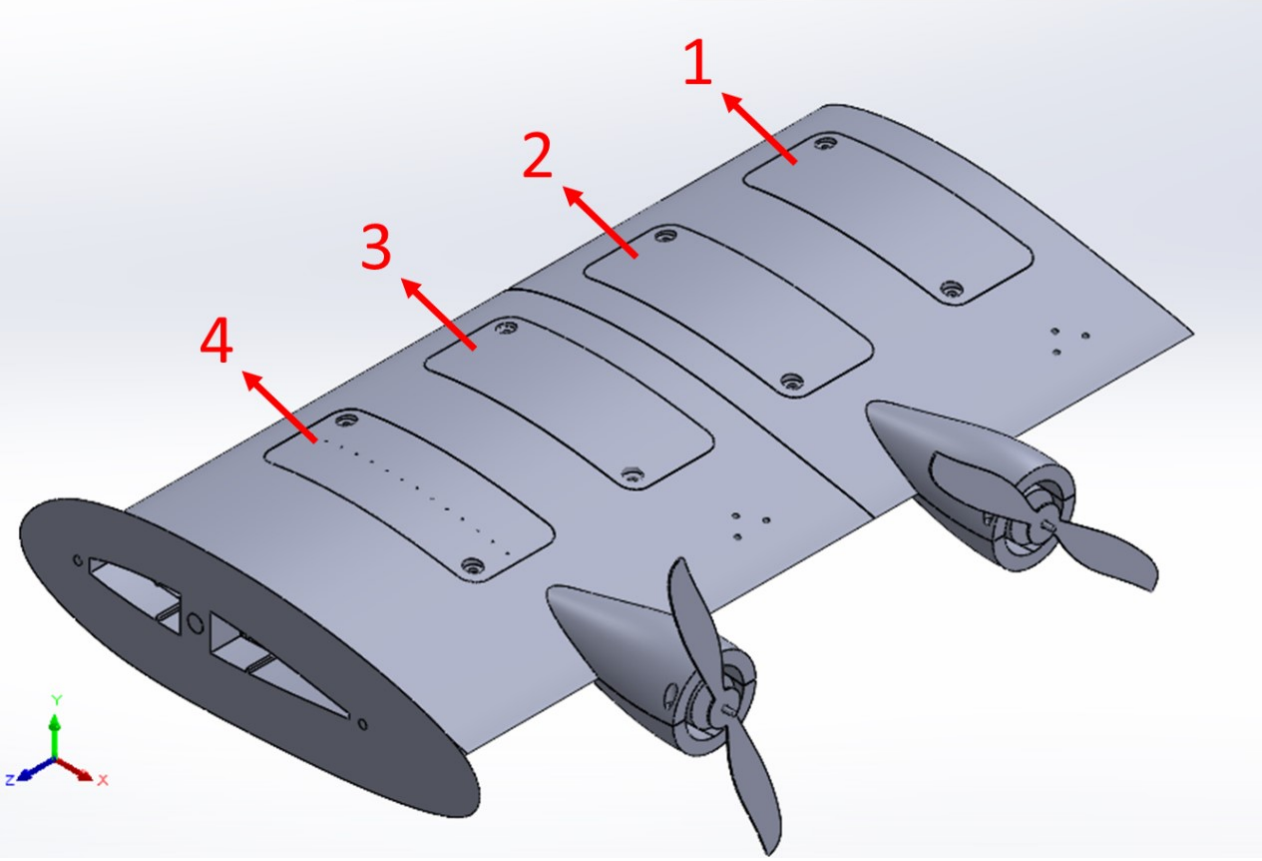

3.4 Test conditions

The experiments were performed employing the wind tunnel flow velocity (V_∞) set to 18 m/s, providing an even flow condition throughout all wind tunnel sessions. Since multiple days were required to run all experiments, the air density had to be calculated every test day, using the current temperature and relative humidity of the ambient as well as the atmospheric pressure. In spite of the daily variations, the density (ρ) was always close to 1.17 kg/m^3. The kinematic viscosity (ν) also varied little over time, sticking around $1.56 \times 10^{-5}\ m^2/s$. In the same fashion, the Reynolds number (Re) never deviated much from 2.88×10^5.

3.4.1 Boundary layer thickness

In order for the wing fairing, depicted in Figure 3.17, to be effective, it is instrumental that the boundary layer thickness of the table – upon which the wing model is placed – be shorter than the height of the fairing. Firstly, it is necessary to estimate the point at which the flow becomes turbulent. Considering a flat plate, a generally accepted consideration is that the critical Reynolds number is around 5×10^5, which can be employed by Equation 3.1 to estimate the transition (Anderson, 2016).

$$Re_{x_{crit}} = \frac{V_\infty * x_{crit}}{\nu} \rightarrow 5 * 10^5 = \frac{18 * x_{crit}}{1.56 * 10^{-5}} \therefore x_{crit} = 0.43\, m \quad (3.1)$$

Since the length of the wind tunnel + wing fairing is equal to 1.37 m – which is bigger than 0.43 –, the wing fairing is located inside the turbulent boundary layer. The next step is to estimate the maximum thickness of the turbulent boundary layer, located at the trailing edge of the wing fairing, for the boundary layer gets thicker the further it travels from the starting point on a given surface. Equation 3.2 allows for this estimation to be made.

$$\delta_{turb} = \frac{0.37 * x}{Re_x^{0.2}} \rightarrow \delta_{turb} = \frac{0.37 * x}{\left(\frac{V_\infty * x}{\nu}\right)^{0.2}} \rightarrow \delta_{turb} = \frac{0.37 * 1.37}{\left(\frac{18 * 1.37}{1.56 * 10^{-5}}\right)^{0.2}} \therefore \delta_{turb} = 0.029\, m \quad (3.2)$$

This result indicates that it is likely that the wing fairing may not distance the wing model from the boundary layer on the table enough, given that the fairing height is only 0.020 m – which is lower than the estimated boundary layer thickness. As a consequence, the experimental results may be tainted by a boundary layer that is not present in a real wing during cruise flight.

3.4.2 Wind tunnel readings setup

Initially, the wing model was rotated to the required angle of attack, with the desired placement of the propellers, except if the experiment employed only the clean wing. Then, the wind tunnel was turned on and the readings were taken every 200 ms, starting after the flow stabilized near the desired speed, until the threshold of 600 readings was achieved. In sequence, the mean of those readings would be calculated, with its respective standard deviation. Finally, the

wind tunnel was turned off. This procedure was repeated for every configuration and angle of attack.

3.4.3 Pressure tap reader readings setup

Firstly, the wing model was rotated to the require angle of attack, with the desired placement of the propellers, except if the experiment employed only the clean wing. Additionally, the pressure taps were placed on the necessary wing enclosures and then the pressure tap reader was turned on. After this device was ready to initiate pressure readings, the wind tunnel was turned on, and as soon as the flow had stabilized near the required speed, the readings would be taken in an interval of 100 ms, up until around 600 readings were obtained for each of the wing enclosures with the pressure taps on. Then, the wind tunnel was turned off and on again, and after the flow had stabilized, the readings were retaken. This step was repeated once more, totalizing 3 groups of around 600 readings each for each of the enclosures with the pressure taps on. Finally, the total sum of the readings of each of the wing enclosures with the pressure taps on was saved to their respective data files, and their corresponding mean of the first 1700 readings was calculated with their respective standard deviations. This procedure was performed for every configuration, angle of attack and set of pressure tap locations on the wing.

3.5 Experimental procedure

This subsection describes each experiment performed for this study, with each wing configuration employed illustrated in Figure 3.26. Firstly, it was studied the undisturbed flow, followed by the flow around the “clean wing” – explained further along this subsection – and, finally, the wing + both propellers. For the analysis requiring pressure readings, such as the ones of the undisturbed flow, the pressure tap reader was employed. Each analysis is cited by chronological order in the list below.

- **[Analysis 1]** The undisturbed flow, using the rake probe, as cited in Subsubsection 3.3.1, on three different locations: at the outnozzle, at 21 cm from the outnozzle and at the rotating point of the wing. It is worth mentioning that this rotating point does not coincide with the aerodynamic center nor is it placed on the chord line, for the sake of the structural integrity of the wing model.
- **[Analysis 2]** The clean wing, for the following angles of attack: 2° and 4°. For this step the pressure taps were used, measuring the pressure differential in the following pairs of locations: U1 + L4, U4 + L1, U2 + L3 and U3 + L2.
- **[Analysis 3]** The clean wing, meaning the wing without the propellers and the nacelles, for the following angles of attack: -6°, -4°, -2°, 0°, 2°, 4°, 6° and 8°. For this step the wind tunnel balance was used.
- **[Analysis 4]** One propeller in location 1 of the wing, for the following angles of attack: 2° and 4°. For this step the pressure taps were used, measuring the pressure differential in location U1.
- **[Analysis 5]** The wing + two propellers on the locations 1 + 3 and 1 + 4, for the angle of attack of 4°. For this step the pressure tap reader was used to measure the pressure differential in the following pairs of locations: U1 + U3 and U1 + U4.
- **[Analysis 6]** The wing + two propellers on the locations 1 + 3 and 1 + 4, for the following angles of attack: 2° and 4°. For this step the wind tunnel balance was used.

In addition to the six analyses described above, other analyses were performed, regarding the single-engine configuration: the placement of the propeller from location 2 to location 4 of the wing – employing the wind tunnel balance as well as the pressure taps – and the use of the wind tunnel balance for the analysis of the single propeller placed on location 1 of the wing. Unfortunately, their corresponding results were lost due to an error in data transferring, and could not be reacquired in compliance with the pandemic restrictions discussed in Section 1.

Figure 3.26 – Wing configurations analyzed in the wind tunnel

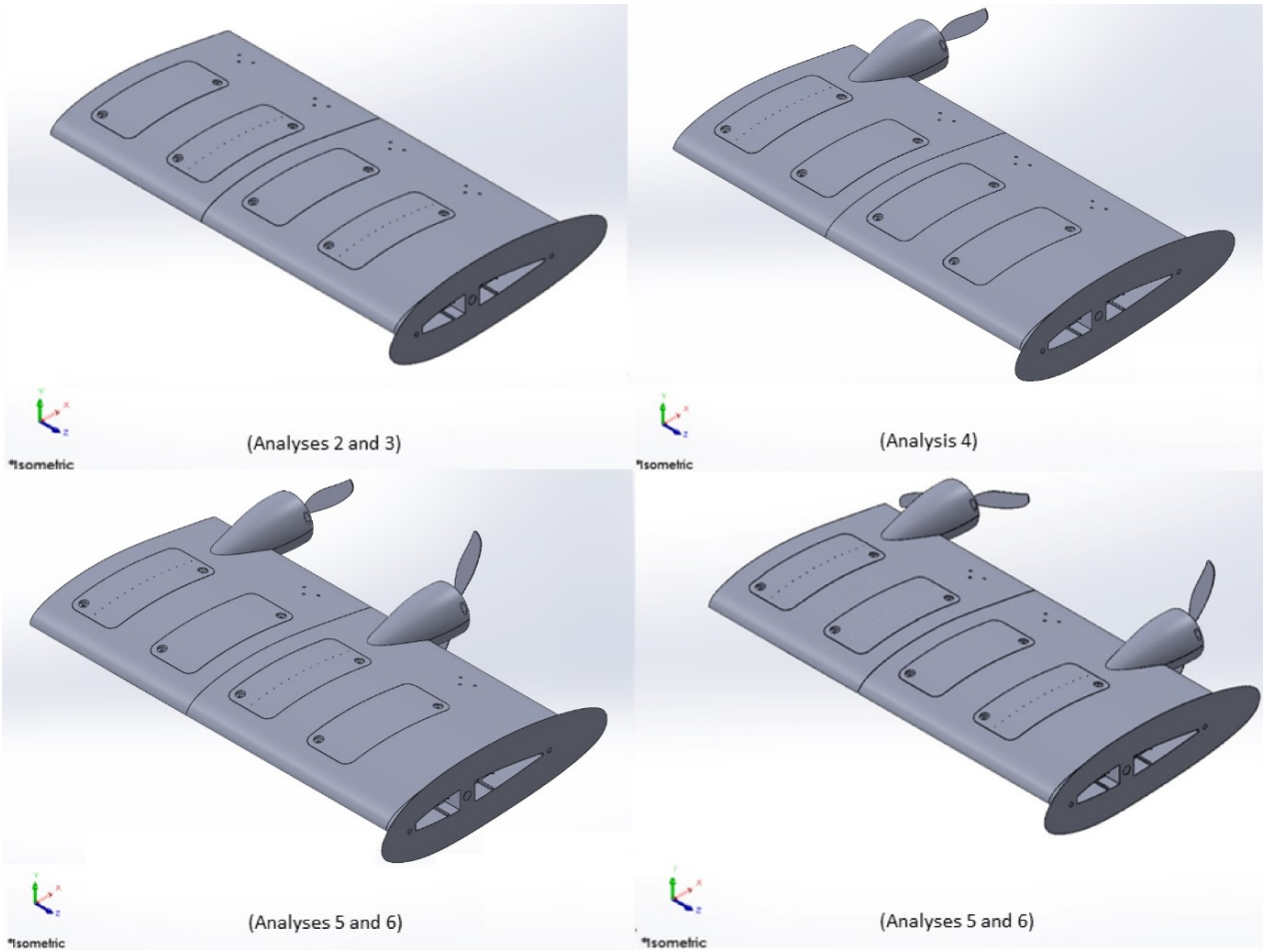

3.6 Numerical procedure

This subsection delineates the numerical procedure employed to compare its findings to some of the experimental results. The clean wing model was implemented in software Xflr5, with the following conditions: $V_\infty = 18\, m/s, \rho = 1.17\, kg/m^3$ and $\nu = 1.56 \times 10^{-5}\, m^2/s$. The analysis is described below.

1. The clean wing, for a series of angles of attack ranging from -6° to 8°, with increments of 0.5°.

The ring vortex method, which is a type of potential flow method, was applied for this analysis, with the viscosity toggle enabled, and the panel distribution of the wing, as well as the streamlines around it, are presented in Figure 3.27.

Figure 3.27 – Panel distribution of the wing (top) and streamlines around the wing (bottom)

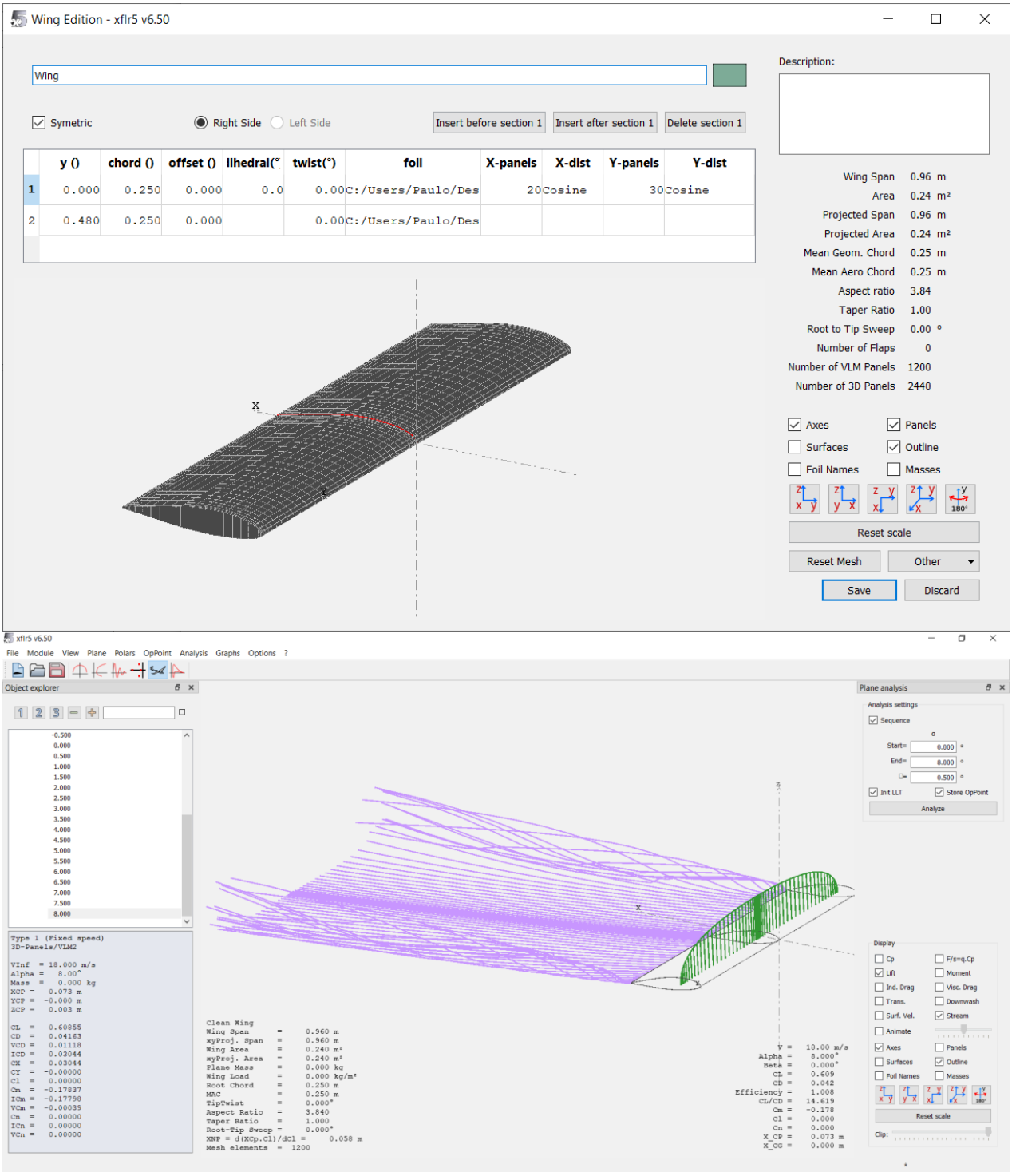

The potential flow methods assume that the flow is incompressible, irrotational and inviscid, which means that they disregard the boundary layer and its effect on the flow dynamic. This creates a significant limitation, especially considering the scope of this project: those methods cannot adequately account for flow separation, since this is a viscosity-driven phenomenon. Additionally, the calculated lift is a linear function of the angle of attack, which is patently not physically accurate, since the lift polar tends to lose its linearity for high angles of attack. Another major drawback, considering the low Reynolds number employed in this work, is that those methodologies are best suited for high Reynolds numbers, since the higher this number is, the less influence the viscous forces have over the given flow (Deperrois, 2019).

4 Results

This section presents the experimental results from the six analyses detailed in Subsection 3.5, along with the numerical comparison – when relevant – presented in Subsection 3.6. Both results are then analyzed and compared. The experimental results are separated in four parts, based on the main configurations analyzed: the rake probe alone, the clean wing, the wing with a single propeller and the wing with two propellers, as illustrated in Figure 3.26.

4.1 Rake probe

This subsection introduces the velocity profile of the flow in the test section of the wind tunnel obtained from three different locations during **Analysis 1** (without the wing model), as stated in Subsection 3.5: at the outnozzle, at 21 cm from the outnozzle and at the rotating point of the wing. The results are depicted in Figure 4.1.

Figure 4.1 – Velocity profile of the flow in the test section

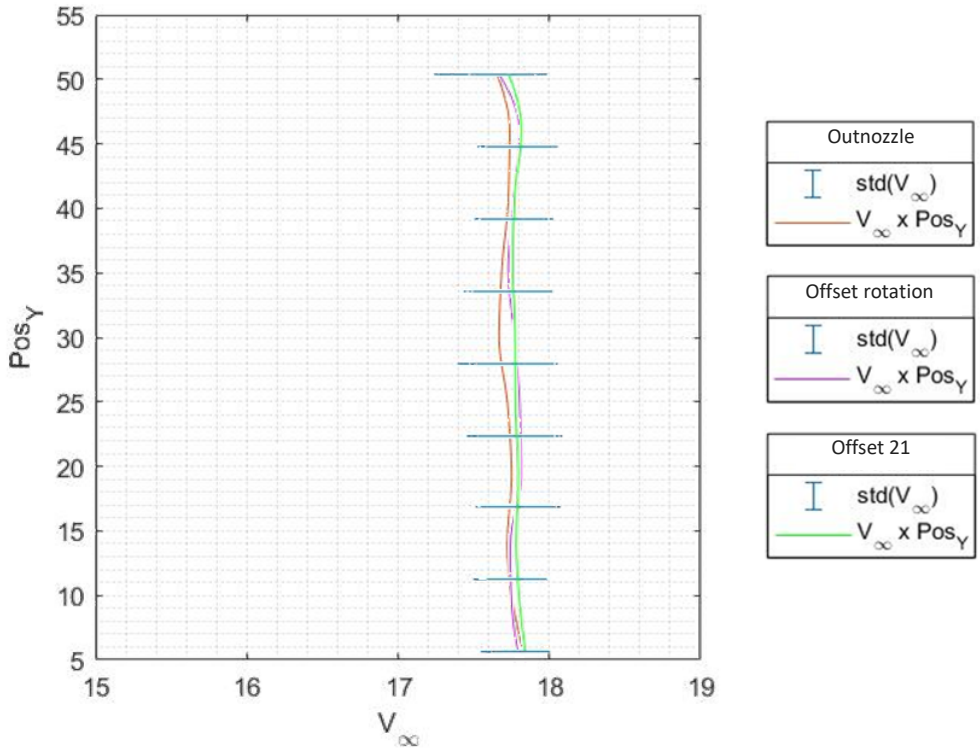

The velocity profiles in those different locations are very well matched, which contributes to corroborate that the flow coming out of the wind tunnel is well suited for performing experiments. Another important observation towards this corroboration is that the flow in all locations does not, indeed, vary considerably along the vertical axis.

4.2 Clean wing

This subsection portrays the pressure distribution obtained on the clean wing (without the propellers) in all of its eight locations (U1, U2, U3, U4, L1, L2, L3, L4), as shown in Figure 3.24, during **Analysis 2**. For each location, it was implemented two angles of attack: 2° and 4°, which are presented in Figure 4.2 and Figure 4.3, respectively. Then, it is shown the results acquired during **Analysis 3** using the wind tunnel balance, employing the following angles of attack: -6°, -4°, -2°, 0°, 2°, 4°, 6° and 8°. A comparison of the lift and drag polars between the wind tunnel balance and the numeric result is shown in Figure 4.4 and 4.5, respectively.

Figure 4.2 – Pressure distribution on the clean wing (AoA = 2°)

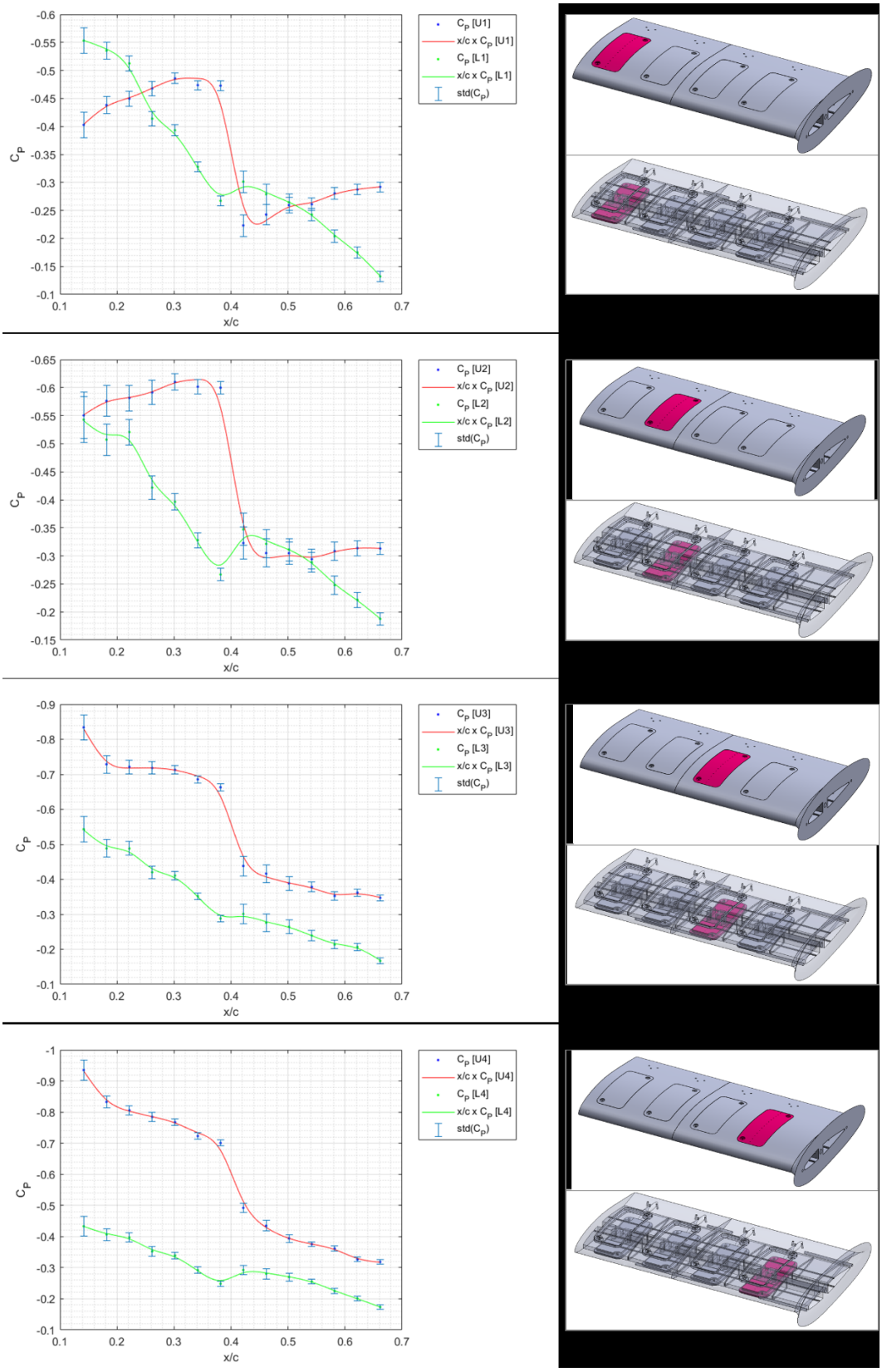

The C_P distribution for AoA = 2° is increasingly more negative on the upper surface of the clean wing in the direction of the wing root. Additionally, the suction peak is clearly showcased in all four upper surface distributions, always extending until 40% of the chord, approximately. Immediately further along the chord, a recirculation bubble – or flow separation – occurs, being indiscernible from each other given that no supplementary analyses, such as smoke or china clay flow visualization, were performed. On the lower surface, the C_P distribution tended to get less negative from the tip of the wing towards the root. The resulting phenomenon, considering both upper and lower surfaces distributions, is an increase in the pressure gradient around the wing towards the leading edge and the wing root, which corroborates the lift distribution displayed in Figure 3.26. The decrease in said gradient towards the trailing edge is noticeable in the difference between the upper surface distributions – where the C_P gets closer to zero past the suction peak – and in the lower surface distributions, where the same coefficient nears zero next to the trailing edge. Finally, it is worth noting that the distribution in the lower surfaces barely differs from each other, suggesting that the flow behavior on this region is much more uniform than that of the upper surface.

Figure 4.3 – Pressure distribution on the clean wing (AoA = 4°)

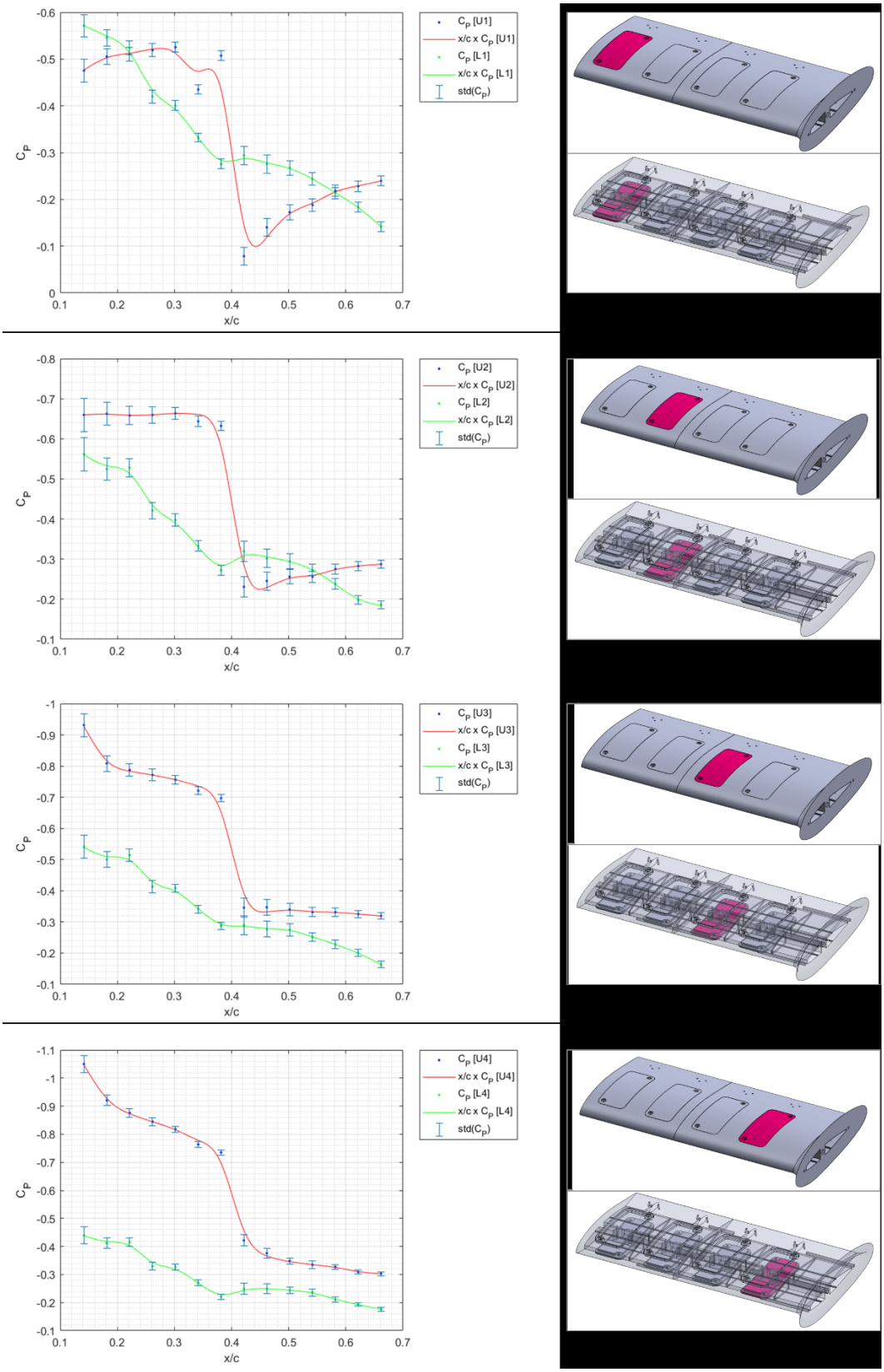

The same remarks made for the C_P distribution for AoA = 2° can be made for AoA = 4°. This is not surprising, considering that in both cases the angles of attack are rather small and close to each other.

Figure 4.4 – Lift polar comparison for the clean wing

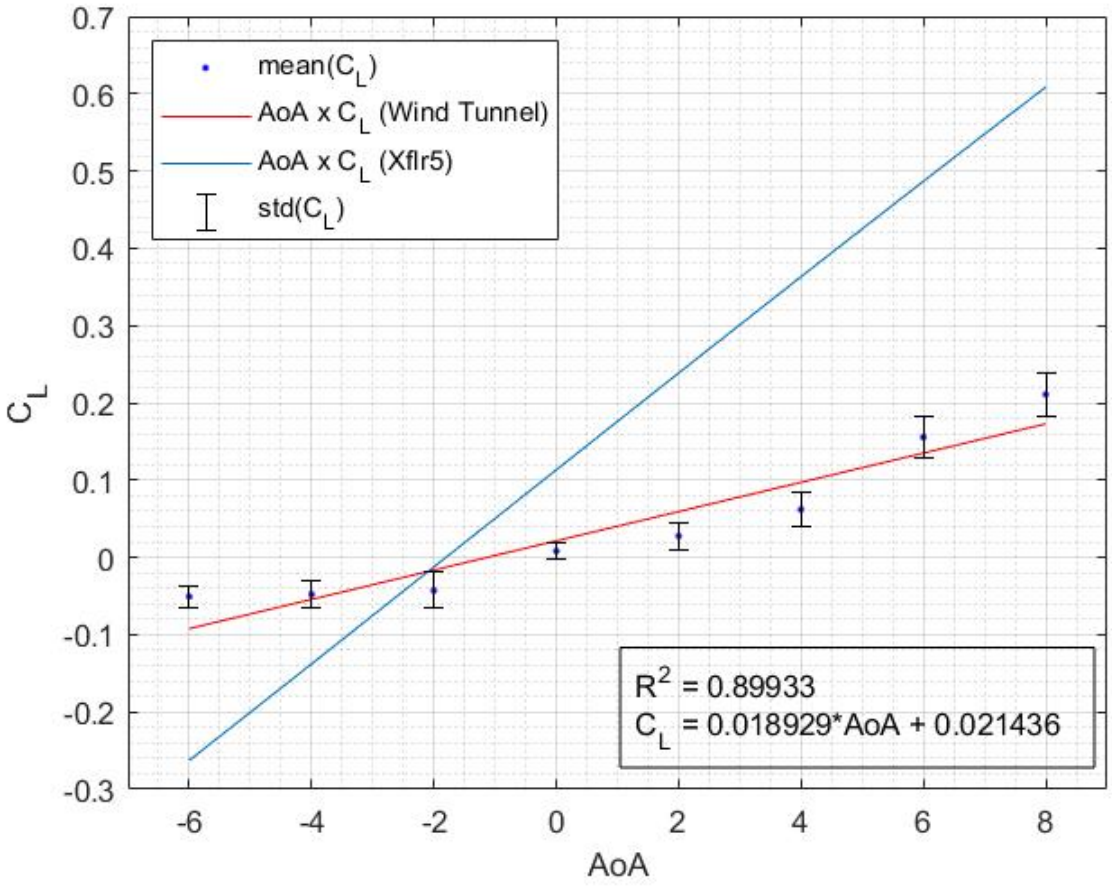

The experimental lift curve for the angle of attack range selected assumes a linear pattern, which is expected since this range is significantly lower than the stall angle. This is corroborated by the same pattern obtained via the ring vortex method. The slope of the experimental curve is much lesser than the one of the numerical result – possibly due to the induced drag which is not very well estimated by the latter. Other factors that may contribute to this discrepancy are enumerated in the following drag polar comparison.

Figure 4.5 – Drag polar comparison for the clean wing

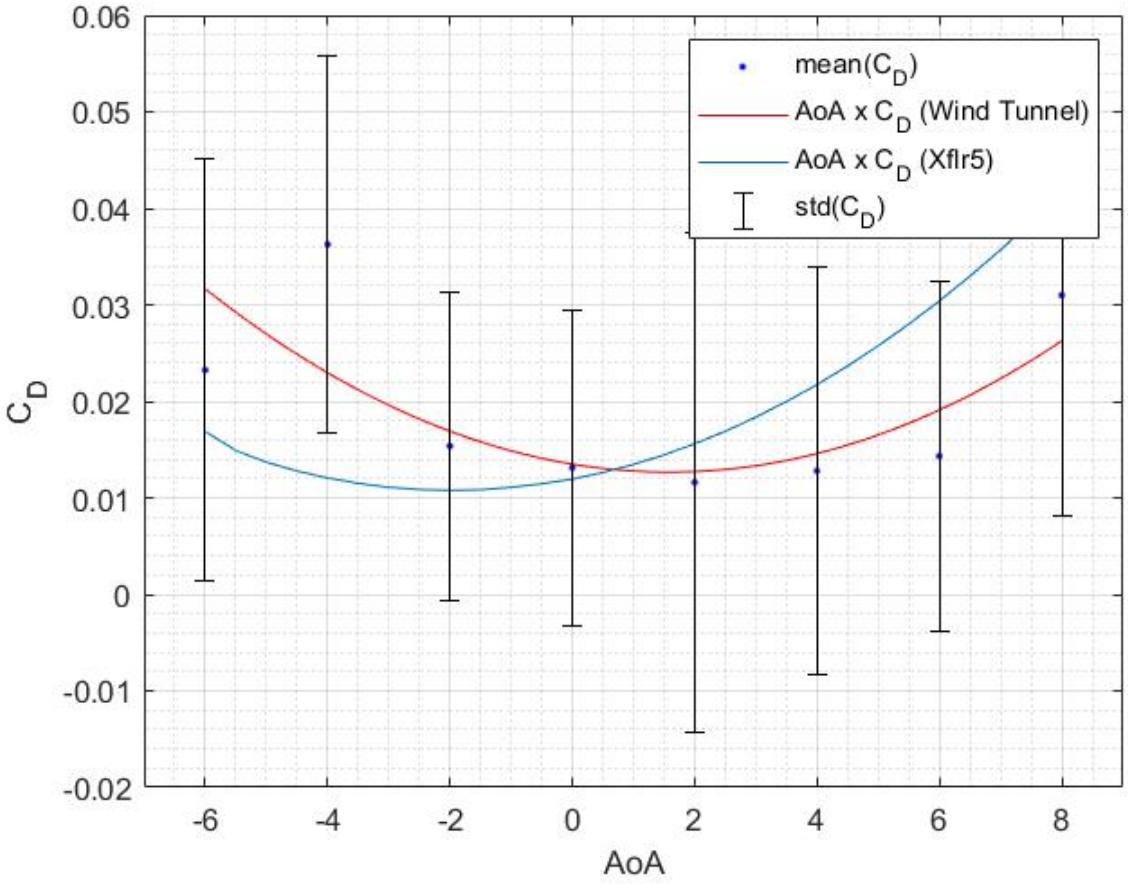

The experimental drag curve is considerably similar in shape to the numerical one, with the main difference between them being the value of the zero-lift drag coefficient (C_{D_0}), which is bigger for the experimental polar. This is justified by multiple reasons related to the numerical simulation, such as: the wing surface is perfect; there are no gaps, nor steps, between the components; the wing fairing was not employed; there are no walls apart from the surface of the wing, preventing interference from its boundary layer on the boundary layer on the wing surface. It is worth mentioning that the standard deviation of the experimental polar is significantly high due to the proximity of the drag forces to the resolution of the wind tunnel balance, reducing the fidelity of this curve. Other source errors were the blockage ratio of the full assembly (excluding the propellers) having reached 5.93%, which could impart an error in the drag coefficient assessment by over 10% (Takeda & Kato, 1992), and the surface rugosity of the printed model, which could have made the flow separation occur closer to the leading edge of the airfoil,

increasing the drag. Finally, as mentioned in Subsubsection 3.4.1, the flow near the root of the wing model was affected by the boundary layer on the table of the experiment, due to the fact that the wing fairing was not high enough to shun the occurrence of this phenomenon.

4.3 Wing and one propeller

This subsection presents the pressure distribution obtained for the configuration requiring the wing and one propeller, during **Analysis 4**, with the use of the pressure tap reader. The propeller was attached on location 1, for the angles of attack of 2° and 4°, and the results are displayed in Figure 4.6.

Figure 4.6 – Pressure distribution for wing + one propeller on location 1 and pressure differential measurements on location U1

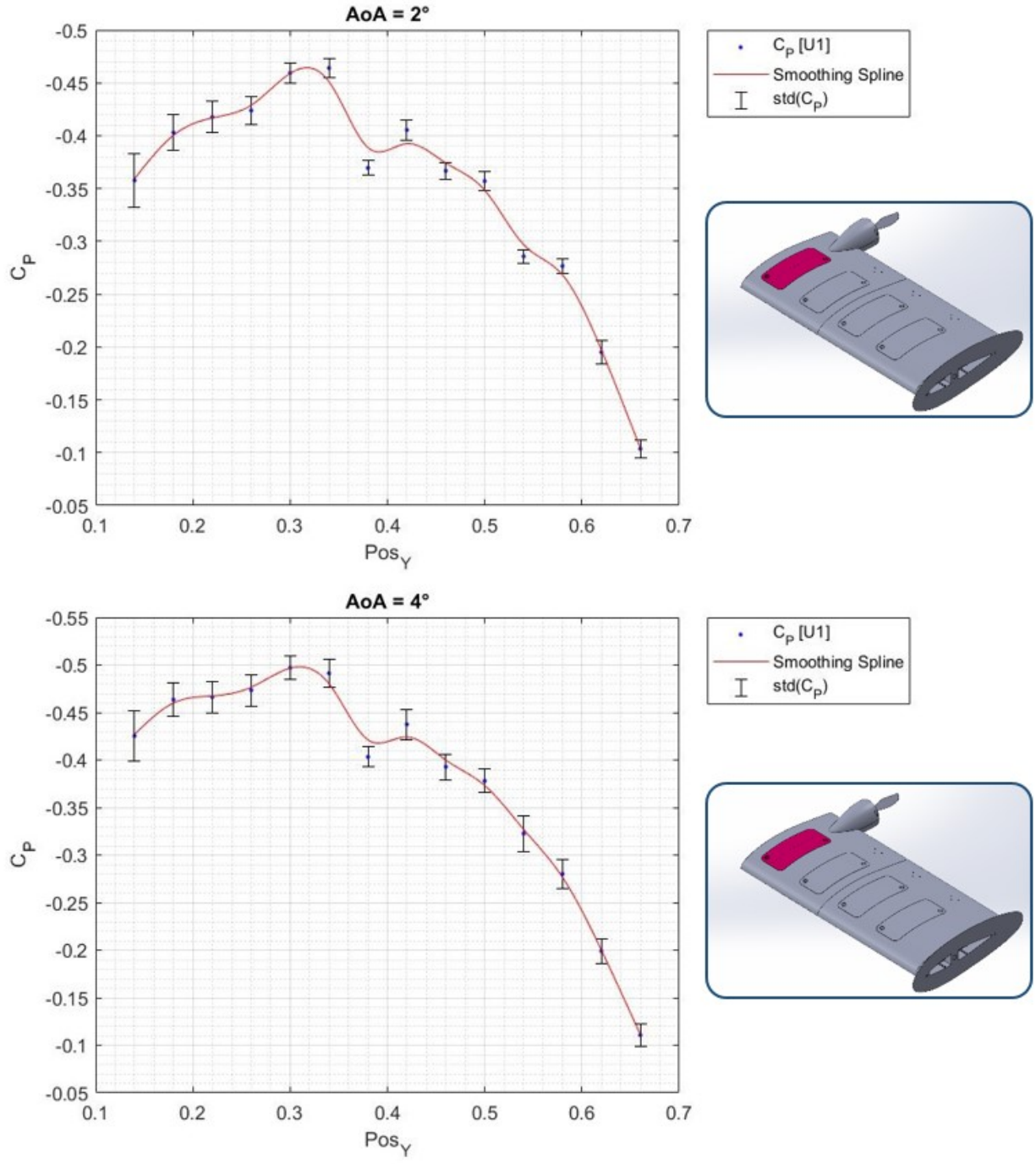

Considering the angle of attack of 2°, the pressure distribution on the upper surface is greater – in module – near the trailing edge of the wing ($^{x}/_{c} > 40\%$) for the mono-propeller configuration than for the clean wing configuration. This is due to the positioning of the propeller

near the trailing edge of the wing, known as the pusher configuration, which delays the transition of the boundary layer as well as the flow separation, increasing the lift force generated by the wing (CATALANO, 2004). Moreover, it is clear that this propeller positioning severely reduced the pressure coefficient plummet directly beyond 40% of the chord, when compared to that of the clean wing pressure coefficient distributions depicted in Figure 4.2 and Figure 4.3. Likewise, the same effect occurs for the angle of attack of 4°, in which case the resulted C_P distribution is even greater in module than for the former angle of attack. This was expected because the latter angle of attack is greater and both angles are small enough to be far from the stall region.

4.4 Wing and two propellers

This subsection shows the pressure distribution obtained for the configuration requiring the wing and two propellers, during **Analysis 5**, with the use of the pressure tap reader and the results are illustrated in Figure 4.7 and Figure 4.8. In sequence, the aerodynamic coefficients for this configuration are assessed, during **Analysis 6**, using the wind tunnel balance, and the resulting lift and drag polars are depicted in Figure 4.9 and Figure 4.10, respectively. In both **Analysis 5** and **6**, it is studied the influence of translating the second propeller from location 3 to location 4 (while the first propeller is kept on location 1), resulting in two sets of results for each analysis. The angle of attack of 4° was employed during **Analysis 5**, while the angles 2° and 4° were chosen for **Analysis 6**.

Figure 4.7 – Pressure distribution for wing + two propellers on location 1 + 3 and pressure differential measurements on location U1 + U3 (AoA = 4°)

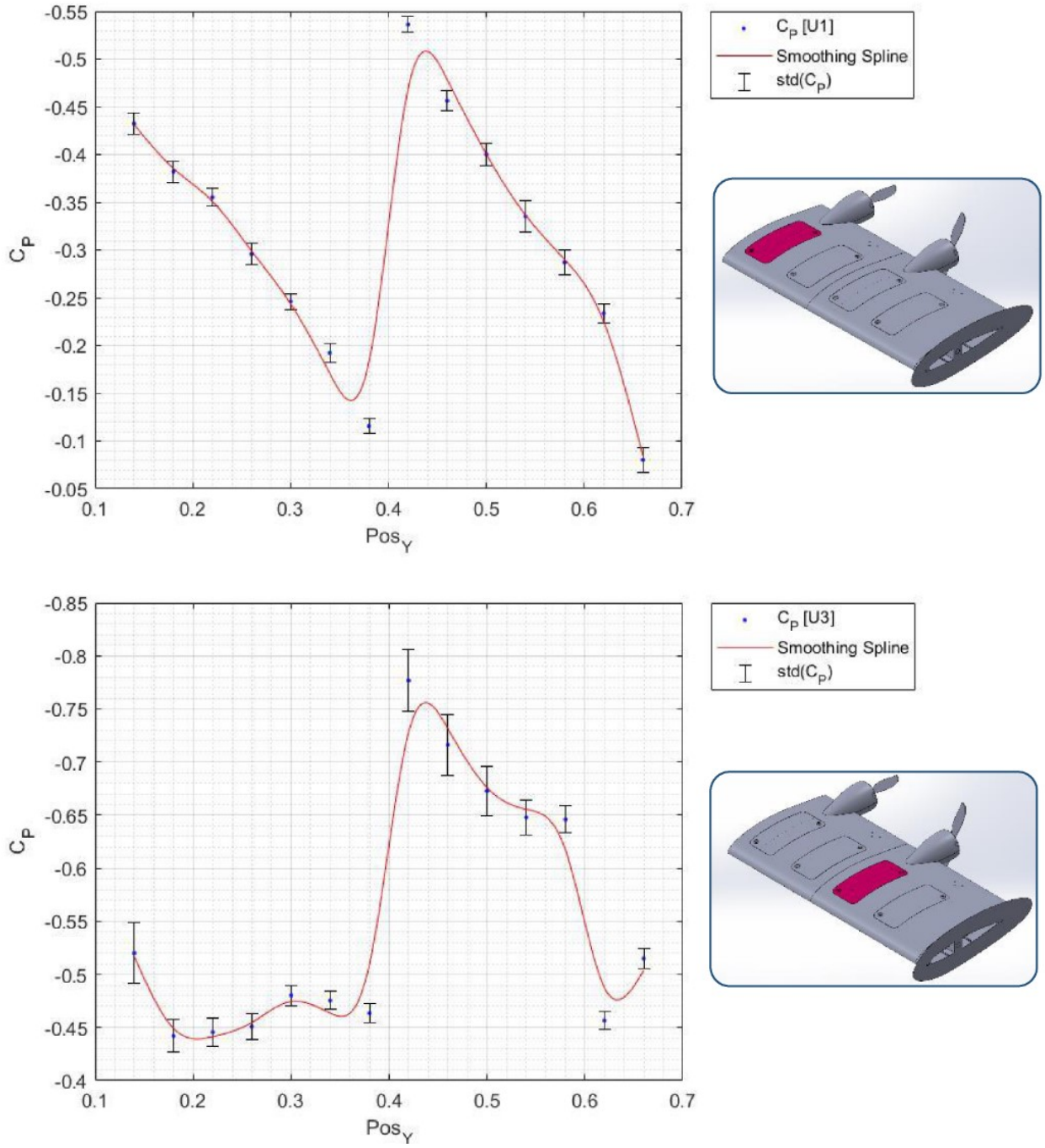

The pressure distribution on location U3 is greater – in module – than the one on location U1 for the configuration 1 + 3. This result was already expected since the lift distribution on the clean wing displayed in Figure 3.26 shows that the lift generated is greater towards the root of the

wing. Even though the computational result does not account for the addition of both propellers, it would be coherent to expect their influence not to change such general expectation for the lift distribution on the wing tip to be smaller, in module, than that on the root. Furthermore, this phenomenon can be explained by the induced drag, which is stronger near the tip of the wing (National Aeronautics and Space Administration, 1924).

Comparing the pressure distribution on location U1 for AoA = 4° with and without both propellers, it is clear that the propellers' influence in the flow strengthened the suction force on location U1 by increasing – in module – the pressure coefficient in the region closer to the trailing edge ($^{x}/_{c} > 40\%$). Again, this behavior was also foreseen due to the fact that the propellers were placed on the trailing edge of the wing, also known as pusher configuration. This effect was stronger, however, for the mono-propeller configuration than for the two-propeller one (still considering the pressure differential on U1), proving that not only does one propeller indeed affect the flow near the other propeller – in addition to their respective nearest region – but also that the distributed propulsion may not always provide an increase in the aerodynamic efficiency of the wing, contrary to what the literature would lead one to believe (de Vries et al., 2019).

The comparison between the pressure distribution on location U3 for AoA = 4° with and without the propellers, on the other hand, depicted an unexpected behavior: the pressure coefficient was significantly reduced – in module –, especially on the region closer to the leading edge ($^{x}/_{c} < 40\%$). This phenomenon is another reminder that the conjoint influence of the propellers on a specific region may hamper its local aerodynamic characteristics. Finally, for the region near the trailing edge ($^{x}/_{c} > 40\%$), the C_P was increased in module, as expected due to the pusher configuration.

Figure 4.8 – Pressure distribution for wing + two propellers on location 1 + 4 and pressure differential measurements on location U1 + U4 (AoA = 4°)

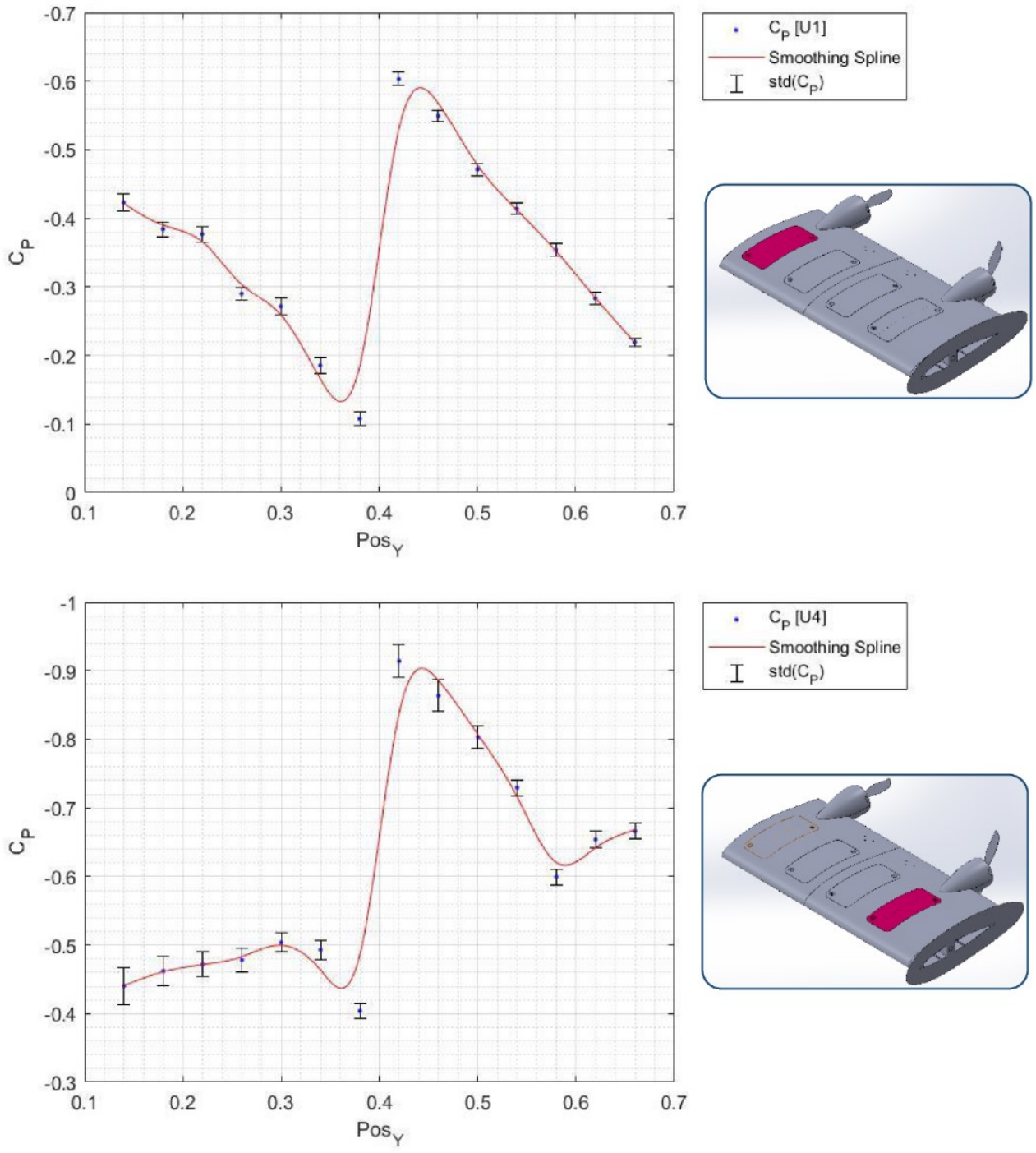

The pressure coefficient on the second half of location U1 also increased in module when the propellers were employed in configuration 1 + 4, compared to the previous configurations – clean wing, one propeller on 1 and two propellers on 1 + 3 –. This phenomenon can be attributed

to the propeller placed on location 4 ameliorating the induced drag by rotating inboard up, further corroborating the potential benefits of a distributed propulsion system. By moving the second propeller from location 3 to location 4, the pressure distribution is decreased, contrary to what was expected, since the location 4 is farther away from the wing tip than location 3 and, therefore, should provide a greater reduction over the induced drag. This might indicate that there is an optimal distance between the propellers in relation to the local aerodynamic coefficients for a specific wing region. Finally, the same behavior observed on location U3 in configuration 1 + 3 was spotted on location U4 in configuration 1 + 4.

Figure 4.9 – Lift polars for wing + two propellers on locations 1 + 3 and 1 + 4

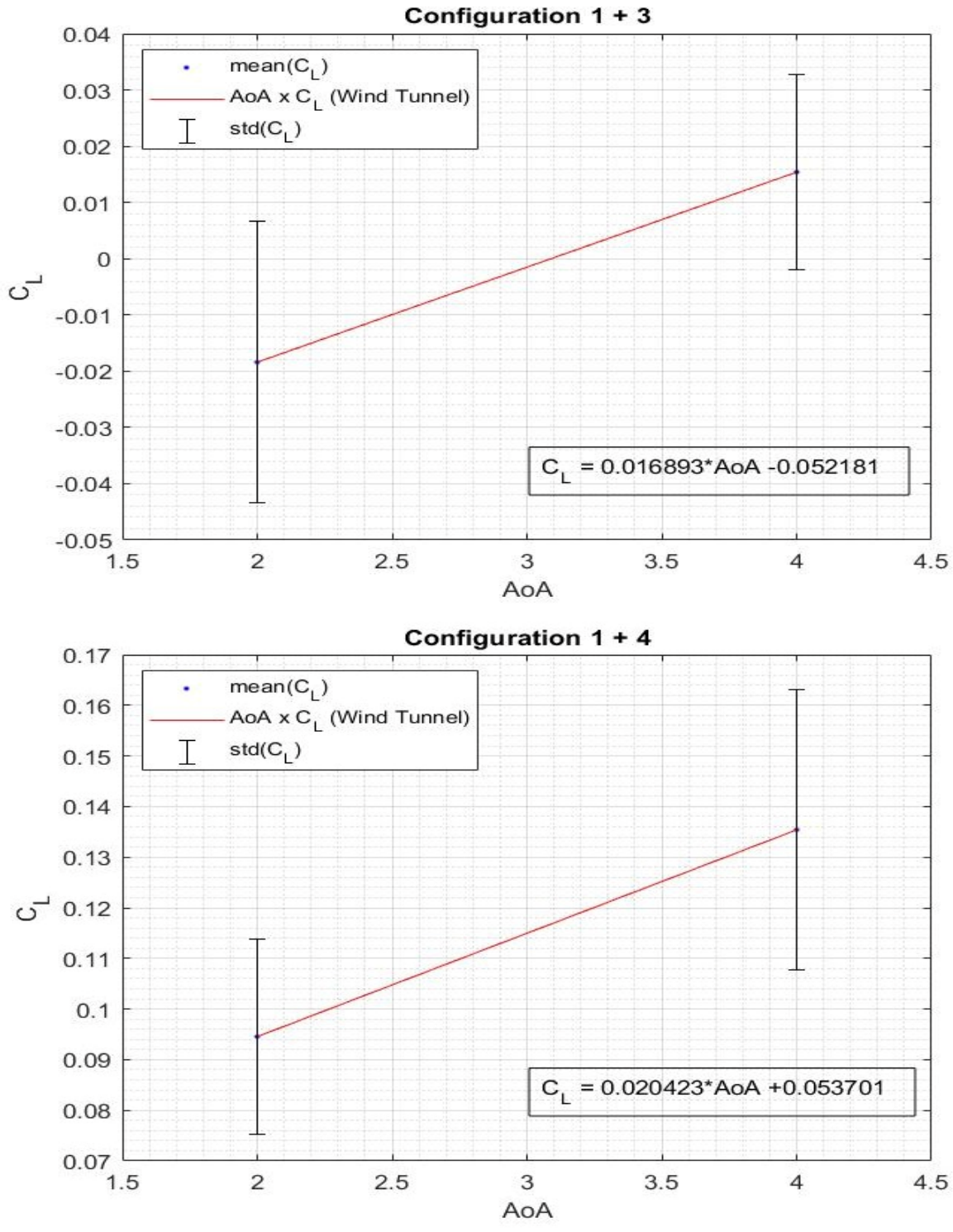

The lift coefficient of the wing for configuration 1 + 4 was greater than that of configuration 1 + 3, for both angles of attack. In addition, although the results may be tainted due to the reduced

scale of the printed model in comparison to the minimum sensibility of the wind tunnel balance, the relative lift increments can be analyzed in order to evaluate the influence of multiple configurations in the aerodynamic coefficients. In summation, the bigger the angle of attack and the farther apart that the propellers are to each other, the bigger the lift coefficient (always considering a range of angles of attack not encompassing nor past the stall region). Finally, the results suggest that the influence of the propeller's placement is far more relevant in the lift generation than the angle of attack: the increment in lift counts due to the increase in the angle of attack from 2° to 4° for configurations 1 + 3 and 1 + 4 is 3 and 4 counts, respectively, while the increment caused by the change in configuration from 1 + 3 to 1 + 4 for angles of attack 2° and 4° is 11 and 12 counts, respectively. This shows that the placement of the second propeller significantly alters the lift distribution over the wing as well as over the wing tip region (where the lift generation is minimal, as depicted in Figure 3.26, considering a typical rectangular wing), on which the other propeller is placed, while the increase in the angle of attack promotes a lesser lift distribution increment across the entire wingspan.

Figure 4.10 – Drag polars for wing + two propellers on locations 1 + 3 and 1 + 4

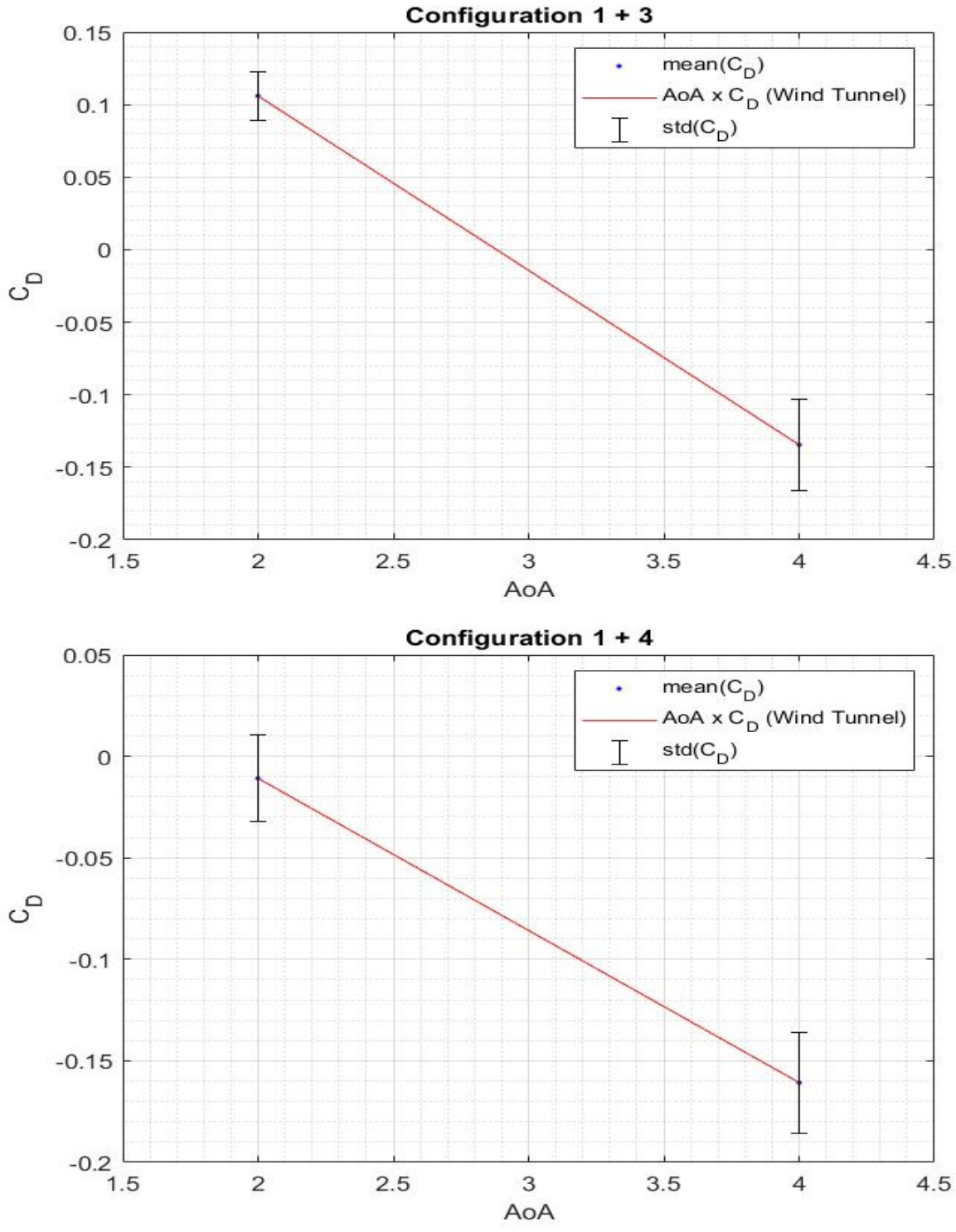

The drag coefficient for configuration 1 + 4 was lesser than that of configuration 1 + 3, which was not expected, considering that the placement of the second propeller from location 3 to

location 4 should reduce its ameliorating effect over the induced drag, provided that location 4 is farther away from the wing tip than location 3. Additionally, as previously stated for the lift polars, even though the result most likely is impaired by the reduced scale of the printed model in relation to the minimum sensibility of the wind tunnel balance, the relative drag increments can be employed in the analyses of the aerodynamic coefficients for different wing-propeller configurations. Unlike the lift polars, the influence of the angle of attack was more pronounced than that of the closeness of the propeller to the wing tip: the increment in drag counts caused by the increase in the angle of attack from 2° to 4° for configurations 1 + 3 and 1 + 4 is 2405 and 1499 counts, respectively, while the increment attributable to the change in configuration from 1 + 3 to 1 + 4 for angles of attack 2° and 4° is 1169 and 262 counts, respectively.

5 Conclusions

Distributed propulsion is frequently discussed lately due to its supposed gains in performance over more traditional configurations, such as the twin turboprop and the turbojet, which include fuel burn and noise reductions as well as an increase in lift generation. One of the most noticeable configurations under the distributed propulsion model is the distributed electric propulsion, DEP, which could be instrumental in achieving a flight operation without the use of fossil fuels.

As with any aircraft configuration model, distributed propulsion can be implemented in a huge variety of ways: the number and diameter of the propellers as well as the spacing between them can all vary greatly – significantly affecting the aerodynamic effects for each personalized configuration. In order to analyze the basal influence of the distributed propulsion, two propellers were employed in this work, along with experiments using one propeller and clean wing only. The second propeller's location was placed in two different spanwise locations, in order to account for the effects of the propeller spacing and distribution in a distributed propulsion system over the aerodynamic coefficients. Throughout the experiments, it was used a wind tunnel, a pressure tap reader and a wind tunnel balance.

In addition to the relevance of further research on distributed propulsion nowadays, it was also opted to adopt the pusher configuration, since very few studies regarding both configurations at the same time were made available to the public. Three main configurations were selected: the wing without propeller, the wing with one propeller and, finally, the wing with two propellers. The analyses of those configurations allowed to better understand the influence of the distributed propulsion – in pusher configuration – on the aerodynamic coefficients of the wing, assessing the optimal placement of the second propeller spanwise in order to obtain the best aerodynamic efficiency.

The results show that the drag coefficient for all test cases employing two propellers was always lesser than the one measured for the wing without propeller. Additionally, the lift coefficient for the two-propeller configuration for the test case where the second propeller is closest to the wing root was always bigger than the one obtained for the wing without propeller. These results suggest that distributed propulsion can indeed boost the aerodynamic efficiency of the wing, and that such gains are strongly dependent on the spanwise distribution of the propellers.

On the other hand, it was also noticed that the potential benefits of the distributed propulsion are not as easily attained as one would be led to believe by the current literature on the subject.

In addition, the pressure coefficient distribution results corroborate that the flow separation is delayed in the pusher configuration, which could be assessed from the greatest values towards the trailing edge of the wing – in module – being in the configuration with two propellers, with the second propeller being placed closest to the wing root. The second best pressure distribution occurs in the configuration where the second propeller is closest to the tip of the wing, followed by the single propeller configuration and, lastly, the wing without propeller. The pressure results are also a testament to the dependence of the spanwise distribution of the propellers to the aerodynamic efficiency of the wing.

A relevant remark concerning the distributed propulsion configuration was noticed: the influence of the propeller's spanwise distribution is far more relevant than the influence of the angle of attack on the lift coefficient of the wing, while the opposite phenomenon was detected for the wing's drag coefficient. Further analyses may be required in order to better understand said phenomena.

In order to analyze the distributed propulsion effects on a wing, this work required the following general steps: design and manufacturing of a wing with enclosures as well as nacelles, instrumentation of a wind tunnel, operation of two propellers simultaneously, experimental setup, operation of a wind tunnel as well as additional devices and, finally, post processing of all resulting data regarding multiple wing-propeller configurations.

Considering the resolution issues of the wind tunnel balance, a continuation of this work could employ CFD to measure the aerodynamic coefficients for the configurations studied, so that to compare the results with the ones contained in this present work. Those simulations could also further explore the influence on the propellers' spanwise distribution, as well as implement more propellers – enabling a more profound understanding over the distributed propulsion configuration. It would also be relevant to redo the lost analyses concerning the placement of the single-engine configuration, as a way of further assessing its influence on the overall flow behavior around the wing as well as on the pressure distribution profiles on various sections across it.

References

ANDERSON Jr., J. D. *Introduction to Flight.* 8th ed. New York: McGraw Hill, 2016.

ALMEIDA, O.; Pinto, W.; Rosa, S. *Experimental Analysis of the Flow Over a Commercial Vehicle-Pickup, International Review of Mechanical Engineering (IREME),* 11 (8), pp. 530-537; 2017.

ALVES, R. M.; Almeida, O. *Validation of Experimental and Numerical Techniques for Flow Analysis over an Ahmed Body.* International Journal of Engineering Research and Applications, 7, 63-71; 2017.

BORER, N. K.; Moore, M. D.; Turnbull, A. R. *Tradespace Exploration of Distributed Propulsors for Advanced On-Demand Mobility Concepts.* 14th Aerospace Technology, Integrations, and Operations Conference, 2014.

CATALANO, F. M. *On the Effects of an Installed Propeller Slipstream on Wing Aerodynamic Characteristics.* Acta Polytechnica, 2004.

DEPERROIS, A. (2019). *Theoretical limitations and shortcomings of xflr5.* Xflr5 Tech.

DE VRIES, R; Hoogreef, M. F. M.; Vos, R. *Preliminary Sizing of a Hybrid-Electric Passenger Aircraft Featuring Over-the-Wing Distributed-Propulsion*. AIAA SciTech Forum. Delft University of Technology, 2019.

GRIFFITH, A. A. *Improvements Relating to Aircraft and Aircraft Engine Installations. United Kingdom Patent, 720,394; 1954.*

INTERNATIONAL CIVIL AVIATION ORGANIZATION. *Tracking of Aviation Emissions & Fuel Efficiency Improvements/Market Based Measures.* ICAO Workshop on State Action Plans on CO_2 Reduction Activities. 14th Aerospace Technology, Integrations, and Operations Conference, 2014. Available in: < https://www.icao.int/NACC/Documents/Meetings/2014/ENVSEMINAR/8.2.IATA%20MBM.pdf>. Access in November 13th, 2022.

KELLER, D. *Towards Higher Efficiency of Propeller-Driven Aircraft with Distributed Propulsion.* CEAS Aeronaut J 12, 777-791; 2021.

KHAJEHZADEH, A. *Analysis of an Over the Wing Based Distributed Propulsion System.* 2018. 179 p. Master of Science Thesis, Delft University of Technology, Delft.

MANZEL, C. W. *Propelling Mechanism for Airships and the Like.* Serial no. 321,008, United States Patent Office, 1,489,872; 1924.

MARCUS, E. A. P.; de Vries, R; Raju Kulkarni, A; Veldhuis, L. L. M. *Aerodynamic Investigation of an Over-the-Wing Propeller for Distributed Propulsion.* AIAA Aerospace Sciences Meeting. Delft University of Technology, 2018.

MARCUS, E. A. P. *Aerodynamic Modelling and Performance Analysis of Over-The-Wing Propellers.* 2018. 123 p. Master of Science Thesis, Delft University of Technology, Delft.

MOORE, M. D.; Fredericks, B. *Misconceptions of Electric Propulsion Aircraft and their Emergent Aviation Markets.* 52nd Aerospace Sciences Meeting. NASA Langley Research Center, 2014.

MOORE, M. D.; Goodrich, K.; Viken, J.; Smith, J.; Fredericks, B. *High-Speed Mobility through On-Demand Aviation.* Aviation Technology, Integration, and Operations Conference, 2013.

NATIONAL AERONAUTICS AND SPACE ADMINISTRATION. 1924. *Induced Drag of Multiplanes* (Prandtl, L.). Available in: <https://ntrs.nasa.gov/api/citations/19930080964/downloads/19930080964.pdf>. Access in September 13th, 2022.

NISHIOKA, A. H.; Almeida, O. *Study, Design and Test of a LENZ-Type Wind Turbine.* International Journal of Advanced Engineering Research and Science, 5(3), 264-269; 2018.

OREFICE, F.; Nicolosi, F.; Della Vecchia, P.; Ciliberti, D. *Conceptual Design of Commuter Aircraft including Distributed Electric Propulsion*. AIAA AVIATION Forum. University of Naples “Federico II”, Naples, 2020.

PAN, T. *Aerodynamic Analysis for Hybrid Electric Distributed Propulsion Aircraft.* 2020. 201 p. PhD thesis, The University of Leeds, Leeds.

PATTERSON, M. D.; Borer, N. K.; German, B. J. *A Simple Method for High-Lift Propeller Conceptual Design.* 54th Aerospace Sciences Meeting. NASA Langley Research Center, 2016.

PINTO, W. J. G. D. S. *Numerical and Experimental Analysis of the Flow over a Commercial Vehicle-Pickup.* Thermal Engineering, 17(2), 92-102; 2018.

SCHMOLLGRUBER, P; Döll, C.; Hermetz, J.; Liaboeuf, R.; Ridel, M.; Cafarelli, I. … Paluch, B. *Multidisciplinary Exploration of DRAGON: an ONERA Hybrid Electric Distributed Propulsion Concept*. AIAA SciTech Forum. ONERA, Palaiseau, 2019.

SGUEGLIA, A. *Methodology for Sizing and Optimizing a Blended Body with Distributed Electric Ducted Fans.* 2019. 312 p. Doctoral Thesis, Institut Supérieur de l'Aéronautique et de l'Espace, Toulouse.

SILVA FILHO, R. R. *Análise Numérica das Características Aerodinâmicas de uma Asa de Baixo Alongamento com Propulsão Distribuída.* 2020. 150 p. Master's thesis, Universidade Federal de Minas Gerais, Belo Horizonte.

SILVEIRA, J. P. *An Experimental Study of the Aerodynamic Characteristics of an Aircraft Model with Canard-Wing Configuration.* 2017. 77 p. Bachelor's thesis, Universidade Federal de Uberlândia, Uberlândia.

STOLL, A. M. *Comparison of CFD and Experimental Results of the LEAPTech Distributed Electric Propulsion Blown Wing*. 15th AIAA Aviation Technology, Integration, and Operations Conference. Joby Aviation, 2015.

TAKEDA, K.; Kato, M. *Wind Tunnel Blockage Effects on Drag Coefficient and Wind-Induced Vibration*. Journal of Wind Engineering and Industrial Aerodynamics, 1992.

Appendix

Appendix A – C_P Distribution code

This appendix section showcases the code designed in software MatLab to plot the C_P distribution over locations U1 and L1 for the clean wing. For the sake of conciseness, some pages were edited out.

```
clear
clc
close all

Pressure_Upper_Surface_1  = [-80    -80 -76 -76 -74 -68 -68
-74 -74 -73 -73 -78 -78 -82 -82 -74 -86 -86 -81 -75 -75 -76
-71 -71 -76 -76 -79 -75 -76 -76 -76 -76 -72 -75 -75 -70 -74
-74 -84 -84 -88 -84 -84 -77 -77 -72 -72 -74 -74 -72 -72 -67
-72 -72 -77 -74 -74 -76 -71 -71 -69 -69 -77 -81 -75 -75 -73
-73 -78 -78 -76 -70 -74 -74 -72 -71 -71 -70 -70 -69 -69 -71
-71 -68 -68 -68 -76 -76 -81 -81 -76 -81 -75 -75 -80 -80 -81
-82 -82 -79 -75 -75 -70 -71 -71 -74 -74 -67 -72 -72 -76 -83
-83 -85 -85 -79 -79 -71 -71 -73 -73 -78 -78 -73 -73 -72 -72
-71 -71 -73 -73 -81 -81 -69 -75 -77 -77 -74 -74 -79 -77 -77
-74 -74 -78 -78 -73 -73 -69 -69 -72 -68 -68 -71 -74 -74 -71
-71 -70 -73 -73 -75 -72 -72 -69 -78 -78 -88 -88 -72 -72 -74
-74 -72 -72 -75 -75 -81 -76 -76 -74 -75 -75 -72 -76 -76 -76
-76 -76 -76 -76 -76 -75 -75 -74 -74 -74 -72 -71 -71 -81 -73
-73 -73 -73 -73 -73 -75 -75 -74 -74 -78 -78 -75 -73 -73 -75
-69 -69 -71 -74 -74 -74 -74 -75 -74 -74 -74 -80 -80 -75 -75
-73 -73 -80 -80 -78 -72 -72 -75 -75 -76 -76 -78 -78 -78 -78
-79 -79 -75 -72 -72 -77 -71 -71 -79 -77 -77 -72 -72 -70 -71
-72 -72 -72 -72 -73 -79 -79 -68 -79 -79 -75 -70 -70 -75 -75
-75 -75 -66 -66 -68 -68 -70 -77 -77 -78 -78 -83 -73 -77 -77
-80 -80 -74 -74 -75 -72 -74 -74 -71 -73 -73 -72 -72 -75 -75
-69 -69 -68 -68 -76 -76 -81 -83 -82 -82 -68 -68 -79 -73 -73
-78 -78 -67 -68 -68 -75 -80 -80 -71 -71 -73 -75 -75 -73 -70
-70 -72 -72 -79 -79 -80 -80 -74 -74 -70 -70 -75 -74 -74 -77
-71 -71 -73 -73 -74 -74 -74 -72 -80 -80 -74 -76 -76 -77 -77
-79 -79 -80 -80 -81 -81 -75 -75 -77 -77 -77 -82 -79 -79 -78
-78 -73 -85 -85 -80 -76 -76 -79 -79 -76 -74 -74 -81 -81 -74
-81 -81 -83 -77 -77 -78 -78 -71 -76 -79 -79 -75 -75 -70 -70
-70 -75 -71 -71 -76 -76 -73 -68 -68 -75 -75 -86 -86 -75 -75
-80 -80 -80 -80 -78 -77 -76 -76 -75 -75 -83 -76 -76 -70 -72
```

```
-72 -71 -71 -71 -74 -74 -73 -73 -76 -78 -76 -76 -78 -78 -77
-77 -74 -74 -74 -74 -72 -72 -66 -66 -69 -69 -77 -77 -75 -75
-26 -24 -21 -21 -24 -24 -23 -23 -24 -25 -25 -24 -24 -24 -26
-26 -25 -25 -24 -24 -24 -26 -26 -26 -26 -25 -25 -25 -24 -24
-25 -25 -25 -25 -25 -24 -24 -26 -25 -25 -25 -25 -25 ];

rho = 1.1597;
V_inf = 18;
q_inf = 0.5*rho*(V_inf^2);

CP_Upper_Surface_1 = Pressure_Upper_Surface_1/q_inf;
CP_Upper_Surface_2 = Pressure_Upper_Surface_2/q_inf;
CP_Upper_Surface_3 = Pressure_Upper_Surface_3/q_inf;
CP_Upper_Surface_4 = Pressure_Upper_Surface_4/q_inf;
CP_Upper_Surface_5 = Pressure_Upper_Surface_5/q_inf;
CP_Upper_Surface_6 = Pressure_Upper_Surface_6/q_inf;
CP_Upper_Surface_7 = Pressure_Upper_Surface_7/q_inf;
CP_Upper_Surface_8 = Pressure_Upper_Surface_8/q_inf;
CP_Upper_Surface_9 = Pressure_Upper_Surface_9/q_inf;
CP_Upper_Surface_10 = Pressure_Upper_Surface_10/q_inf;
CP_Upper_Surface_11 = Pressure_Upper_Surface_11/q_inf;
CP_Upper_Surface_12 = Pressure_Upper_Surface_12/q_inf;
CP_Upper_Surface_13 = Pressure_Upper_Surface_13/q_inf;
CP_Upper_Surface_14 = Pressure_Upper_Surface_14/q_inf;


CP_Lower_Surface_1  = Pressure_Lower_Surface_1/q_inf;
CP_Lower_Surface_2  = Pressure_Lower_Surface_2/q_inf;
CP_Lower_Surface_3  = Pressure_Lower_Surface_3/q_inf;
CP_Lower_Surface_4  = Pressure_Lower_Surface_4/q_inf;
CP_Lower_Surface_5  = Pressure_Lower_Surface_5/q_inf;
CP_Lower_Surface_6  = Pressure_Lower_Surface_6/q_inf;
CP_Lower_Surface_7  = Pressure_Lower_Surface_7/q_inf;
CP_Lower_Surface_8  = Pressure_Lower_Surface_8/q_inf;
CP_Lower_Surface_9  = Pressure_Lower_Surface_9/q_inf;
CP_Lower_Surface_10 = Pressure_Lower_Surface_10/q_inf;
CP_Lower_Surface_11 = Pressure_Lower_Surface_11/q_inf;
CP_Lower_Surface_12 = Pressure_Lower_Surface_12/q_inf;
CP_Lower_Surface_13 = Pressure_Lower_Surface_13/q_inf;
CP_Lower_Surface_14 = Pressure_Lower_Surface_14/q_inf;

std_CP_Upper_Surface = [std(CP_Upper_Surface_1)
std(CP_Upper_Surface_2) std(CP_Upper_Surface_3)
std(CP_Upper_Surface_4) std(CP_Upper_Surface_5)
```

```
std(CP_Upper_Surface_6) std(CP_Upper_Surface_7)
std(CP_Upper_Surface_8) std(CP_Upper_Surface_9)
std(CP_Upper_Surface_10) std(CP_Upper_Surface_11)
std(CP_Upper_Surface_12) std(CP_Upper_Surface_13)
std(CP_Upper_Surface_14)];

std_CP_Lower_Surface = [std(CP_Lower_Surface_1)
std(CP_Lower_Surface_2) std(CP_Lower_Surface_3)
std(CP_Lower_Surface_4) std(CP_Lower_Surface_5)
std(CP_Lower_Surface_6) std(CP_Lower_Surface_7)
std(CP_Lower_Surface_8) std(CP_Lower_Surface_9)
std(CP_Lower_Surface_10) std(CP_Lower_Surface_11)
std(CP_Lower_Surface_12) std(CP_Lower_Surface_13)
std(CP_Lower_Surface_14)];

Pos_Y = [0.1416 0.1816  0.2216  0.2616  0.3016  0.3416
0.3816  0.4216  0.4616  0.5016  0.5416  0.5816  0.6216
0.6616];

CP_Upper_Surface = [mean(CP_Upper_Surface_1)
mean(CP_Upper_Surface_2) mean(CP_Upper_Surface_3)
mean(CP_Upper_Surface_4) mean(CP_Upper_Surface_5)
mean(CP_Upper_Surface_6) mean(CP_Upper_Surface_7)
mean(CP_Upper_Surface_8) mean(CP_Upper_Surface_9)
mean(CP_Upper_Surface_10) mean(CP_Upper_Surface_11)
mean(CP_Upper_Surface_12) mean(CP_Upper_Surface_13)
mean(CP_Upper_Surface_14)];

CP_Lower_Surface = [mean(CP_Lower_Surface_1)
mean(CP_Lower_Surface_2) mean(CP_Lower_Surface_3)
mean(CP_Lower_Surface_4) mean(CP_Lower_Surface_5)
mean(CP_Lower_Surface_6) mean(CP_Lower_Surface_7)
mean(CP_Lower_Surface_8) mean(CP_Lower_Surface_9)
mean(CP_Lower_Surface_10) mean(CP_Lower_Surface_11)
mean(CP_Lower_Surface_12) mean(CP_Lower_Surface_13)
mean(CP_Lower_Surface_14)];

X1 = Pos_Y;
Y1 = CP_Upper_Surface;
Y2 = CP_Lower_Surface;
D1 = std_CP_Upper_Surface;

%% Fit: 'untitled fit 1'.
```

```
[xData, yData] = prepareCurveData( Pos_Y, CP_Upper_Surface
);

% Set up fittype and options.
ft = fittype( 'smoothingspline' );
opts = fitoptions( 'Method', 'SmoothingSpline' );
opts.SmoothingParam = 0.9999973839752613;

% Fit model to data.
[fitresult, gof] = fit( xData, yData, ft, opts);

% Plot fit with data.
figure( 'Name', 'untitled fit 1' );
h1 = plot( fitresult, xData, yData);
% Label axes
xlabel Pos_Y
ylabel CP
grid on
hold on

% Create errorbar
errorbar1 =
errorbar(X1,Y1,D1,'DisplayName','std(C_P)','LineStyle','non
e','Color',[0 0.447 0.741]);

% Get xdata from plot
xdata1 = get(errorbar1, 'xdata');
% Get ydata from plot
ydata1 = get(errorbar1, 'ydata');
% Make sure data are column vectors
xdata1 = xdata1(:);
ydata1 = ydata1(:);

[xData, yData] = prepareCurveData( Pos_Y, CP_Lower_Surface
);

% Set up fittype and options.
ft = fittype( 'smoothingspline' );
opts = fitoptions( 'Method', 'SmoothingSpline' );
opts.SmoothingParam = 0.9999973839752613;

% Fit model to data.
[fitresult, gof] = fit( xData, yData, ft, opts);
```

```
% Plot fit with data.
h2 = plot( fitresult, xData, yData);
hold on

set(gcf, 'unit', 'inches');
% get the original size of figure before the legends are
added
figure_size =  get(gcf, 'position')
% add legends and get its handle
h_legend = legend([h1; h2], 'C_P [U1]', 'x/c x C_P [U1]',
'C_P [L1]', 'x/c x C_P [L1]', 'Total', 'Location',
'NorthEast Outside')
set(h_legend, 'location', 'northeastoutside')
% set unit for legend size to inches
set(h_legend, 'unit', 'inches')
% get legend size
legend_size = get(h_legend, 'position')
% new figure width
figure_size(3) = figure_size(3) + legend_size(3)
% set new figure size
set(gcf, 'position', figure_size)


set([h2],'color','g')
grid minor

% Create errorbar
errorbar2 =
errorbar(X1,Y2,D1,'DisplayName','std(C_P)','LineStyle','non
e','Color',[0 0.447 0.741]);

% Get xdata from plot
xdata1 = get(errorbar2, 'xdata');
% Get ydata from plot
ydata1 = get(errorbar2, 'ydata');
% Make sure data are column vectors
xdata1 = xdata1(:);
ydata1 = ydata1(:);

set(gca, 'YDir','reverse')

xlabel('x/c')
ylabel('C_P')
```

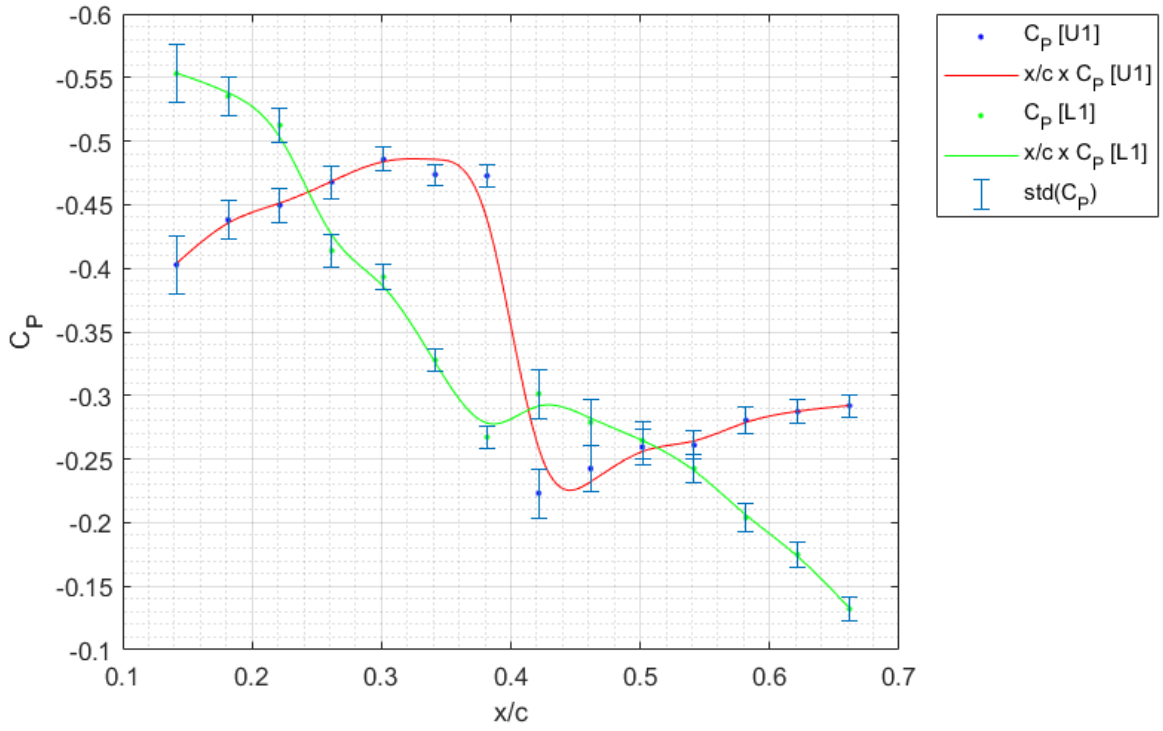
-0.6
-0.55
-0.5
-0.45
-0.4
-0.35
-0.3
-0.25
-0.2
-0.15
-0.1
C_P
0.1
0.2
0.3
0.4
0.5
0.6
0.7
x/c
C_P [U1]
x/c x C_P [U1]
C_P [L1]
x/c x C_P [L1]
std(C_P)

Appendix B – C_L Polar code

This appendix section showcases the code designed in software MatLab to plot the lift polar for the clean wing. For the sake of conciseness, some pages were edited out.

```
function [fitresult, gof] = createFit(AoA, CL)
clear
close all
clc

Lift_0deg  = [0.5   0.5 0.5 0.5 0.5 0.5 0.5 0.5 0.5 0.5 0.5
0.5 0   0   0   0   0   0   0   0   1.4 1.4 1.4 1.4 1.4 1.4
0   0   0   0   0   0   0   0   0   0   0   0   0   0
0   0   1.4 1.4 1.4 1.4 1.9 1.9 0.5 0.5 0.5 0.5 0.5 0.5 0.5
0.5 0.5 0.5 0.5 0.5 0.5 0.5 0.5 0.5 0   0   0   0   0   0
0   0   0   0   0   0   0   0   0   0   0   0   0   0   0
0   0   0   0   0   0   0   0   0   0   0   0   0   0   0
0   0   0   0   0   0   0   0   0   0   0   0   0   0   0
0   0   0.5 0.5 0.5 0.5 0   -0.5    -0.5    -0.5    -0.5
-0.5    -0.5    0   0   0   0   0   0   0.5 0.5 0.5 0.5 0.5
0.5 0   0   0   0   0   0   0.5 0.5 0.5 0.5 0.5 0.5 0.5 0.5
0.5 0.5 0.5 0.5 0.5 1.9 1.9 1.9 1.9 1.9 1.4 0   0   0   0
0.5 0.5 0.5 0.5 0.5 0.5 0   0   0   0   0   0   0   0   0
0   0   0   0   0   0   0   0   0   0.5 0.5 0.5 0.5 0.5 0.5
0.5 0.5 0.5 0.5 0.5 0.5 0.5 0.5 0.5 0.5 0.5 0   0   0   0
0   0   0.5 0.5 0.5 0.5 1.4 1.4 0.9 0.9 0.9 0.9 0   -0.5
0   0   0   0   0   0.5 0   0   0   0   0   0   0   0   0
0   0   0   0.5 0.5 0.5 0.5 0.5 0.5 0.5 0.5 0.5 0.5 0.5 0
0   0   0   0   0   0.5 0.5 0.5 0.5 0.5 0.5 0   0   0   0
0   0   0   1.4 1.4 1.4 1.4 1.4 1.4 0   0   0   0   0   0
0   0   0   0   0   0   0   0   0   0   0.5 0.5 0.5 0.5 0.5
0.5 0.5 0.5 0.5 0.5 0.5 0.5 0.5 0.5 0.5 0.5 0.5 0.5 0.5 0.5
0.5 0.5 0.5 0.5 0   0   0   0   0   0.5 0.5 0.5 0.5 0.5 0.5
0.5 0.5 0.5 0.5 0.5 0.5 0.5 0.5 0.5 0.5 0.5 0.5 0.5 0.5 0.5
0.5 0.5 0.5 0.5 0.5 0.5 0.5 0.5 0.5 0.5 0.5 0.5 0.5 0.5 0.5
0   0   0   0   0   0   0   0   0   0   0.5 0.5 0.5 0.5 0.5
0.5 0.5 0.5 0.5 0.5 0.5 0.5 0.5 0.5 0.5 0.5 0.5 0.5 0.5 0.5
0.5 0.5 0.5 0.5 0.5 1   1   1   1   1.9 1.9 0.9 0.9 0.9 0.9
0   0   0   0   0   0   0   0.5 0.5 0.5 0.5 0.5 0.5 0.5 0.5
0.5 0.5 0.5 0.5 0   0   0   0   0   0   0.5 0.5 0.5 0.5 0.5
0.5 0.5 0.5 0.5 0.5 0.5 0.5 0.5 0.5 0.5 0.5 0.5 0.5 0.5 0.5
0.5 0.5 0.5 0.5 0   0   0   0   0   0.5 0.5 0.5 0.5 0.5 0.5
```

```
3.6    -2.7    -2.7    -2.7    -2.7    -2.7    -2.7    -2.7
-2.7    -2.2    -2.2    -2.2    -2.2    -2.2    -2.7    -
2.7    -2.7    -2.7    -2.7    -2.7    -2.7    -2.7    -2.7
-2.7    -2.7    -2.7    -2.2    -2.2    -2.2    -2.2    -
2.2    -2.2    -2.2    -2.2    -2.2    -2.2    -2.2    -2.2
-2.7    -2.7    -2.7    -2.7    -2.7    -2.7    -2.2    -
2.2    -2.2    -2.2    -2.2    -2.2    -2.2    -2.2    -2.2
-2.2    -3.1    -3.1    -3.1    -3.1    -3.1    -3.1    -
2.2    -1.7    -1.7    -1.7    -1.7    -1.7    -1.7    -1.7
-1.7    -1.7    -1.7    -1.7    -2.2    -2.7    -3.6    -
3.6    -3.6    -3.6    -3.1    -2.6    -1.7    -1.7    -1.7
-2.6    -2.6    -3.1    -3.1    -3.1    -3.1    -2.2    -
2.2    -2.2    -2.2    -2.2    -2.2    -3.1    -3.6    -2.7
-2.7    -2.7    -2.7    -2.2    -1.7    -2.6    -2.6    -
2.6    -2.6    -2.6    -2.6    -2.6    -2.6    -2.6    -2.6
-1.7    -2.2    -2.2    -2.2    -2.2    -3.1    -3.1    -
2.6    -2.6    -2.6    -2.6    -1.7    -1.7    -1.7    -1.7
-1.7    -1.7    -1.7    -1.7    -0.8    -0.8    -0.8    -
0.8    -0.8    -0.8    -1.7    -1.7    -1.7    -1.7    -2.6
-2.6    -2.6    -2.6    -2.6    -2.6    -1.7    -2.2    -
2.2    -2.2    -2.2    -2.2    -2.2    -1.7    -0.8    -0.8
-0.8    -0.8    -0.8    -1.3    -2.2    -2.2    -2.2    -
3.1    -3.6    -3.1    -3.1    -3.1    -3.1    -3.1    -2.6
-2.6    -2.6    -2.6    -2.6    -2.6    -3.1    -3.1    -
4.5    -4.5    -4.5    -3.6    -4.1    -4.1    -2.7    -2.7
-3.6    -3.6    -3.1    -2.2    -2.2    -2.2    -2.2    -
1.3    -1.8    -2.7    -2.7    -2.7    -2.7    -2.2    -1.7
-1.7    -1.7    -1.7    -2.6    -3.1    -3.6    -3.6    -
3.6    -3.6    -3.6    -3.1    -2.6    -2.6    -2.6    -2.6
-1.7    -2.2    -2.2    -2.2    -2.2    -2.2    -3.1    -
2.6    -2.6    -2.6    -2.6    -2.6    -2.6    -2.6    -2.6
-2.6    -2.6    -2.6    -1.7    -2.2    -2.2    -2.2    -
2.2    -2.2    -2.2    -1.7    -1.7    -1.7    -1.7    -1.7
-2.2    -2.2];

rho_0deg = 1.1713;
rho_2deg = 1.1713;
rho_4deg = 1.1707;
rho_6deg = 1.1747;
rho_8deg = 1.1792;
rho_minus2deg = 1.1713;
rho_minus4deg = 1.1713;
rho_minus6deg = 1.1713;
```

```
rho = (rho_0deg + rho_2deg + rho_4deg + rho_6deg + rho_8deg
+ rho_minus2deg + rho_minus4deg + rho_minus6deg)/8;

S_ref = 0.2405;
V_inf = 18;
q_inf = 0.5*rho*(V_inf^2);

CL_0deg = Lift_0deg/(q_inf*S_ref);
CL_2deg = Lift_2deg/(q_inf*S_ref);
CL_4deg = Lift_4deg/(q_inf*S_ref);
CL_6deg = Lift_6deg/(q_inf*S_ref);
CL_8deg = Lift_8deg/(q_inf*S_ref);
CL_minus2deg = Lift_minus2deg/(q_inf*S_ref);
CL_minus4deg = Lift_minus4deg/(q_inf*S_ref);
CL_minus6deg = Lift_minus6deg/(q_inf*S_ref);


std_CL = [std(CL_minus6deg) std(CL_minus4deg)
std(CL_minus2deg) std(CL_0deg) std(CL_2deg) std(CL_4deg)
std(CL_6deg) std(CL_8deg)];

AoA = [-6 -4 -2 0 2 4 6 8];

CL = [mean(CL_minus6deg) mean(CL_minus4deg)
mean(CL_minus2deg) mean(CL_0deg) mean(CL_2deg)
mean(CL_4deg) mean(CL_6deg) mean(CL_8deg)];


%% Fit: 'untitled fit 1'.
[xData, yData] = prepareCurveData( AoA, CL );
ft = fittype( 'poly1' );
[fitresult, gof] = fit( xData, yData, ft );

figure( 'Name', 'AoA x C_L' );
h = plot( fitresult, xData, yData);
legend( h, 'mean(C_L)', 'AoA x C_L (Wind Tunnel)',
'Location', 'NorthWest' );

% Label axes
xlabel AoA
ylabel C_L
grid on
grid minor
```

```
hold on

X3 = [-6 -5.5 -5 -4.5 -4 -3.5 -3 -2.5 -2 -1.5 -1 -0.5 0 0.5
1 1.5 2 2.5 3 3.5 4 4.5 5 5.5 6 6.5 7 7.5 8];
Y3 = [  -0.263371     -0.232065   -0.200706   -0.169299   -
0.137852   -0.106372   -0.074864   -0.043335   -0.011792
0.019758    0.051310    0.082855    0.114388    0.145902
0.177391    0.208847    0.240264    0.271636    0.302956
0.334218    0.365414    0.396540    0.427587    0.458550
0.489423    0.520199    0.550871    0.581435    0.611883];

plot(X3,Y3,'DisplayName','AoA x C_L (Xflr5)');

X1 = AoA;
Y1 = CL;
D1 = std_CL;

errorbar1 =
errorbar(X1,Y1,D1,'DisplayName','std(C_L)','LineStyle','non
e','Color',[0 0.447 0.741]);

str=['R^2 =',num2str(gof.rsquare),newline,...
'C_L = ',num2str(fitresult.p1),'AoA +
',num2str(fitresult.p2)]
annotation('textbox',[.52 .26 0
0],'string',str,'FitBoxToText','on')
```

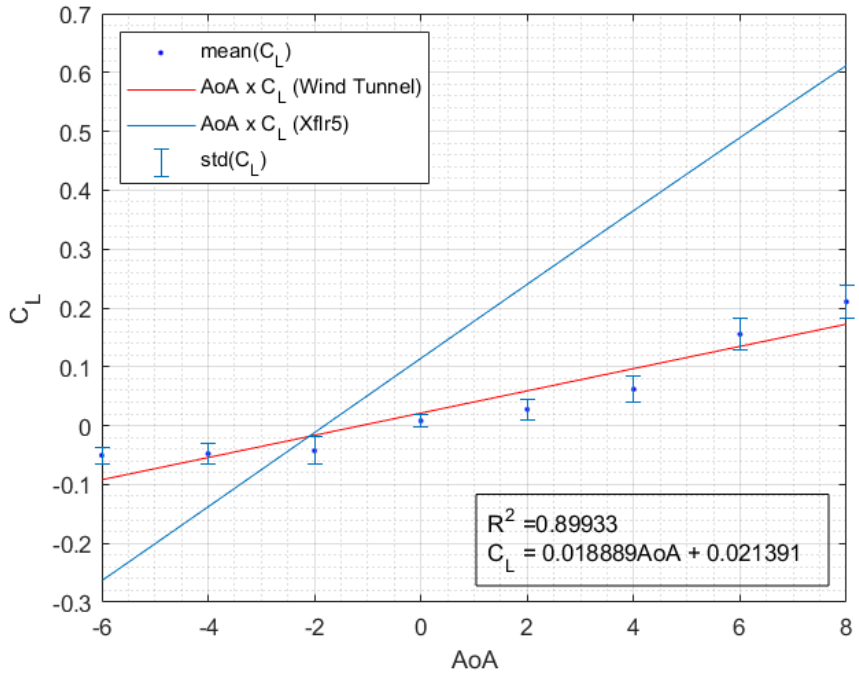

Appendix C – C_D Polar code

This appendix section showcases the code designed in software MatLab to plot the drag polar for the clean wing. For the sake of conciseness, some pages were edited out.

```
function [fitresult, gof] = createFit(AoA, CL)
clear
close all
clc

Drag_0deg  = [-1.2  -1.2    -1.2    -1.2    -1.2    -1.2
-1.2 -1.2   -1.2    -1.2    -1.2    -1.2    0   0   0   0
0   0   0   0 -0.2  -0.2    -0.2    -0.2    -0.2    -0.2
0   0   0   0   0   0   0   0   0   0   0   0   0   0
0   0   -0.2    -0.2    -0.2    -0.2    -1.5    -1.5    -
1.2    -1.2    -1.2    -1.2    -1.2    -1.2    -1.2    -1.2
-1.2    -1.2    -1.2    -1.2    -1.2    -1.2    -1.2    -
1.2    0   0   0   0   0   0   0   0   0   0   0   0   0
0   0   0   0   0   0   0   0   0   0   0   0   0   0
0   0   0   0   0   0   0   0   0   0   0   0   0   0
0   0   0   0   0   0   0   0   0   -1.2    -1.2    -
1.2    -1.2    -2.5    -1.2    -1.2    -1.2    -1.2    -1.2
-1.2    0   0   0   0   0   0   -1.2    -1.2    -1.2    -
1.2    -1.2    -1.2    0   0   0   0   0   0   -1.2    -1.2
-1.2    -1.2    -1.2    -1.2    -1.2    -1.2    -1.2    -
1.2    -1.2    -1.2    -1.2    -1.5    -1.5    -1.5    -1.5
-1.5    -0.2    0   0   0   0   -1.2    -1.2    -1.2    -
1.2    -1.2    -1.2    0   0   0   0   0   0   0   0   0
0   0   0   0   0   0   0   0   0   -1.2    -1.2    -1.2
-1.2    -1.2    -1.2    -1.2    -1.2    -1.2    -1.2    -
1.2    -1.2    -1.2    -1.2    -1.2    -1.2    -1.2    0
0   0   0   0   0   -1.2    -1.2    -1.2    -1.2    -0.2
-0.2    1   1   1   1   0   -1.2    -2.5    -2.5    -2.5
-2.5    -2.5    -1.2    0   0   0   0   0   0   0   0   0
0   0   0   -1.2    -1.2    -1.2    -1.2    -1.2    -1.2
-1.2    -1.2    -1.2    -1.2    -1.2    0   0   0   0   0
0   -1.2    -1.2    -1.2    -1.2    -1.2    -1.2    0   0
0   0   0   0   0   -0.2    -0.2    -0.2    -0.2    -0.2
-0.2    0   0   0   0   0   0   0   0   0   0   0   0   0
0   0   0   -1.2    -1.2    -1.2    -1.2    -1.2    -1.2
-1.2    -1.2    -1.2    -1.2    -1.2    -1.2    -1.2    -
1.2    -1.2    -1.2    -1.2    -1.2    -1.2    -1.2    -1.2
```

```
1.7    -1.7    -2.7    -2.7    -2.7    -2.7    -2.7    -2.7
-1.7    -0.5    -0.5    -0.5    -0.5    -0.5    -0.5    -
0.5    -0.5    -0.5    -0.5    -0.5    -1.7    -0.5    0.6
0.6 0.6 0.6 1.8 0.6 -0.5    -0.5    -0.5    -1.5    -1.5
-0.2    -0.2    -0.2    -0.2    0.8 0.8 0.8 0.8 0.8 0.8 -
0.2    -1.5    -2.5    -2.5    -2.5    -2.5    -1.2    -2.5
-1.5    -1.5    -1.5    -1.5    -1.5    -1.5    -1.5    -
1.5    -1.5    -1.5    -0.5    0.8 0.8 0.8 0.8 -0.2    -0.2
-1.5    -1.5    -1.5    -1.5    -0.5    -0.5    -0.5    -
0.5    -0.5    -0.5    -0.5    -0.5    -1.5    -1.5    -1.5
-1.5    -1.5    -1.5    -0.5    -0.5    -0.5    -0.5    -
1.5    -1.5    -1.5    -1.5    -1.5    -1.5    -0.5    0.8
0.8 0.8 0.8 0.8 0.8 -0.5    -1.5    -1.5    -1.5    -1.5
-1.5    -0.2    0.8 0.8 0.8 -0.2    -1.5    -2.7    -2.7
-2.7    -2.7    -2.7    -1.5    -1.5    -1.5    -1.5    -
1.5    -1.5    -2.7    -2.7    -2.5    -2.5    -2.5    -1.5
-0.2    -0.2    -0.5    -0.5    -1.5    -1.5    -2.7    -
3.7    -3.7    -3.7    -3.7    -2.7    -1.5    -0.5    -0.5
-0.5    -0.5    0.8 -0.5    -0.5    -0.5    -0.5    -1.5
-2.7    -1.5    -1.5    -1.5    -1.5    -1.5    -0.2    -
1.5    -1.5    -1.5    -1.5    -0.5    -1.7    -1.7    -1.7
-1.7    -1.7    -2.7    -1.5    -1.5    -1.5    -1.5    -
1.5    -1.5    -1.5    -1.5    -1.5    -1.5    -1.5    -0.5
0.8 0.8 0.8 0.8 0.8 0.8 -0.5    -0.5    -0.5    -0.5    -
0.5    -1.7    -1.7 ];

rho_0deg = 1.1713;
rho_2deg = 1.1713;
rho_4deg = 1.1707;
rho_6deg = 1.1747;
rho_8deg = 1.1792;
rho_minus2deg = 1.1713;
rho_minus4deg = 1.1713;
rho_minus6deg = 1.1713;

rho = (rho_0deg + rho_2deg + rho_4deg + rho_6deg + rho_8deg
+ rho_minus2deg + rho_minus4deg + rho_minus6deg)/8;

S_ref = 0.2405;
V_inf = 18;
q_inf = 0.5*rho*(V_inf^2);

CD_0deg = Drag_0deg/(q_inf*S_ref);
CD_2deg = Drag_2deg/(q_inf*S_ref);
```

```
CD_4deg = Drag_4deg/(q_inf*S_ref);
CD_6deg = Drag_6deg/(q_inf*S_ref);
CD_8deg = Drag_8deg/(q_inf*S_ref);
CD_minus2deg = Drag_minus2deg/(q_inf*S_ref);
CD_minus4deg = Drag_minus4deg/(q_inf*S_ref);
CD_minus6deg = Drag_minus6deg/(q_inf*S_ref);


std_CD = [std(CD_minus6deg) std(CD_minus4deg)
std(CD_minus2deg) std(CD_0deg) std(CD_2deg) std(CD_4deg)
std(CD_6deg) std(CD_8deg)];

AoA = [-6 -4 -2 0 2 4 6 8];

CD = [-mean(CD_minus6deg) -mean(CD_minus4deg) -
mean(CD_minus2deg) -mean(CD_0deg) -mean(CD_2deg) -
mean(CD_4deg) -mean(CD_6deg) -mean(CD_8deg)];


%% Fit: 'untitled fit 1'.
[xData, yData] = prepareCurveData( AoA, CD );
ft = fittype( 'poly2' );
[fitresult, gof] = fit( xData, yData, ft );

figure( 'Name', 'AoA x C_D' );
h = plot( fitresult, xData, yData);
legend( h, 'mean(C_D)', 'AoA x C_D (Wind Tunnel)');%,
'Location', 'NorthWest' );

% Label axes
xlabel AoA
ylabel C_D
grid on
grid minor

hold on

X3 = [-6 -5.5 -5 -4.5 -4 -3.5 -3 -2.5 -2 -1.5 -1 -0.5 0 0.5
1 1.5 2 2.5 3 3.5 4 4.5 5 5.5 6 6.5 7 7.5 8];
Y3 = [0.01687   0.014905    0.013694    0.012777
0.012058    0.011505    0.011088    0.01086 0.010776
0.010836    0.011092    0.011458    0.011944    0.012631
0.013465    0.014454    0.015611    0.016905    0.018361
```

```
0.019985    0.021742    0.023666    0.025755    0.028004
0.03041 0.032982    0.035709    0.038593    0.041628];

plot(X3,Y3,'DisplayName','AoA x C_D (Xflr5)');

X1 = AoA;
Y1 = CD;
D1 = std_CD;

errorbar1 =
errorbar(X1,Y1,D1,'DisplayName','std(C_D)','LineStyle','non
e','Color',[0 0.447 0.741]);
```

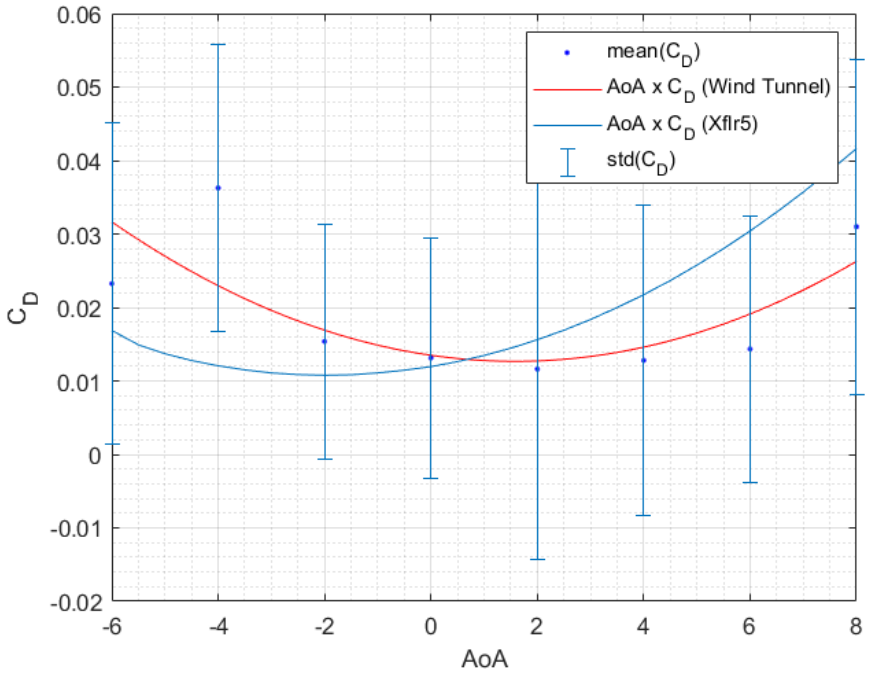

Appendix D – Control of the drone motors

This appendix section showcases the setup procedure employed to operate two drone motors at the same time with a single code script, which was sourced from the Autonomous Aircraft Laboratory (LAA) located in the Federal University of Uberlandia (UFU). The RPM of each motor can be specified by altering the wavelength of the PWM signal (via laptop), which ultimately is converted into the desired rotation by the Electronic Speed Controller (ESC). The original version was tweaked in order to control two drone motors at the same time.

General setup

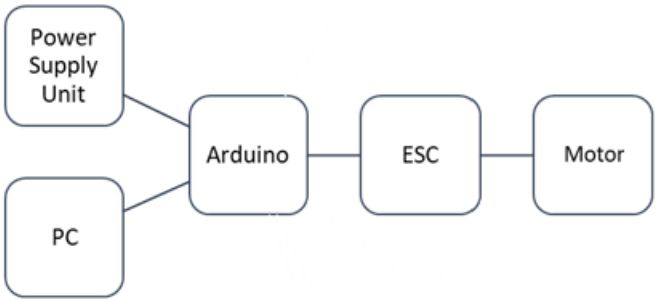

Arduino setup

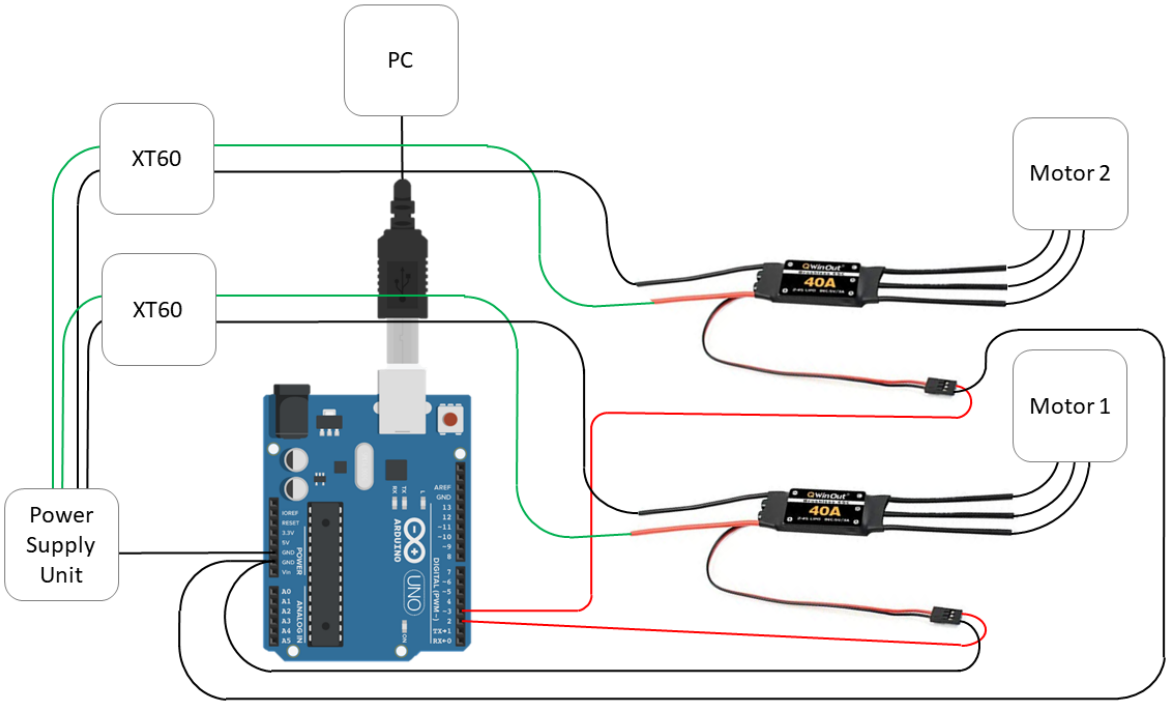

```
 /*    Universidade Federal de Uberlandia
         Faculdade de Engenharia Mecanica
            Engenharia Mecatrônica
            Realizado em 02/12/2019
  /*          Realizar o ensaio de forca e velocidade do
motor brushless        */
  //---------------------------------
  //    BIBLIOTECAS
  //---------------------------------

  #include <SPI.h>
  #include <Wire.h>
  #include <Servo.h>
  #include <math.h>
  //#include "HX711.h"
  //HX711 scale;

  //---------------------------------
  //    OBJETOS
  //---------------------------------

  Servo Motor1;
  Servo Motor2;

  //---------------------------------
  //    VARIAVEIS GLOBAIS
  //---------------------------------

  float t_ks,t_k, t_km1,now,newnow;
  float N1=0.2066;
  float N2=0.4131;
  float N3=0.2066;

  float C1=1.0000;
  float C2=-0.3695;
  float C3=0.1958;
  float deltaT;
  float Ta =0.012;//[segundos]
  int j=0;

  //---------------------------------
  //   VARIAVEIS DOS MOTORES
  //---------------------------------
  float U_0=1000;
```

```
  float U=1000;
  float pwm_1=2000;
  float pwm_2=2000;
  float u_k=0;
  float u_km1=0;

  float force=0.00;
  float f_k=0.00;
  float f_km1=0.00;
  float f_km2=0.00;
  float ff_km1=0.00;
  float ff_km2=0.00;
  int rndSeed=8;
  // HX711 circuit wiring
  #define LOADCELL_DOUT_PIN 5
  #define LOADCELL_SCK_PIN 6

  int command;
  //----------------------------------
  //    VOID SETUP
  //----------------------------------

  void setup() {

    Serial.begin(115200);

  //Initialising the HX711 SCALE
  // scale.begin(LOADCELL_DOUT_PIN, LOADCELL_SCK_PIN);

  // scale.set_scale(783.97806326038055590324351697495);
  //  scale.tare();

    //======================
    //  MOTOR
    //======================
    //GPIO4 = D2
    Motor1.attach (2); //attach the motor
    Motor1.write(0); //DJI MOTOR Initialization
    Motor2.attach (3); //attach the motor LOCALIZACAO DO
MOTOR 2!!!!!!!!!!!!!!!!!!!!!!!!!!!
    Motor2.write(0); //DJI MOTOR Initialization
    randomSeed(rndSeed);
    t_ks=millis();
    newnow=millis();
```

```
    delay(250);
  }


  //----------------------------------
  //    VOID LOOP
  //----------------------------------

  void loop()
  {
     t_k=millis();
   if(Serial.available()>0)
    {
     command=Serial.read();
  //  //MOTOR
    if(command==113)//letra q
      {
        Motor1.write (0); //full reverse. The ESC will
automatically brake the motor.
        pwm_1=1000;

      }
     if(command==119)//letra w
      {
        pwm_1=pwm_1+50;
        saturacao();
        Motor1.write (pwm_1);
      }
    if(command==101)//letra e
      {
        pwm_1=pwm_1+1;
        saturacao();
        Motor1.write (pwm_1);
      }
    if(command==114)//letra r
      {
        pwm_1=pwm_1-1;
        saturacao();
        Motor1.write (pwm_1);
      }
     if(command==97)//letra a
      {
        Motor2.write (0); //full reverse. The ESC will
automatically brake the motor.
```

```
        pwm_2=1000;

      }
      if(command==115)//letra s
      {
        pwm_2=pwm_2+50;
        saturacao();
        Motor2.write (pwm_2);
      }

      if(command==100)//letra d
      {
        pwm_2=pwm_2+1;
        saturacao();
        Motor2.write (pwm_2);
      }

      if(command==102)// letra f
      {
        pwm_2=pwm_2-1;
        saturacao();
        Motor2.write (pwm_2);
      }

      if(command==32)// space
      {
        Motor1.write (0); //full reverse. The ESC will
automatically brake the motor.
        pwm_1=1000;

        Motor2.write (0); //full reverse. The ESC will
automatically brake the motor.
        pwm_2=1000;

      }

    }

  //      readSensor();
        printInfo();

    while( (millis()- t_k)/1000 < Ta)
         {
           //Wait for the next amostragem
```

```
        }

  }

  //-----------------------------------
  //    SUBROTINAS
  //-----------------------------------

  void saturacao(){

    /*Saturaçao da variavel de comando entre 1000us e
2000us*/
    //MOTOR 1 PRETO
    if(pwm_1 < 1000)
    {
      pwm_1 = 1000;
    }
    if(pwm_1 > 2000)
    {
     pwm_1=2000;
    }

      /*Saturaçao da variavel de comando entre 1000us e
2000us*/
    //MOTOR 2 PRETO
    if(pwm_2 < 1000)
    {
      pwm_2 = 1000;
    }
    if(pwm_2 > 2000)
    {
     pwm_2=2000;
    }
  }

  void printInfo(){
    //Serial.print((millis()- t_k)/1000,4);
    Serial.print((millis()/1000.00),5);
    Serial.print("\t ");
    Serial.print(pwm_1);
    Serial.print("\t ");
    Serial.print(pwm_2);
    Serial.print("\t ");
```

```
    Serial.print(force*9.81/1000);  //multiplicar por 9.81
pra ser em Newtons
    Serial.print("\t ");
    Serial.println(((millis()-t_k)/1000.00),5);
  }

  //void readSensor(){
  //  f_k= scale.get_units(1);
  //  force = ( (N1)* f_k + (N2) * f_km1 + (N3) * f_km2 -
C2 * ff_km1 - C3 * ff_km2 )/(C1);
  //  f_km2=f_km1;
  // f_km1=f_k;
  //  ff_km2=ff_km1;
  //  ff_km1=force;
  //}
```